COMPACT ESPI DEVICE FOR ISOTROPIC MEASUREMENTS OF RESIDUAL STRESS

by

Samuel Melamed

B.A.Sc, University of Toronto, 2011

A THESIS SUBMITTED IN PARTIAL FULFILLMENT OF
THE REQUIREMENTS FOR THE DEGREE OF

MASTER OF APPLIED SCIENCE

in

THE FACULTY OF GRADUATE AND POSTDOCTORAL STUDIES

(Mechanical Engineering)

THE UNIVERSITY OF BRITISH COLUMBIA

(Vancouver)

August 2015

Abstract

Residual stresses are self-equilibrating stresses that exist within bodies without any external loads acting on them. Monitoring residual stresses is vital to engineer safe and reliable structures. A reliable means of measuring residual stress is by drilling a small hole in the body and observing the resulting redistribution of the stress using an electronic speckle pattern interferometer (ESPI). Current ESPI systems are not suitable to measure stress on large or immovable structures because they depend on highly coherent laser sources that are bulky, delicate and not suitable for rugged field conditions. Additionally, ESPI is limited to a single direction of measurement. If the measurement axis is misaligned with the principal stress direction accuracy is reduced. This presents a practical challenge when measuring unknown residual stress states in the field. A compact ESPI device providing an isotropic residual stress measurement is presented here. The compactness of the device is possible by a novel optical arrangement that uses a diffraction grating and a miniature laser diode. This optical arrangement can be geometrically tuned to provide high quality measurements even with low coherence laser diodes. Furthermore, the device is constructed with two orthogonal measurement axes to reduce the influence of instrument alignment on measurement accuracy and to improve the overall precision by doubling the quantity of data. Experimentation with a calibrated bend specimen showed that the device has an accuracy ranging 9-12MPa and precision of 13MPa. This integration of ESPI and hole drilling modules into a compact, stand-alone unit is a significant milestone for in-field residual stress measurements.

Preface

All of the work presented henceforth was conducted in the Renewable Resources Laboratory at the University of British Columbia, Point Grey campus.

A version of Chapter 3 has been published in Optics and Laser in Engineering, volume 67, under the title "In-plane ESPI Using An Achromatic Interferometer With Low-coherence Laser Source." I was responsible for the experimental conceptualization of Section 3 of that paper, apparatus construction and data collection for Section 4 and 5. Summer student, Yijian Zhang, conducted the data collection of Section 3. My supervisor, Dr. Schajer, was responsible for the experimental conceptualization of Section 4 and the manuscript composition. Dr. Schajer and I shared in the analysis and visualization of the results.

I was the lead investigator of all remaining work where I was responsible for the design and construction of the compact ESPI apparatus, experimental conceptualization, data collection, result analysis and manuscript composition.

Table of Contents

List of Figures

List of Tables

List of Graphs

Dedication

Dedicated to the memory of my grandfather

Samuil Melamed

who inspired my passion for science

and instilled the persistence required to pursue it.

Acknowledgements

Firstly, I would like to thank my supervisor, Dr. Gary Schajer, for his support and guidance in solving the innumerous details inherent in a physical project like this. Dr. Schajer has a remarkable ability to focus on the things that matter and disregard the things that do not. I find this to be one of the most important skills an engineer can have and am inspired to perfect it throughout my career.

Markus Fengler and his team, thank you for teaching me how to use the wide range of equipment in the machine shop and for your time and efforts in helping me build such an intricate device.

Glenn Jolly and Sean Buxton, I came to UBC with the ambition to design and build electromechanical equipment, yet I was completely clueless about circuitry and electronics. Thank you for helping me fulfill my ambition through your patient explanations and assistance in debugging the numerous electrical issues I encountered along the way.

I would like to thank my lab mates Darren Sutton, Guillaume Richoz, Wade Gubbels, Ted Angus, Josh Harrington and Yijian Zhang for their varied technical perspective and making the lab a fun and exciting place.

Finally, I would like to thank my friends and family for their inspiration, encouragement and care. I couldn't have achieved my personal and professional goals without you. Thank you, thank you!

An idea that is developed

and put into action

is more important than

an idea that exists

only as an idea

~ Edward de Bono

Chapter 1: Introduction

This research introduces a novel Electronic Speckle Pattern Interferometry (ESPI) device for practical measurements of residual stress. The main motivation for such an instrument is to measure the residual stress state of components and structures in the field. Current ESPI instruments are bulky and require tightly controlled laboratory conditions, which makes them impractical for large or immovable structures. Consequently, a practical system is defined as compact and robust, capable of withstanding field conditions while providing high quality residual stress measurements.

1.1 Residual Stress

A stress state which exists within a body without any external loads is called residual stress. Residual stress is self-equilibrating, that is, areas of tension are balanced out by areas of compression [1]. Residual stresses occurs due to material strain inconsistencies in a body [2]. These inconsistencies can occur on a micro or a macro scale. Micro residual stresses extend over the submicron range and are typically formed due to inhomegeneity of grain structures [2]. Macro residual stresses extend over several millimeters and are typically formed by areas of the body which have plastically deformed causing adjacent areas to strain elastically. These types of stresses can be significantly high (>100s of MPa) and if unaccounted for can have catastrophic effects. This work targets the measurement of macro residual stresses.

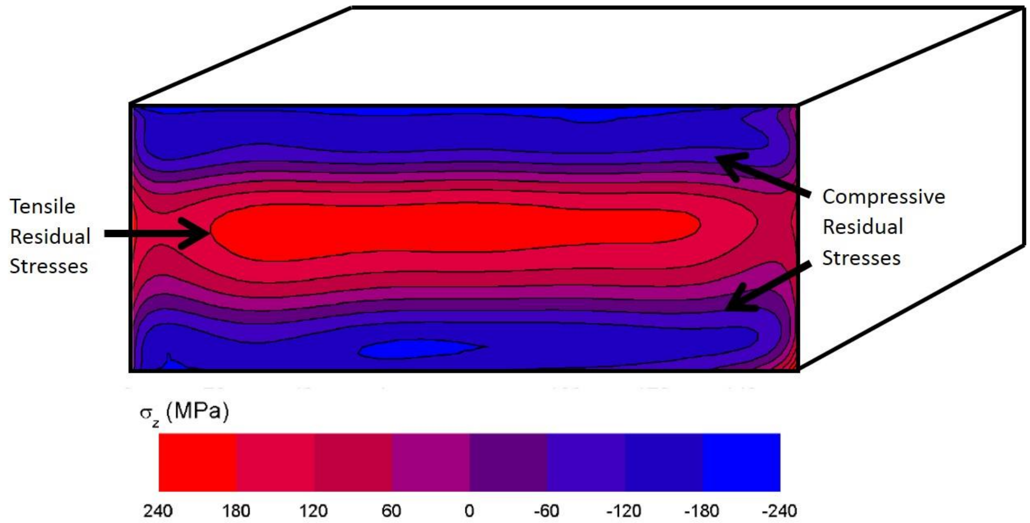

Figure 1.1 - Stress distribution of a rolled steel bar cross section, adapted from [3]

1.1.1 Formation of Residual Stress

Almost all manufacturing techniques introduce residual stress [1]. Typically residual stress forms during non-uniform plastic deformation, that is, one area of a body plastically deforms more than another area [4]. This internal difference in deformation causes elastic stress between these two areas.

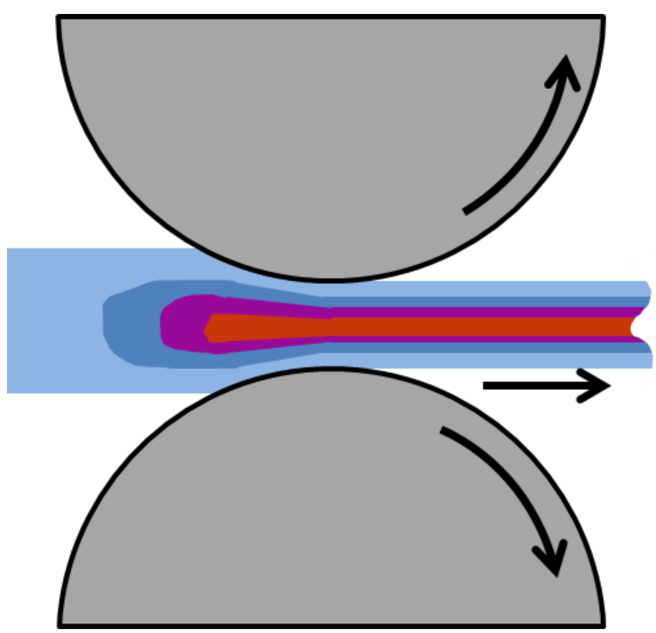

Figure 1.2 - Rolling process introducing residual stress

For example, as shown in Figure 1.1, the surface of rolled sheet metal is in compression while the center is in tension. Figure 1.2 shows why this occurs. During the rolling process the surface material stretches along the rolled direction more than the central material. As a result the central material pulls on the surface material causing the residual stress distribution seen in Figure 1.1. Since most manufacturing processes seek to give a body a particular permanent shape, invariably they also introduce residual stresses.

1.1.2 Effects of Residual Stress

Residual stress can be desirable or undesirable. When considering a load bearing body, undesirable residual stresses add to the applied load thereby decreasing its factor of safety. Residual stresses can also have adverse effects on the dimensional stability of a body. For example, during manufacturing, if material is removed non-uniformly across the residual stress profile, the body would deform to reach stress equilibrium. Such is the case of the warped airplane cargo ramp shown in Figure 1.3.

Figure 1.3 - Warped cargo ramp (D. Bowden, Boeing Company)

On the other hand, residual stresses can increase a material's fracture toughness. A good example of this is glass, which typically fails under tension due to opening of surface cracks. By controlling the cooling rate of the glass surface, relative to its core cooling rate, desirable compressive stresses can be introduced into the surface of the glass. These compressive surface stresses force any surface cracks closed, thereby increasing the tensile strength the glass can tolerate [1], [4]. This type of glass is called toughened glass and its residual stress profile can be seen in Figure 1.4.

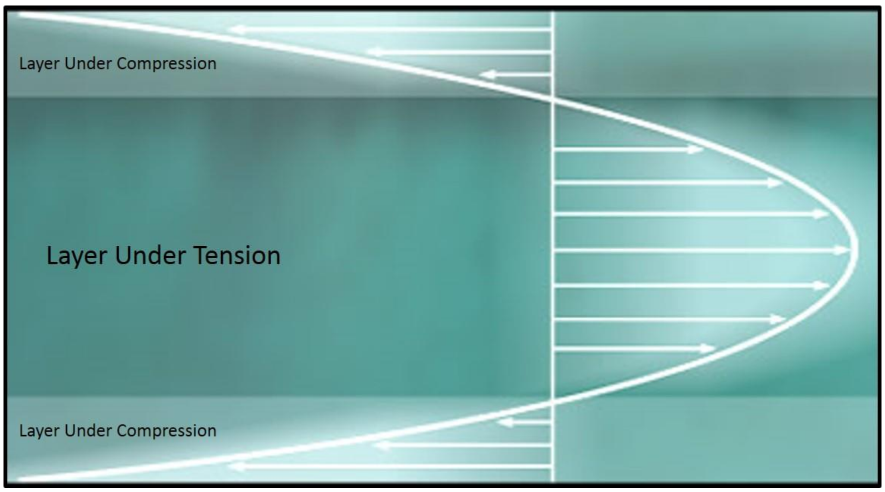

Figure 1.4 - Residual stress distribution of toughened glass, adapted from [5]

Whether it is monitoring a component's stress state or controlling its mechanical properties, measuring residual stress is vital in engineering safe and reliable structures.

1.1.3 Challenges of Measuring Residual Stress

Because of its internal nature, residual stress in a body is challenging to evaluate. Measurements are therefore indirect, meaning, properties which relate to stress are measured and the residual stress is subsequently determined.

There are several residual stress measurement techniques, each with its own advantages and disadvantages. Because of the wide range of measurement needs (i.e. precision, depth, damage, portability, cost, etc.) there is no one perfect method. The aim of this research is to develop a measurement technique appropriate for field measurements of mechanical structures such as automotive frames, ship hulls, pipes, etc.

1.2 Residual Stress Measurement Techniques

Most residual stress measurement techniques fall under two categories, non-destructive and destructive. Non-destructive techniques generally measure the distribution of microstructures inside the body relating these properties to known stress states. Destructive methods cut into the body causing a redistribution of the residual stress and a subsequent material displacement. By observing the body before and after the cut is made this displacement can be measured and related to corresponding stresses. If the cut in the body is relatively small and tolerable the measurement technique is deemed semi-destructive. Semi-destructive methods are particularly appealing because they do not compromise the functionality of the measured component. One such method is the Hole Drilling Method whereby a small (≈ Ø2mm) hole is drilled into the body and the surrounding surface is evaluated. This method is particularly appropriate for this study as it is practical, robust and precise to within 10-30% [1].

1.2.1 Hole Drilling

The hole drilling technique is a stress relieving technique. Figure 1.5 shows a residually stressed specimen with a surface layer in compression. By making a hole in the body the tensile residual stress on the surface is released and the surface pulls back. Due to Poisson's effect there is also a small surface elevation as well.

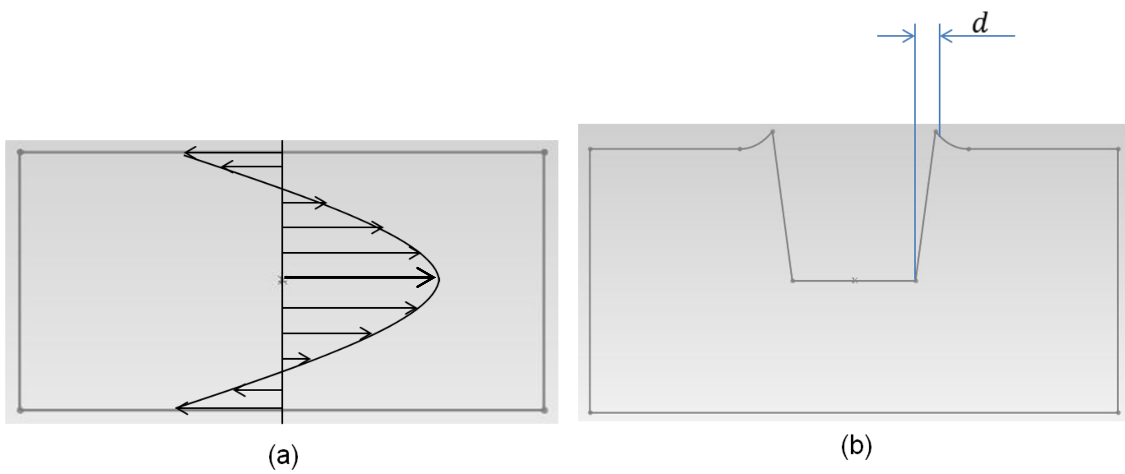

Figure 1.5 - a) Typical residual stress profile of rolled metal b) Surface deformation due to hole relaxation

The change in the geometry around the hole is directly proportional to the amount of residual stress that has been drilled out. Therefore by sensing this deformation and comparing it to hole-drilling models of varying stress levels the residual stress can be interpolated. Put simply, measuring residual stress using the hole drilling method is a three step process:

1. Drill a small hole in the area of interest
2. Detect the resulting deformation of the material around the hole
3. Compute the corresponding residual stress

This hole drilling methodology was pioneered by Dr. Richard J. Mathar in the 1930s and over the past 80 years has been continuously developed and refined [6]. One of the major challenges of the method is detecting the extremely small (≈ 100nm) displacement resulting around the hole. This is a particularly challenging issue when measurements have to be taken in the field where noise can easily "wash-out" the faint displacement signal. Therefore, one of the major challenges this research aims to overcome is to develop a stable system, capable of detecting these small displacements outside of tightly controlled laboratory conditions [7].

1.2.2 Sensing Deformation

There are several techniques to detect the deformation caused by hole-drilling, these generally fall under two categories, strain gage or optical techniques.

The standardization of specialized strain gage rosettes and measurement procedure has facilitated an extremely robust and reliable means for measuring the surface deformation caused by hole drilling [1], [8], [9]. However, due to the stringent physical requirements, strain gage measurements require significant operator skill and preparation time.

Optical techniques generally fall into two categories, interferometric techniques and Digital Image Correlation (DIC). Interferometric techniques utilize the phase change caused by the interference of monochromatic light to measure surface deformation. DIC on the other hand utilizes pattern recognition algorithms to correlate known patterns to deformed patterns. Optical techniques are extremely sensitive to environmental fluctuation and therefore are limited to controlled laboratory environments.

1.2.2.1 Strain Gage Measurements

Strain gages are transducers whose electrical resistance changes with its geometry. The strain gage is physically attached to the surface of the body. Any deformation in the body is directly translated to the strain gage where it can be electrically measured. To measure residual stress, specialized hole-drilling rosettes have been developed. Figure 1.6 shows a standardized rosette geometry where 3 strain gages are precisely oriented at 0°, 135° and 270° from each other [9]. The hole is drilled in the center of the specialized rosette to determine the three in-plane stress components σ_x, σ_y and τ_{xy}.

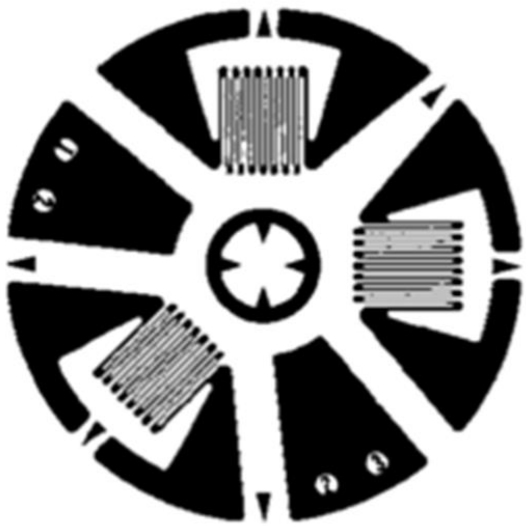

Figure 1.6 - Hole drilling strain gauge rosette, adapted from [9]

1.2.2.2 Electronic Speckle Pattern Interferometry

Interferometry is the study of wave interaction in order to make various types of measurements. For the purpose of this research, interferometry is referred to the use of light wave interaction to measure displacement. Surfaces illuminated with monochromatic light, such as laser light, appear grainy as seen in Figure 1.7. This 'speckle pattern' is caused by light interference and is directly related to the surface being illuminated. Thus, any surface deformation will cause the speckle pattern to change [10].

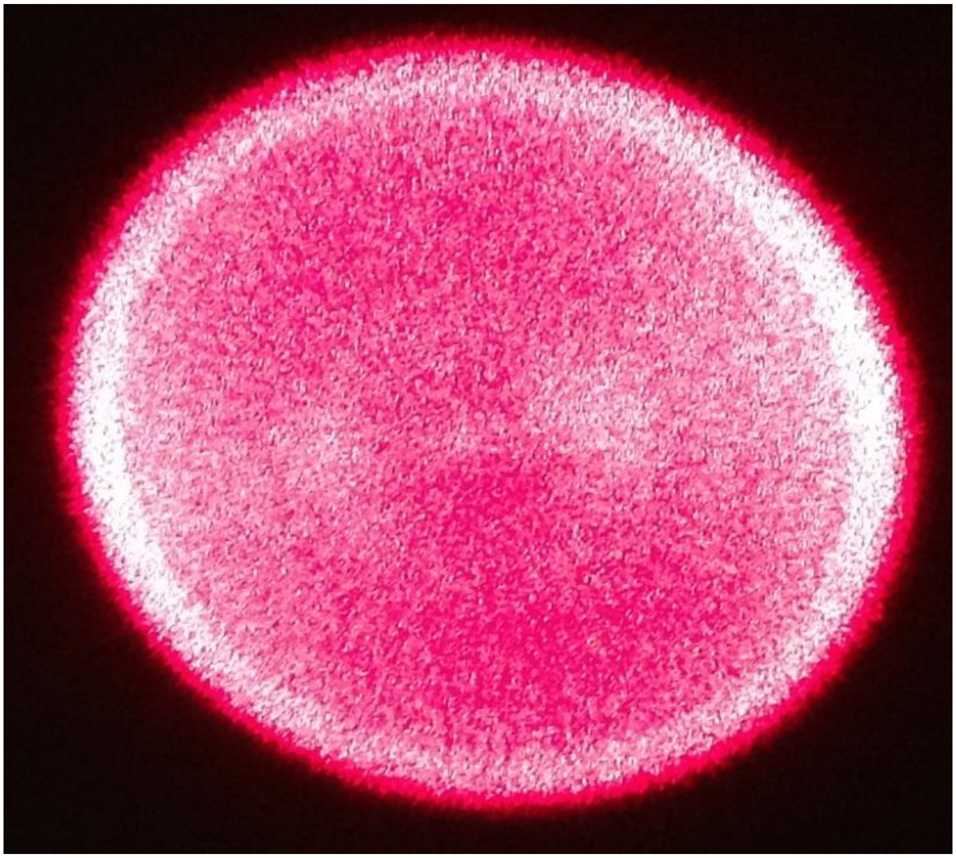

Figure 1.7 - Speckle pattern formed with a red laser diode

An electronic speckle pattern interferometer is capable of detecting a change in this speckle pattern and correlate it to the surface deformation that caused it. Figure 1.8 shows a typical ESPI setup. Because the wavelength of visible light is in the order of 400-700nm, ESPI is sensitive to 30nm-10μm deformations [11].

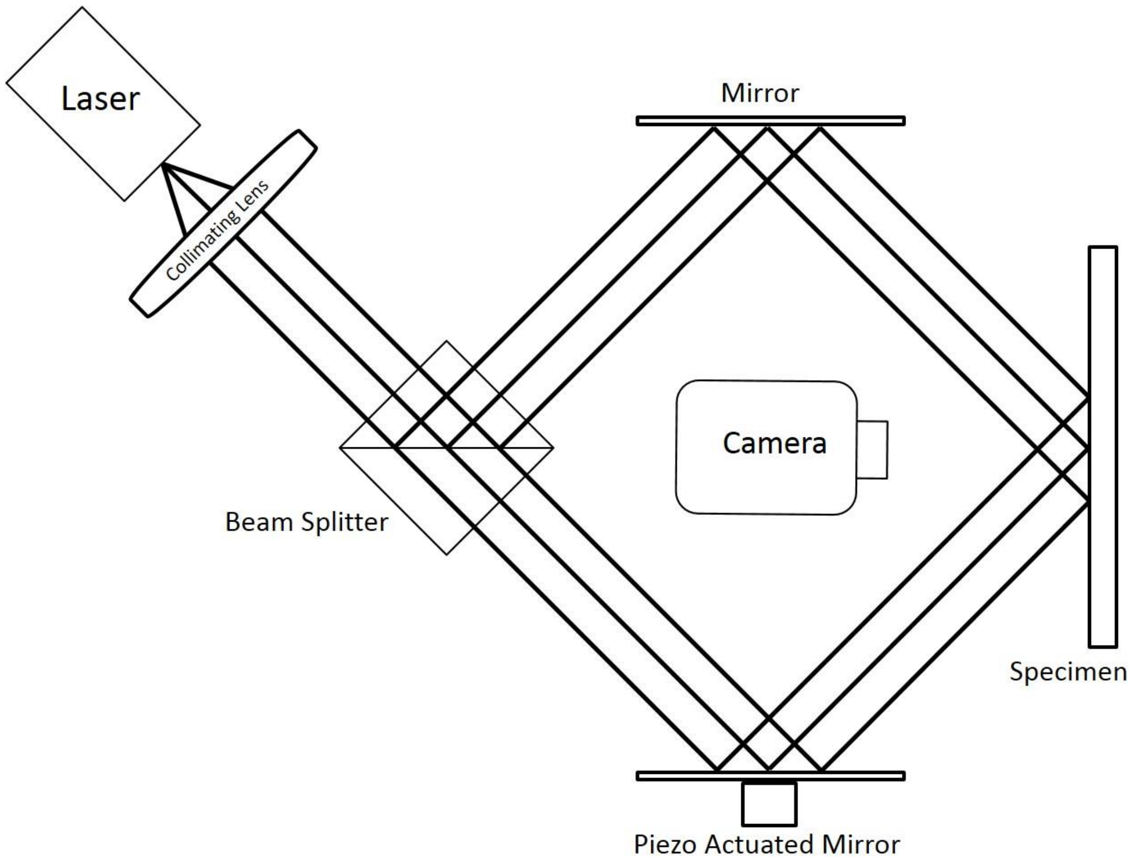

Figure 1.8 - Plan view of a typical ESPI set up

1.2.2.3 Strain Gage vs. ESPI

Both strain gage and ESPI techniques have their advantages and disadvantages. Table 1.1 highlights some of these key differences between the two systems.

	Advantages	Disadvantages
Strain Gauge	Accurate and reliable measurements	Few localised measurements
	Compact, portable and robust equipment	Long preparation and measurement time
ESPI	Several measurements along specimen	Sensitive to ambient noise
	Minimal surface preparation	Bulky and delicate equipment

Table 1.1 - Strain gage vs. ESPI technique comparison table

The main advantage of strain gage systems is their robustness and suitability for field use. A typical portable strain gage system can be seen in figure 1.9.

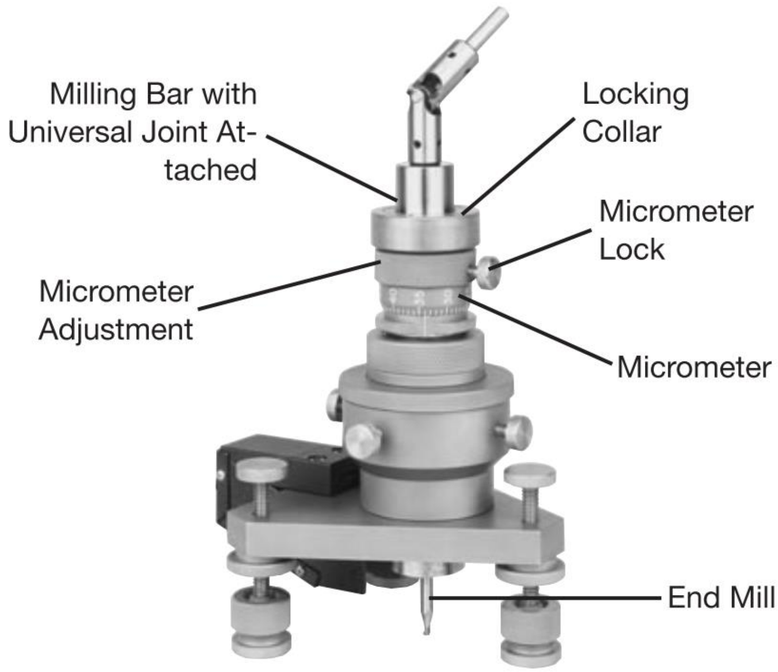

Figure 1.9 - Portable strain gauge drilling system, adapted from [12]

However, due to the physical requirement of preparing the measurement surface and setting up the strain gage equipment only a few strategic measurements can be practically taken. ESPI systems require significantly less surface preparation and thus have the capability to take several measurements in rapid successions. A greater number of measurements provides a clearer picture about the stress distribution in a structure. Nevertheless, conventional EPSI systems are typically bulky set ups that require tightly controlled operational conditions in order to yield useful measurements. As a result they are operated in tightly controlled laboratory environments.

1.3 Sate of the Art and Research Objective

The overall motivation of this research is to develop a compact ESPI system, capable of obtaining practical, in-field residual stress measurements. One of the greatest challenges in developing such a device is the high quality illumination source required for reliable ESPI measurements. These illumination sources are bulky, delicate, and generally not suitable for rugged field conditions. Additionally, ESPI is limited to a single direction of measurement. If the measurement axis is misaligned with the principal stress direction accuracy is reduced. This presents a practical challenge when measuring unknown residual stress states in the field.

Several companies such as Stresstech, Dantec Dynamics, and Steinbichler have developed successful commercial ESPI instruments for stress and strain analysis. However, these companies have yet to develop a practical and portable ESPI instrument. Therefore their ESPI services are limited to in-house measurements.

Viotti and Albertazzi have been successful at developing a portable ESPI instrument for residual stress measurements [13]. However, the miniaturization of their equipment has compromised measurement quality. The major reason for this is that portable ESPI equipment relies on a laser diode whose wavelength purity is much inferior in comparison to single mode lasers typically used in laboratory ESPI measurements [14], [15].

The motivation of this research is to develop a system that would function practically in field conditions without compromising measurement quality. It is recognized that the most important factor for ESPI measurements is the wavelength purity of the illumination source, otherwise known as the coherence length. The coherence length of the illuminations source defines the quality of the signal. **Therefore, a system which allows for miniature, low coherence laser diodes to provide high quality measurements, independent of instrument alignment with the principal stress direction would be an ideal solution for in-field measurement.**

1.4 Solution Insight

In order to meet the objectives of this project a novel ESPI arrangement utilizing a diffraction grating, instead of a traditional beam splitter, is developed. It will be shown that the use of such an optical element along with careful geometrical tuning allows for extremely high quality measurements, even with low coherence illumination sources such as laser diodes.

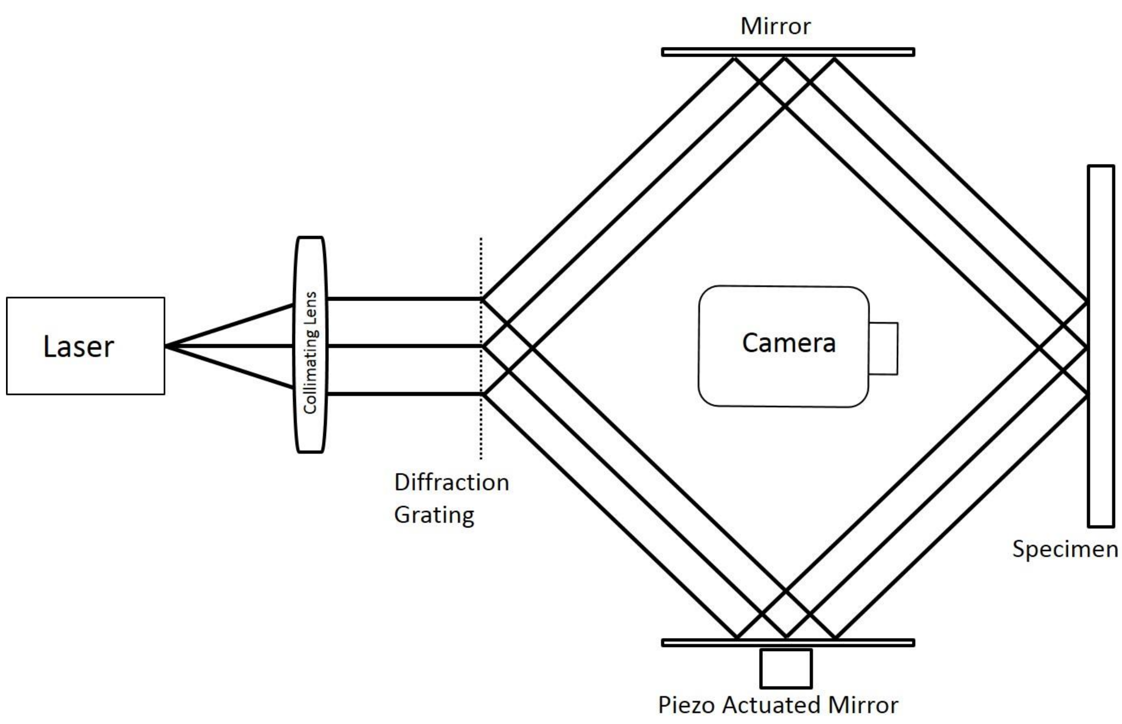

Figure 1.10 - Diffraction grating ESPI set-up

The insight to use a diffraction grating comes from the necessity to maintain equal optical path lengths within the illumination of the interference pattern. Through experimentation it was discovered how to tune the geometry of the interferometer to yield measurements with extremely high quality.

This new system also lends itself to being practically integrated into a portable device. A compact and portable device with this novel ESPI arrangement was constructed. In addition, the device was constructed with dual axis illumination to provide a complete in-plane measurement, free from directional bias. This dual axis capability has been shown to further improve the precision of residual stress measurements.

1.5 Experimental Method

This thesis firstly proves the effective use of miniature laser diodes to provide high quality ESPI measurements. To do so, formulas that relate the geometry of the interferometer to measurement quality are derived. The formulas are then verified by tuning the geometry and observing the control over measurement quality. Secondly it integrates the novel laser diode set up into a compact and portable ESPI device. The device is then used to measure known residual stress profiles. The deviation of the measurements is then calculated to determine the accuracy and precision the device is capable of.

1.6 Overview

The present work is organized as follows:

Chapter 2 gives an in depth explanation of residual stress measurements using the Hole Drilling method and Electronic Speckle Pattern Interferometry.

Chapter 3 introduces the proposed diffraction grating interferometer arrangement.

Chapter 4 introduces the compact ESPI device and the various modules comprising it.

Chapter 5 presents the accuracy and precision of the portable ESPI device.

Chapter 6 discusses the contributions of this study, and presents future work and recommendations.

Chapter 2: Residual Stress Measurements Using ESPI and Hole Drilling

ESPI is a powerful imaging technique that enables the visualization and measurement of minute (10nm-30μm) surface displacements of strained bodies [11][16]. Finite element analysis (FEA) is a powerful computational tool used to mathematically model applied loads on a body and compute the resulting displacements, strains and stresses. This analysis combines these two methods to measure locked-in residual stresses. Using FEA, a family of displacement fields is generated over a range of hole geometries and stress conditions. These finite element runs are used to generate lookup interpolation tables to provide the best fit for ESPI obtained deformation maps [17]. This interpolation method has proven to be very effective at accurately determining residual stress [18]. For compact ESPI measurements, a challenge remains to obtain reliable deformation maps. This challenge is rooted in the ability of the illumination source to provide a detectable signal.

2.1 Computation of Residual Stress from Hole Drilling

Figure 2.1a shows a section of a residually stressed body. The residual stresses, σ_x, σ_y, τ_{xy}, are represented along the boundary of the section and are the unknowns that this analysis aims to determine.

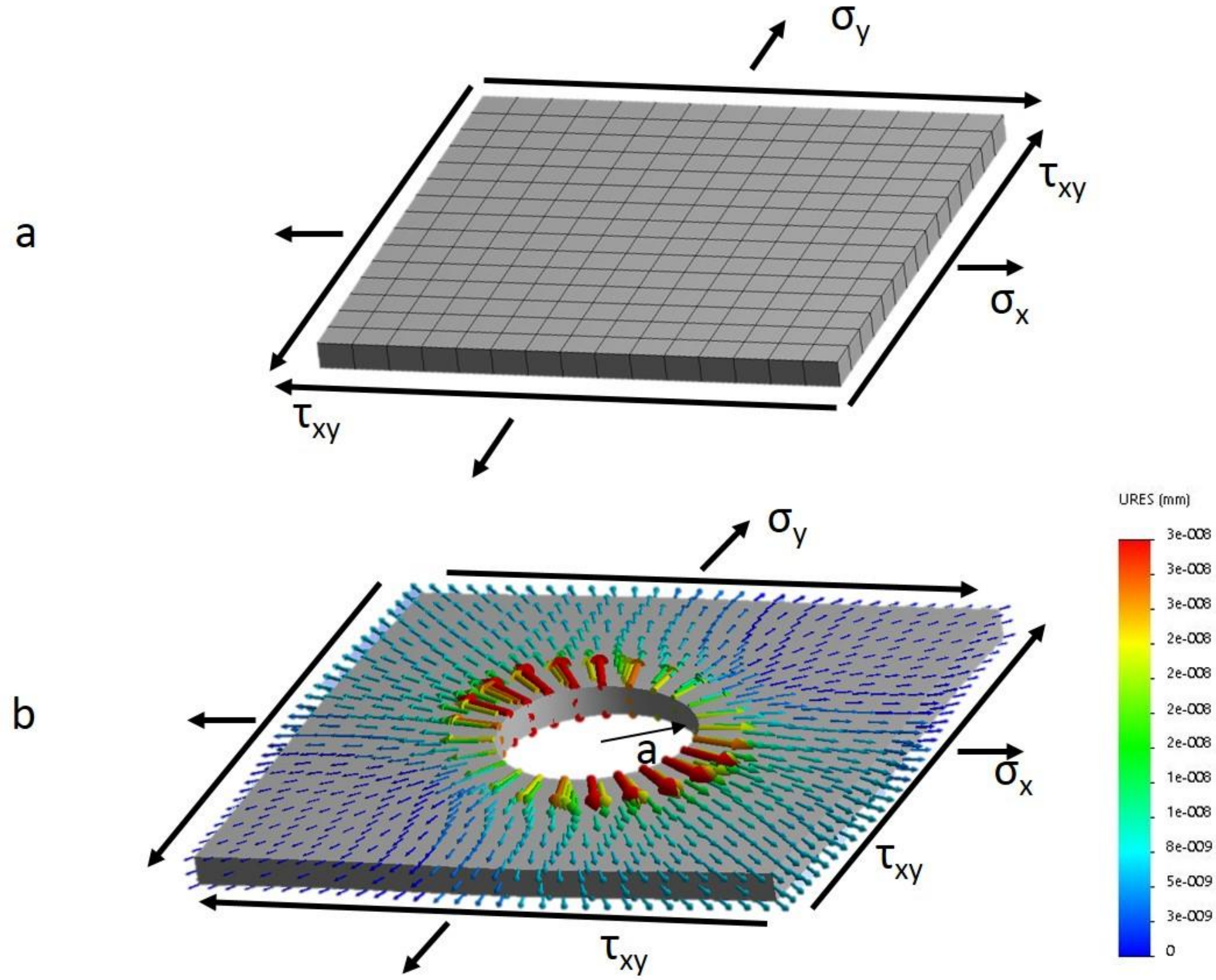

Figure 2.1 - a) Section of a stressed body b) Hole drilling displacement map of a residually stressed body

A hole drilled into this section causes the elements around the hole to deform as shown by the finite element model in Figure 2.1b and represented by displacement field $D_{FEA}(x, y)$. An ESPI interferometer is capable of measuring such a displacement field, which can be represented by $D_{ESPI}(x,y)$. The goal of this analysis is to compare the measured and computationally generated displacement fields to extract the three unknown stresses.

2.1.1 FEA Generated Displacement Field

Figure 2.1b shows the finite element displacement field, $\mathrm{D_{FEA}(x,y)}$, caused by drilling a hole, with radius a, in a residually stressed specimen with elastic modulus E. This computed displacement field is a superposition of the displacement fields, $\mathrm{D_{\sigma_x}(x,y)}$, $\mathrm{D_{\sigma_y}(x,y)}$, $\mathrm{D_{\tau_{xy}}(x,y)}$, resultant by applying each stress component, σ_x, σ_y, τ_{xy}, individually.

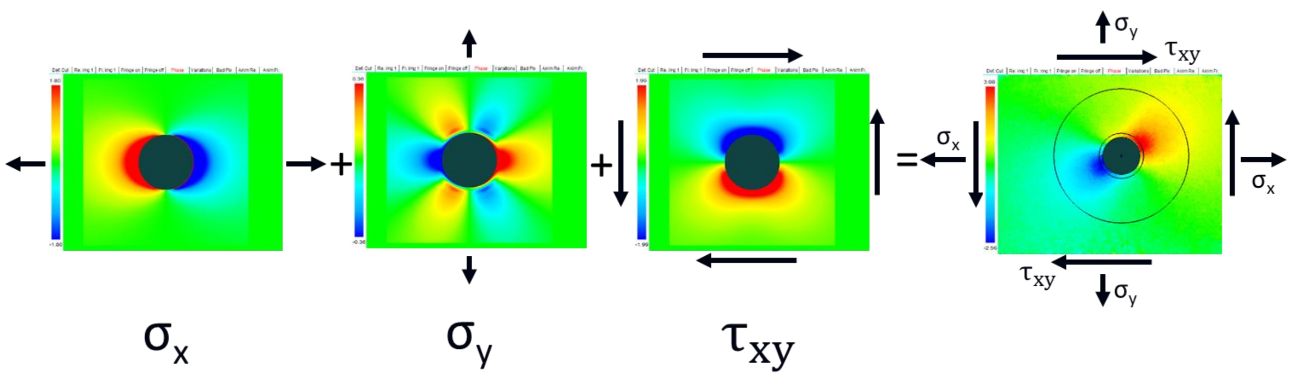

Figure 2.2 - Displacement of each stress component superimposed to form the combined displacement pattern

Mathematically this can be represented by:

$$D_{FEA}(x,y) = \mathrm{C_1 D_{\sigma_x}(x,y) + C_2 D_{\sigma_y}(x,y) + C_3 D_{\tau_{xy}}(x,y)} \tag{1}$$

where $D_{\sigma_x}(x, y)$, $D_{\sigma_y}(x, y)$, $D_{\tau_{xy}}(x, y)$ are displacement fields generated by applying σ_x, σ_y, τ_{xy}, individually in an FEA model. C_1, C_2, C_3 are dimensionless factors that indicate the contribution of each individual displacement field, $D_{\sigma_x}(x, y)$, $D_{\sigma_y}(x, y)$, $D_{\tau_{xy}}(x, y)$, to the combined displacement field $\delta_{FEA}(x, y)$.

These factors are directly proportional to their respective stress component, the geometry of the hole, *a*, and the elastic modulus of the body, *E*. Equation (1) can therefore be rewritten as [19]:

$$D_{FEA}(x, y) = \left(D_{\sigma_x}(x, y)\right)\frac{\sigma_x}{aE} + \left(D_{\sigma_y}(x, y)\right)\frac{\sigma_y}{aE} + \left(D_{\tau_{xy}}(x, y)\right)\frac{\tau_{xy}}{aE} \tag{2}$$

By varying the geometry of the hole and the amount of stress applied in the FEA model a family of displacement fields is generated. A wide range of displacement fields can be represented by linear combinations of the FEA generated displacement fields, $D_{\sigma_x}(x, y)$, $D_{\sigma_y}(x, y)$, $D_{\tau_{xy}}(x, y)$.

2.1.2 Rigid Body Motion

In practice, ESPI displacement measurements will include artifacts due to rigid body motion. These artifacts are caused by bulk movements and air currents. For an in-plane ESPI measurement, these rigid body movements can be expressed as translations in x-axis, w_1, translations in the y-axis, w_2, and in-plane rotation around the center of the hole, w_3 [19]. These rigid body movements affect the whole displacement field uniformly and therefore can be linearly added to the displacement field in formula (2).

$$D(x, y) = \left(D_{\sigma_x}(x, y)\right)\frac{\sigma_x}{aE} + \left(D_{\sigma_y}(x, y)\right)\frac{\sigma_y}{aE} + \left(D_{\tau_{xy}}(x, y)\right)\frac{\tau_{xy}}{aE} + \frac{w_x}{a} + \frac{w_y}{a} + \frac{w_o}{a} \tag{3}$$

In effect, the hole drilling computation aim to determine three in-plane stresses, σ_x, σ_y, τ_{xy} and three in-plane rigid body motions, w_1, w_2, w_0.

2.1.3 Residual Stress Computation

To compare the modeled displacement field with the measured displacement field the two are equated and the measured displacement field is substituted into equation (3).

$$D_{ESPI}(x,y) = D_{FEA}(x,y) \tag{4}$$

$$D_{ESPI}(x,y) = \left(\mathrm{D}_{\sigma_x}(\mathrm{x,y})\right)\frac{\sigma_x}{aE} + \left(\mathrm{D}_{\sigma_y}(\mathrm{x,y})\right)\frac{\sigma_y}{aE} + \left(\mathrm{D}_{\tau_{xy}}(\mathrm{x,y})\right)\frac{\tau_{xy}}{aE} + \frac{w_x}{a} + \frac{w_y}{a} + \frac{w_o}{a} \tag{5}$$

Equations (5) is asking what magnitudes of σ_x, σ_y, τ_{xy}, w_1, w_2, and w_0 result in the measured displacement field, $D_{ESPI}(x,y)$. To determine these unknowns a minimum of six displacement equations are required. ESPI displacement measurements are images where each pixel represents a displacement vector. A typical ESPI measured displacement field, shown in Figure 2.3, is composed of over 100,000 displacement vectors. Therefore, the system of equations is highly over determined. A least squares approximations is used to compute the best fit of σ_x, σ_y, τ_{xy}, w_1, w_2, and w_0 [17], [18], [19].

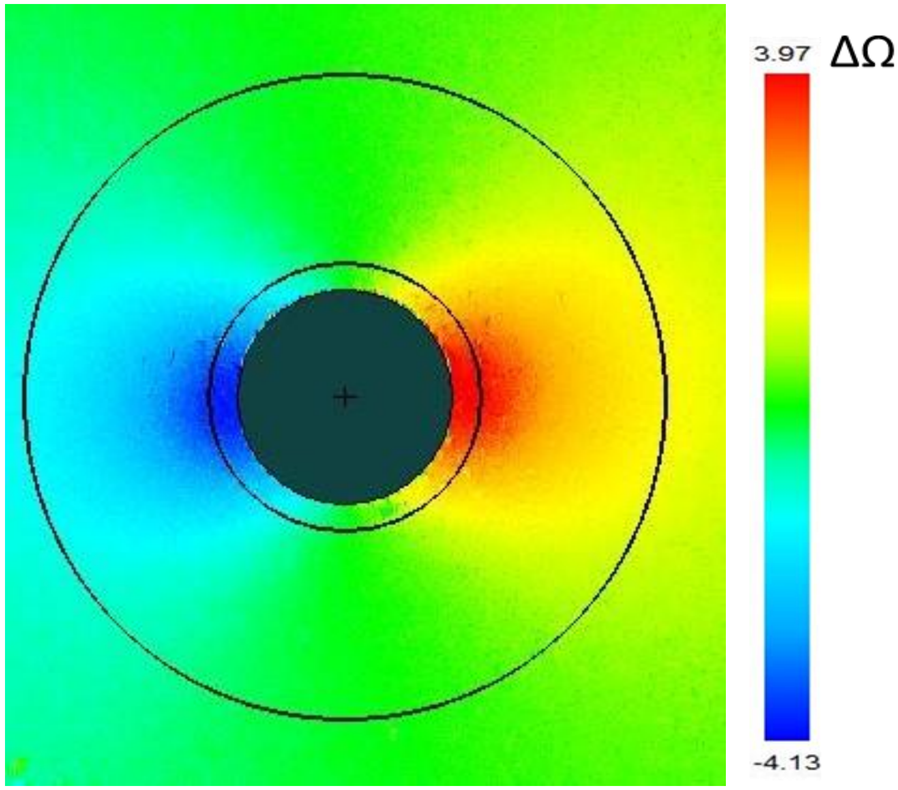

Figure 2.3 - ESPI measured displacement field

2.1.4 Computational Robustness and Accuracy

Scaling FEA generated deformation fields to match a measured deformation field has proven to be a very effective and robust means of measuring residual stress [17], [18]. By knowing what patterns can be expected various sources of noise can be separated and eliminated from the residual stress computation. Furthermore, this computational technique can be applied to a wide range of interferometric set-ups and devices.

Having established a robust computational method to determine residual stress the accuracy of the measurement mainly depends on the capability of the system to detect the displacement caused by hole drilling. This thesis aims to improve the accuracy and precision of detecting surface displacement.

2.2 Electronic Speckle Pattern Interferometry

Electronic Speckle Pattern Interferometry utilizes the interference properties of laser light to visualize and quantify very small (30nm-10μm) surface displacements [11]. Since its initial development in 1971 by Butters and Leendertz at Loughborough University of Technology, ESPI has found a wide range of application in the fields of solid mechanics, fluid dynamics, quality control, and biomedical engineering [20]. Today ESPI continues to be developed for an increasing number of applications to provide non-contact, non-destructive whole-field measurement solutions. With the developments of graphical computation, digital cameras, stepper motors, and miniature laser diodes new possibilities have presented themselves for ESPI. Mainly, the possibility of packaging an entire speckle pattern interferometer into a portable device, capable of taking measurements in the field, outside of tightly controlled laboratory conditions. The purpose of this thesis is to develop such an instrument to measure residual stress. Before we can understand the challenges of achieving this we must first understand the behavior of laser light and how the ESPI measurement is taken.

2.2.1 Laser Light

Unlike the light from the sun or a conventional light bulb, light emitted from a laser is highly monochromatic. This means that laser light consists of only a single wavelength. Figure 2.4 shows the spectrum of various light sources. White light consists of a wide range of wavelengths across the red, green and blue spectrum. A red LED emits a range of wavelengths in the red spectrum and laser light consists of a single wavelength. The degree of how monochromatic a light source is, is called coherence length and, as will be explained later, is extremely important achieving a reliable measurement.

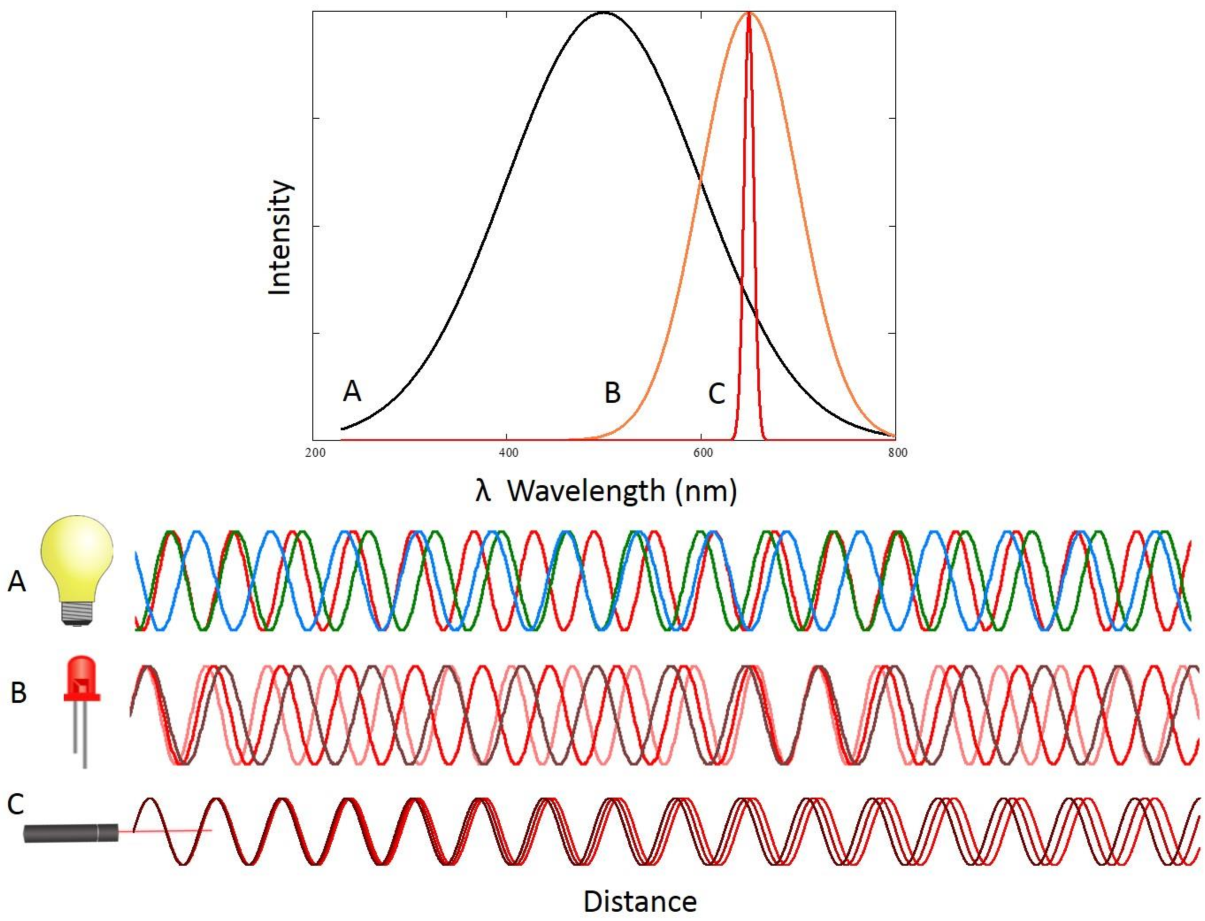

Figure 2.4 - Spectrum and wave-fronts of White light (A), Red LED (B), Single mode laser (C)

When an object is illuminated by coherent light it appears grainy as shown in Figure 1.7. The reason for this granular appearance is because of the interference phenomenon of light.

2.2.2 Interference Phenomenon

When two coherent light beams converge on a surface they combine constructively, by reinforcing each other's intensity or destructively, by diminishing it. This interaction is called interference and is governed by the phase difference in which the two beams combine [21], [22].

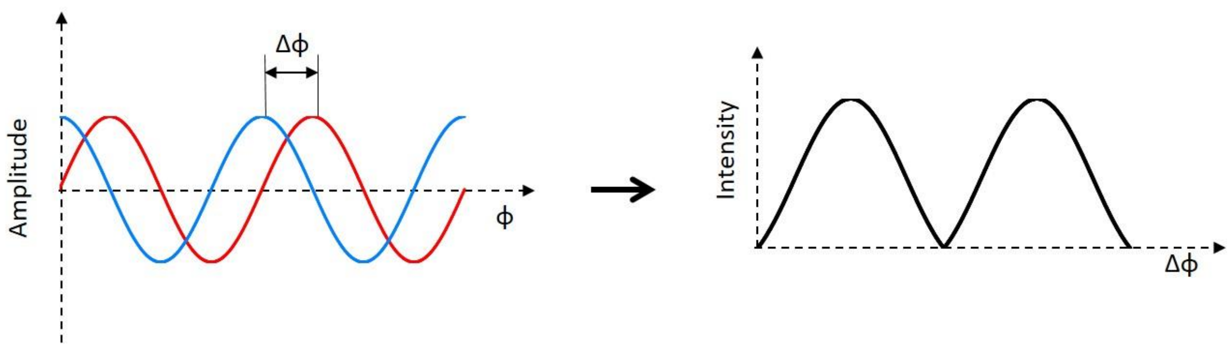

Figure 2.5 - Interference of waves depends on the phase difference at which they combine

The resulting intensity of the interference between two beams can be given by the interference formula [23]:

$$I = I_1 + I_2 + 2\sqrt{I_1 I_2}\cos(\Delta\phi) \tag{6}$$

where I_1 and I_2 are the intensities of the interfering light waves and $\Delta\phi$ is their phase difference.

If the two light waves originate from the same source, and hence with the same phase, than their phase difference is directly related to their path length difference, δ, by:

$$\delta = \frac{\lambda}{2\pi}\Delta\phi \tag{7}$$

where λ is the wavelength of the light source [16].

In effect, an interferometer translates the phase changes caused by surface displacements into intensity changes that can be measured. Since the wavelength of visible light is on the order of 500 nm a typical interferometer is capable of measuring displacements in the range of 30nm.

2.2.3 Speckle Effect

As mentioned previously, when an object is illuminated by a coherent light source it appears granular. One of the greatest revelations about this speckle phenomenon is that the speckle pattern carries information about the surface it illuminates [24], [25].

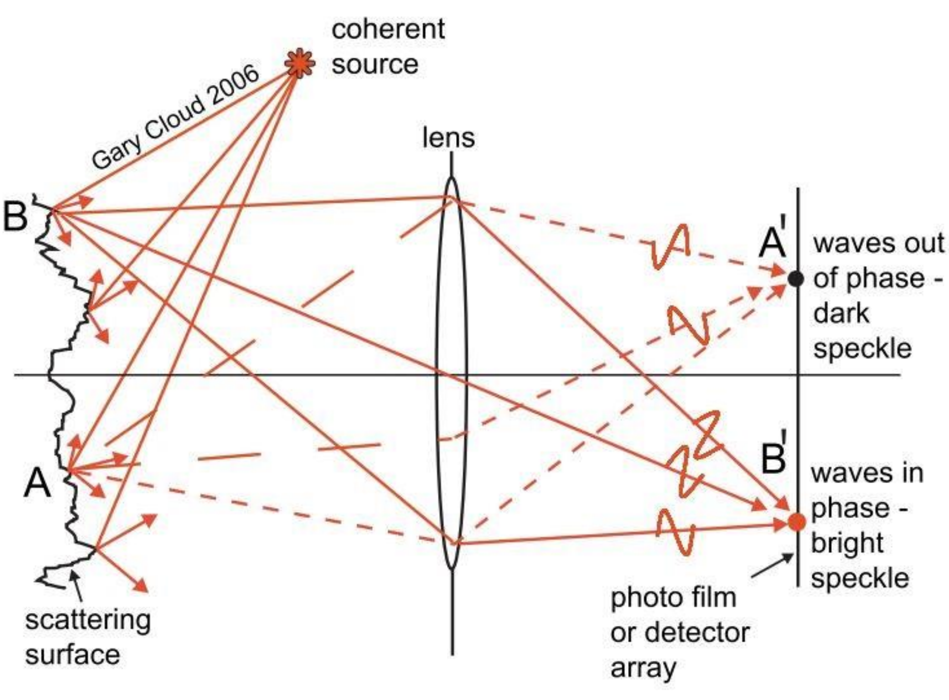

Figure 2.6 - Speckle pattern formation on an imaging plane. Adapted from [25]

When a coherent light ray strikes an optically rough surface it scatters diffusely. If a camera images a surface illuminated by coherent light, the scattered rays from each point on the surface converge on the image plane to form a speckle pattern. This occurs because the rays that converge at a point on the image travel different distances and cause a random interference on the imaging plane. The most important thing to understand is that each point on the surface corresponds to its own speckle on the image [25]. By photographing the speckles before and after surface deformation the phase difference at each point on the surface can be quantified. For visible light, λ = 400-700 nm, ESPI is sensitive to displacements as small as $\lambda/20$ = 30 nm [11].

2.2.4 ESPI Set-up

Figure 2.6 shows a typical ESPI arrangement.

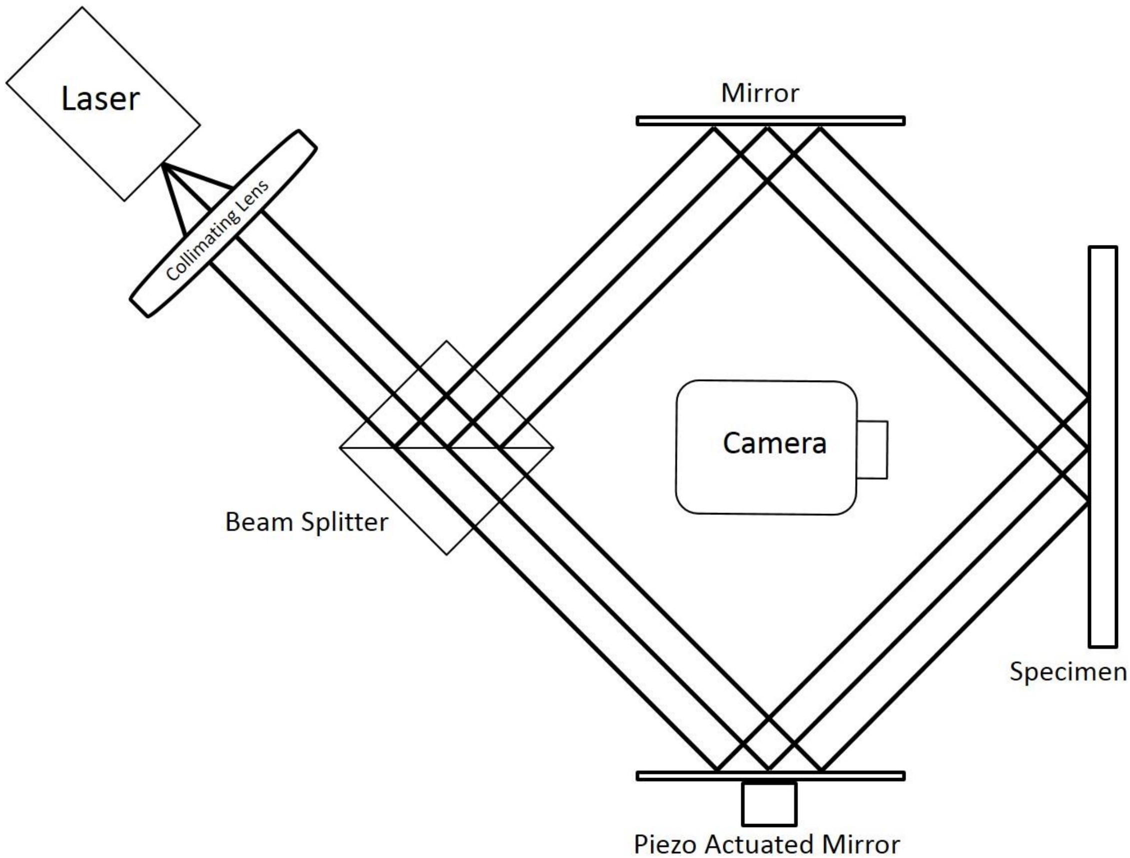

Figure 2.7 - Typical Arrangement of an Electronic Speckle Pattern Interferometer

An ESPI device consists of:

1. A coherent illumination source to produce a speckle pattern.
2. A 50/50 beam splitter, to divide the beam into two equal beams of half the original intensity.
3. A pair of mirrors to converge the beams onto the surface of the specimen; where, one of the mirrors is mounted on a piezoelectric actuator.
4. A camera to image the speckle pattern.

The digital camera images the speckle pattern on the surface of the specimen. The camera f-number is adjusted such that each speckle is the same size as a pixel. Therefore the intensity of each pixel represents the interference of a small area on the surface [26]. The size of this small area, a, depends on the magnification of the camera lens, M, and the size of the pixel p.

$$a = \frac{p}{M} \tag{8}$$

The two illumination beams are called the interferometer arms. Any relative movement between them causes a change in the speckle pattern. The mirror mounted on a piezoelectric actuator allows the interferometer to uniformly change the phase of each speckle. The phase shift, $\Delta\varphi$, caused by an advance, x, of the piezo mirror is:

$$\Delta\varphi = \frac{4\pi \sin\theta}{\lambda} x \tag{9}$$

where θ is the incidence angle of the illumination beam [16].

By stepping one of the interferometer arms by known amounts and detecting the phase shift, $\Delta\varphi$, the original phase difference, $\Delta\phi$, of each pixel is determined.

2.2.5 The Phase-Shifting Method

Figure 2.8 shows a 7×7 pixel image of a speckle pattern. Each pixel represents a speckle and therefore relates to a phase difference, $\Delta\phi$, between the rays which converge on it.

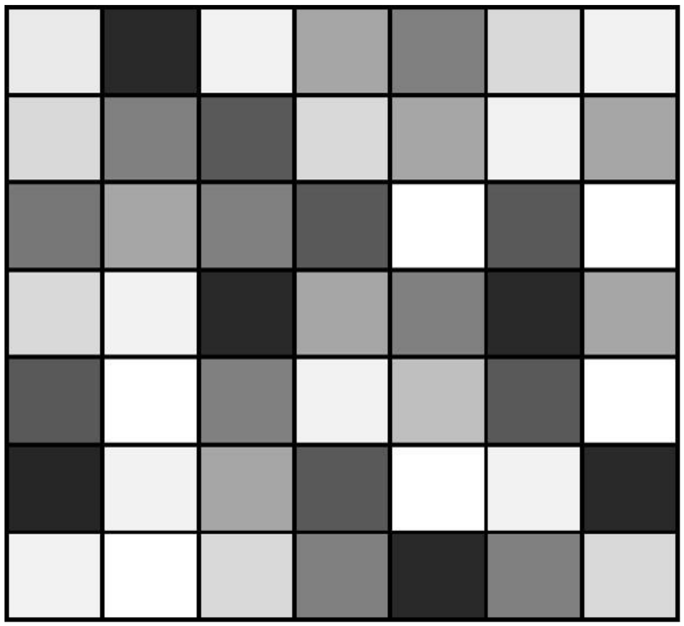

Figure 2.8 – 7x7 pixel image of a speckle pattern. Each pixel corresponds to one speckle

The intensity of a pixel is represented by equation (6) which can be rewritten as:

$$I = A + B\cos(\Delta\phi) \tag{10}$$

Where A is the mean intensity, B is the amplitude and $\Delta\phi$ is the phase difference that the phase stepping method aims to evaluate. By stepping the piezoelectric actuator the intensity of each pixel is changes. The shift can be represented mathematically by:

$$I = A + B\cos(\Delta\phi + \Delta\varphi) \tag{11}$$

The phase-shifting method consists of taking four images, each shifted by $+\frac{\pi}{2}$; resulting in four intensity measurements for each pixel:

$$\begin{aligned} I_1 &= A + B\cos(\Delta\phi + \frac{\pi}{2}) \\ I_2 &= A + B\cos(\Delta\phi + \pi) \\ I_3 &= A + B\cos(\Delta\phi + \frac{3\pi}{2}) \\ I_4 &= A + B\cos(\Delta\phi + 2\pi) \end{aligned} \tag{12}$$

Figure 2.9 show how the intensity change of a pixel can be used to fit the sinisoidal curve and determine the original phase difference, $\Delta\phi$, at that pixel.

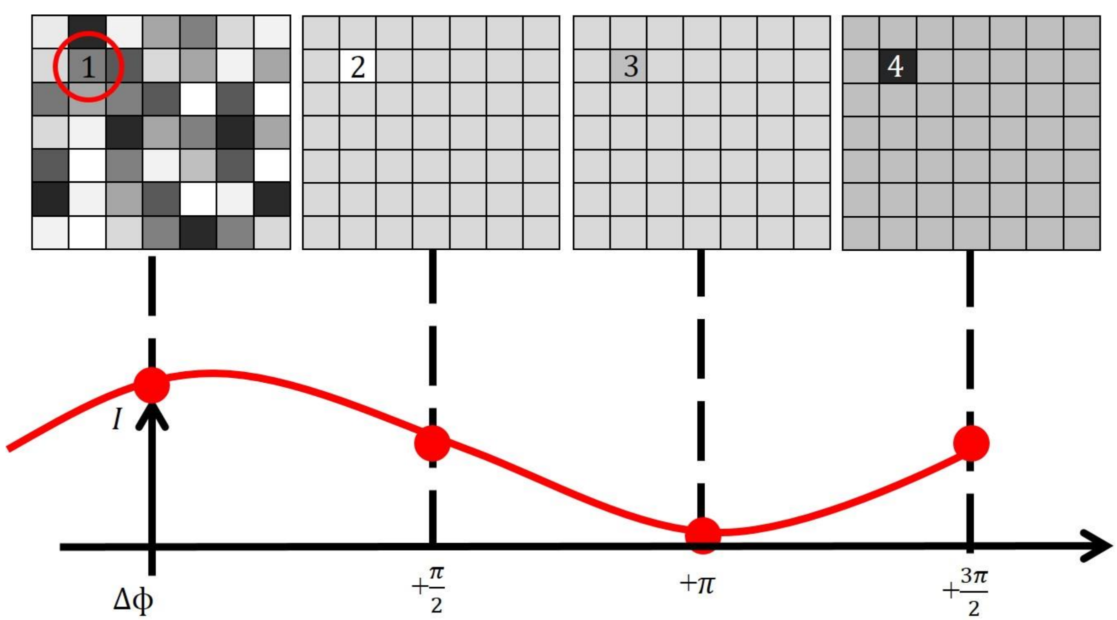

Figure 2.9 - Phase shifting by $\pi/2$ resulting in intensity changes of the speckle pattern.

Although 3 images are enough to curve fit the sinusoidal function a fourth image simplifies the calculation to a tangential function [16]:

$$\tan \Delta\phi = \frac{I_2 - I_4}{I_1 - I_3} \tag{13}$$

Now that the phase of each pixel has been determined for the reference set a hole is drilled into the specimen. The release of residual stress causes a displacement on the surface of the specimen. A second set of phase shifted images is taken and the phase of each pixel determined.

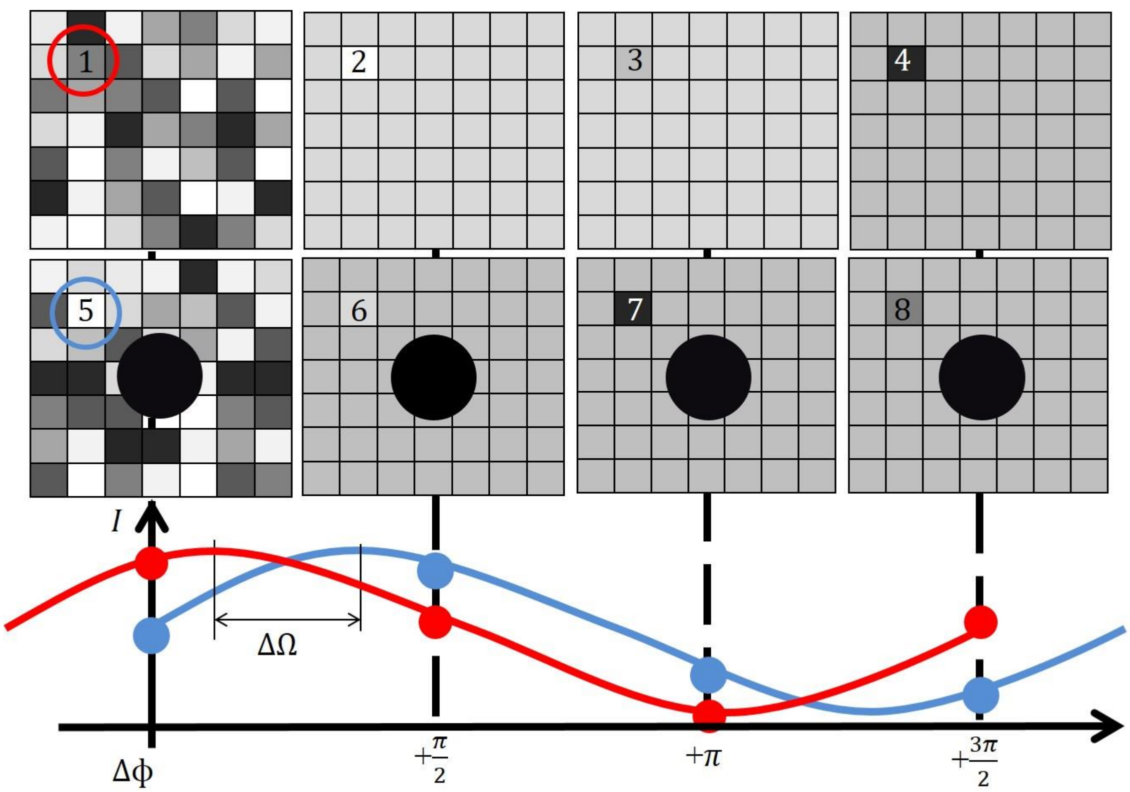

Figure 2.10 - Subsequent set of phase shifted images after hole drilling

The change in phase difference, $\Delta\Omega$, between the two sets of images is:

$$\Delta\Omega = \Delta\phi_2 - \Delta\phi_1 \tag{14}$$

This change in phase difference, $\Delta\Omega$, before and after hole drilling, corresponds to the displacement field, $D_{ESPI}(x, y)$, and is directly related to the residual stress in the specimen. As discussed in Section 2.1 this measured displacement field can be used to determine the residual stress in the body.

2.2.6 Phase Unwrapping

The change in phase difference, $\Delta\Omega$, lies in the range between $-\pi$ to π. The change in phase difference needs to be transformed into a continuous displacement field which represents the displacement due to hole drilling more appropriately and from which the residual stresses can be computed.

The change in phase difference for each pixel is plotted as a grayscale intensity ranging from 0 to 255. The resulting graphic known as a fringe pattern is shown in Figure 2.11a.

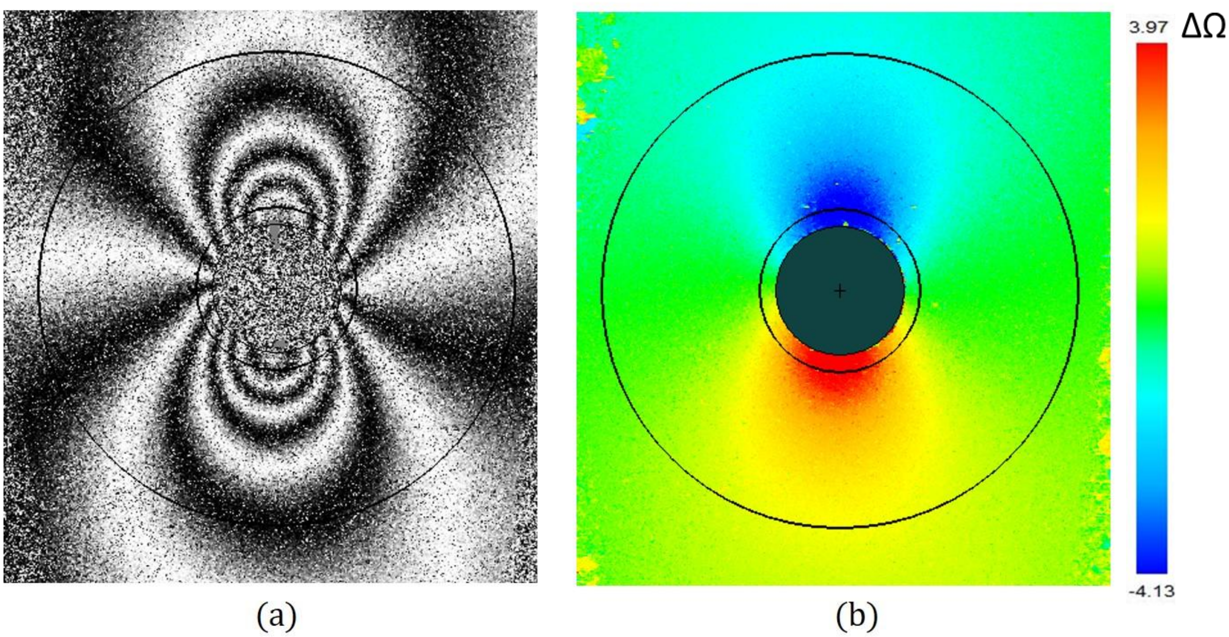

Figure 2.11 - a) Fringe pattern caused by plotting the change in phase difference of each pixel b) Unwrapped phase map

The width of each dark or white fringe represents a phase change of one wavelength, λ. Areas close to the hole have closely spaced fringes meaning there is several wavelengths of displacement right around the hole. Areas further away from the hole have only a few fringes meaning there is little movement there. To gain a more intuitive picture of the phase distribution a phase unwrapping algorithm is used to detect the sharp contrasts of the fringe pattern and splice them together [20], [27]. The resulting graphic is the phase map as shown in Figure 2.11b.

Using equation (7) a scalar displacement field can be generated. To determine the final displacement field, $D_{ESPI}(x, y)$, the direction of displacement needs to be evaluated.

2.2.7 Direction of Measurement

The geometry of an ESPI set-up governs the direction of measurement. This direction of measurement is called the sensitivity vector and is defined as the subtraction of the reference beam from the incident beam [16], [20]. This means that only displacements in the sensitivity direction will cause detectable phase changes. An in-plane interferometer such as the one described in Figure 2.7 has the following geometry:

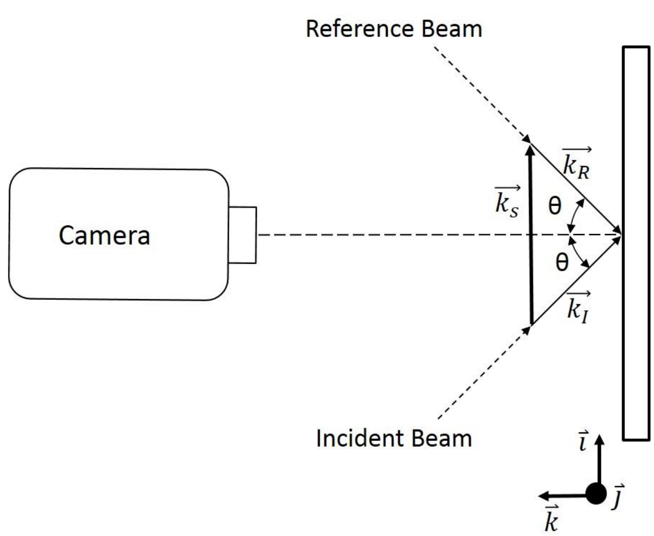

Figure 2.12 – Sensitivity vector of in-plane interferometer

The sensitivity vector can be defined mathematically as:

$$\overrightarrow{k_s} = \overrightarrow{k_I} - \overrightarrow{k_R}$$
$$\overrightarrow{k_R} = -\sin\theta\vec{\imath} - \cos\theta\,\vec{\jmath} \qquad (15)$$
$$\overrightarrow{k_I} = \sin\theta\vec{\imath} - \cos\theta\,\vec{\jmath}$$
$$\overrightarrow{k_s} = 2\sin\theta\vec{\imath}$$

If a point on the surface moves by $\vec{d} = d_x\vec{\imath} + d_y\vec{\jmath} + d_x\vec{k}$, only the $d_x\vec{\imath}$ component will contributes to the change in phase. This single direction of measurement limits the representation of the true displacement field caused by hole drilling [28].

2.3 Measurement Limitations

An ESPI interferometer is capable of translating speckle pattern intensity changes into phase maps. Each pixel in a digital phase map holds two pieces of information, a location on the specimen and its respective displacement along the sensitivity vector. Practically, displacements are rarely only in one direction. Nevertheless, a single axis ESPI interferometer is still capable of computing all three residual stress components, σ_x, σ_y, τ_{xy}. This is possible because each stress component affects the displacement along the axis of measurement independently via the effects of Poisson's Ratio. The accuracy of the measured residual stress components acting away from the measurement direction is roughly one third that of the residual stress component acting in the direction of measurement [29].

Various sources of noise also affect the quality of the phase map. It has been discovered that the quality of the illumination source is the most important factor to consider in producing a high quality phase map. This thesis aims to develop a device with reduced directional bias, capable of generating high quality displacement fields while maintaining portability and practicality.

2.3.1 Single Axis Measurements

Figure 2.13 show an 8×8 pixel displacement field around a 2×2 pixel hole in a body equally stressed in the X and Y axes. The displacement vectors are equal in magnitude and direction along the two axes.

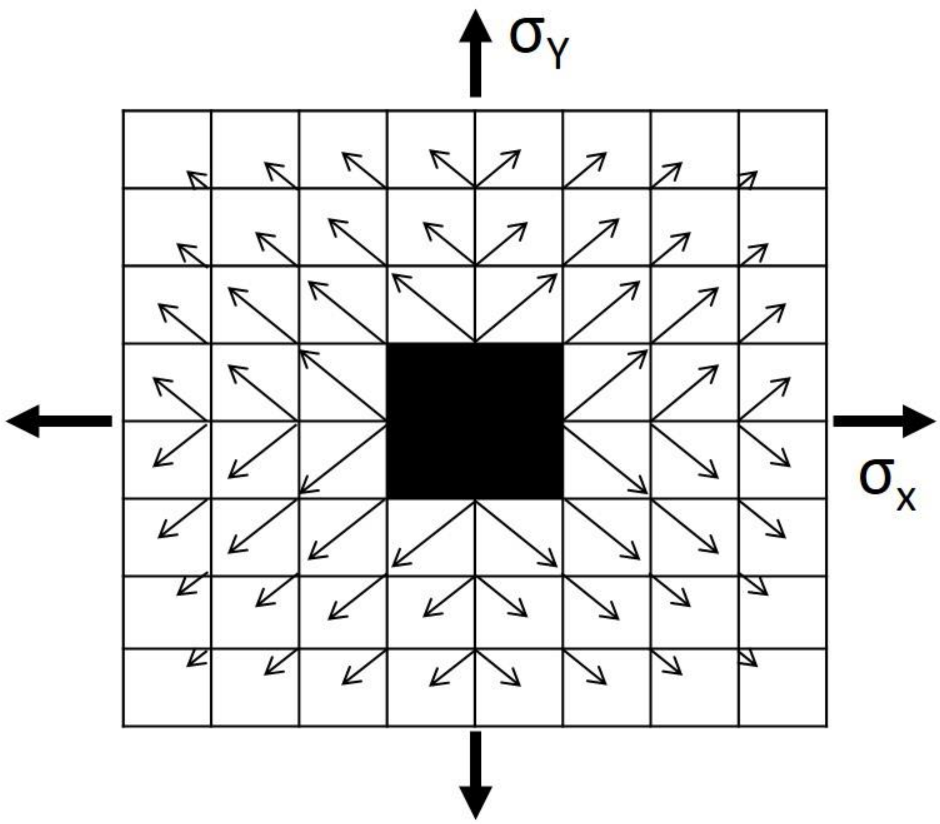

Figure 2.13 – Hole drilling displacement field of a body equally stressed in the X and Y axes

Figure 2.14a show the displacement field as it is measured by an ESPI system with a sensitivity vector along the X axis. The displacement vectors are projected along the sensitivity vector. Figures 2.14b and 2.14c show the individual contributions to the displacement measurement from σ_x and σ_y respectively. The contribution from σ_y to the final measurement is only through the effects of Poisson's Ratio and is one third smaller in magnitude than the contribution from σ_x. This phenomenon results in the evaluation of σ_y to be significantly less accurate than the evaluation of σ_x.

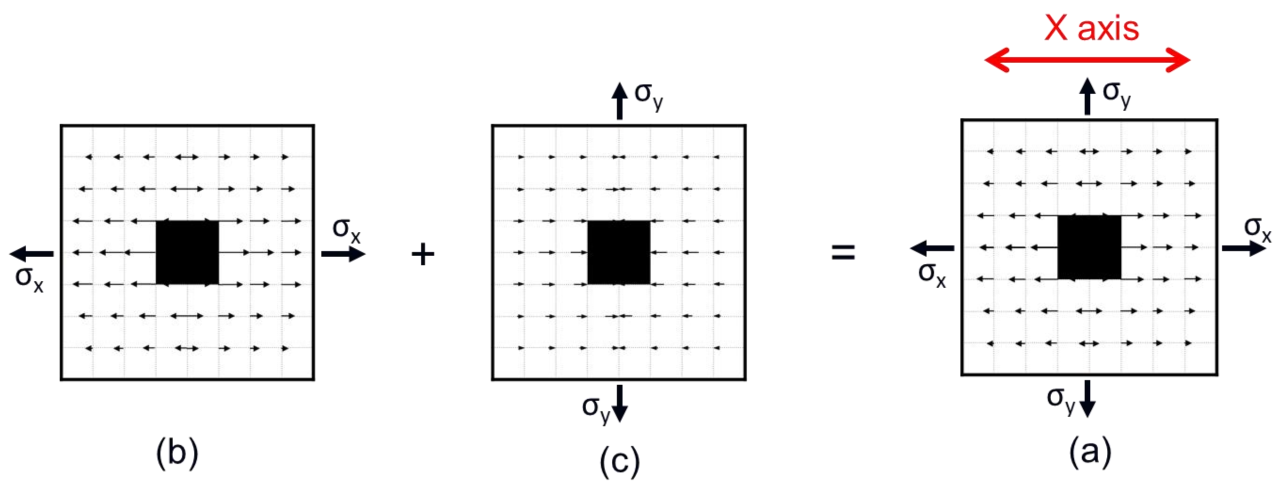

Figure 2.14 - a) Displacement field as measured by an X axis interferometer b) Contribution to the displacement measurement byσ_x c) Contribution to the displacement measurement by σ_y

To address this problem, this work has developed an interferometer with dual axis sensitivity, capable of measuring σ_x, σ_y, τ_{xy} with equal accuracy.

2.3.2 Dual Axis Measurements

An interferometer arrangement with two orthogonal measurement axes has two major advantages over a single axis interferometer. Firstly, such an interferometer measures the displacement caused by all three residual stress components, σ_x, σ_y, τ_{xy} directly, providing completed isotropic sensitivity. The addition of any subsequent axes (third axis, fourth axis, etc.) will not provide any additional in-plane sensitivity. Secondly, the measurement from each axis is combined to form a displacement field, $D_{ESPI}(x,y)$, with twice the amount of vectors. Each pixel in a dual axis phase map holds three pieces of information, a location on the specimen and two displacements along the sensitivity vectors. This increased amount of data improves the reliability of the least squares computation and the overall precision of the measurement [28]. Preliminary dual axis experiments have shown an improvement in measurement accuracy and precision [27], [28]. However, works still remains in developing a more permanent optical arrangement where the benefits of dual axes residual stress measurement can be explored in greater detail.

2.3.3 Measurement Quality

Measurement quality is defined by the ability of the ESPI device to translate pixel intensity into a reliable displacement map. This metric is called visibility and is the ratio of a pixel's mean intensity, A, and its amplitude, B. Visibility, V, is evaluated during phase shifting. As the reference beam is stepped each pixel's intensity change is compared to its mean intensity. Figure 2.15 illustrates the intensity changes of high and low visibility pixels.

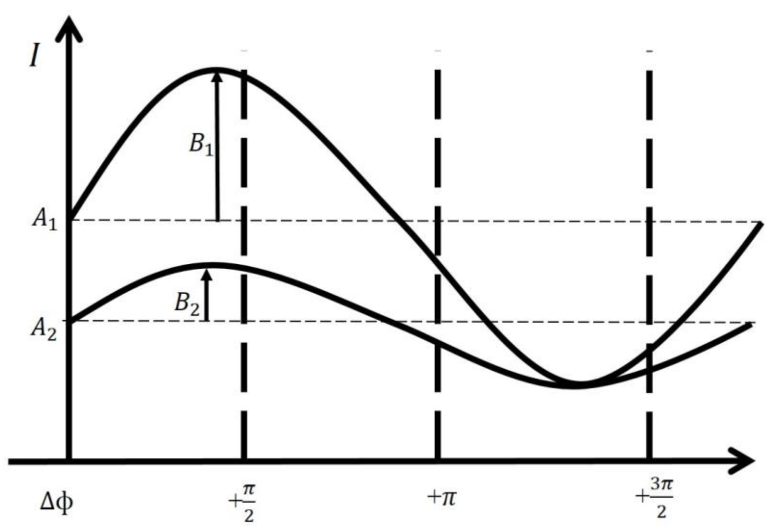

Figure 2.15 - High and low modulated signals

In effect the visibility measures how sensitive the ESPI device is to phase changes [27].

Mathematically it is defined:

$$V = \frac{B}{A} \tag{16}$$

$$V = \frac{\sqrt{(I_1 - I_3)^2 + (I_2 - I_4)^2}}{I_1 + I_2 + I_3 + I_4} \tag{17}$$

Figure 2.16 shows how pixels of low visibility are evaluated on a phase map. Pixels in green are of low quality ($V \leq 0.1$) whereas white pixels are of good useable quality ($V > 0.1$) [27]. This phase map exhibits bands of low and high quality. An interesting phenomenon which will be explored in detail in Chapter 3.

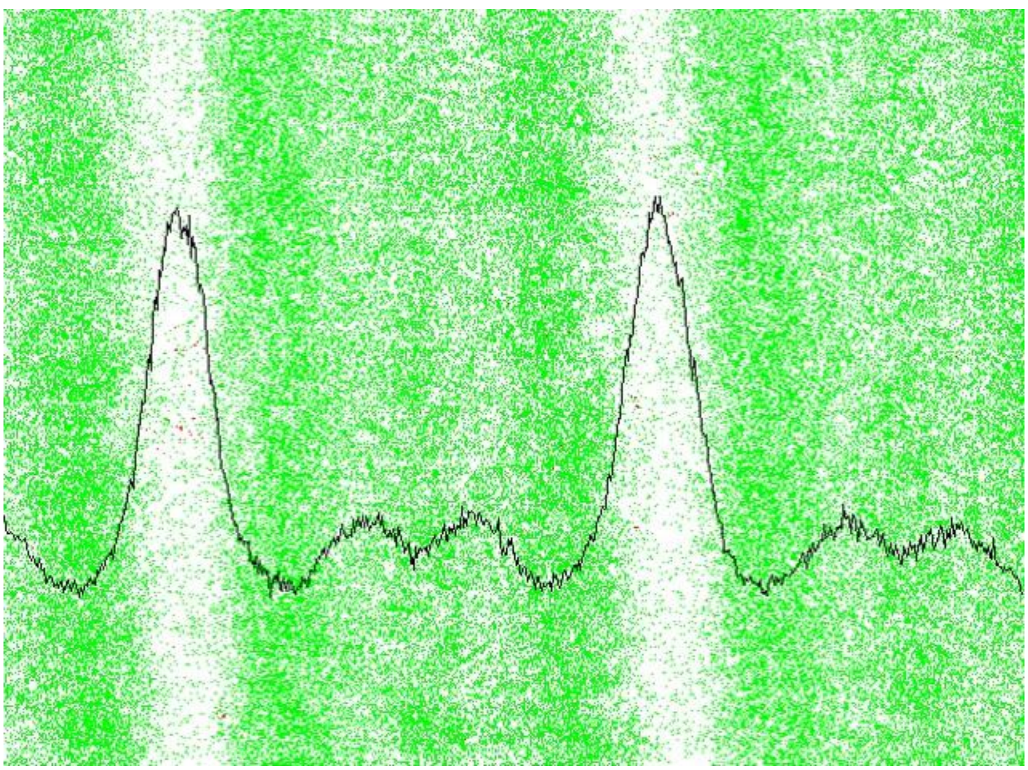

Figure 2.16 - Evaluation of pixel visibility. Pixels in white are of good visibility and pixels in green are of bad visibility

To achieve a reliable measurement of high quality there are several factors to consider; such as environmental disturbances, pixel to speckle size ratio and surface discontinuities. The most important factor, however, is the coherence of the illumination source. As explained in section 2.2.1, coherence is the measure of how monochromatic a light source is. The coherence defines the ability of the light to interfere. Light of insufficient coherence will fail to create intensity changes during phase shifting and will directly decrease the visibility of the phase map.

2.3.3.1 Environmental Disturbances

Rigid body movements or temperature drifts during ESPI measurements introduce changes in the speckle pattern that are unrelated to residual stress displacements. As described in section 2.1, using the power of the least squares technique, rigid body movements and temperature drifts can be separated from residual stress displacements. This capability of ESPI to computationally deal with environmental disturbances has increased robustness for in-field measurements.

2.3.3.2 Speckle Size

Speckle size is important in achieving a reliable measurement. The size of the speckles, S, is governed by the magnification, M, and f-number, f, of the imaging system as outlined by the following equation [26]:

$$S = \lambda \frac{f}{M}(1 + M) \tag{18}$$

For the highest quality measurements speckle size, S, should be adjusted to match pixel size. That way, each pixel caries information about only one speckle [27]. If the speckles were too small then each pixel will average out the intensity of several speckles which would effectively reduce the quality of the measurement.

2.3.3.3 Surface Discontinuities

Ideally, a displacement map should be continuous and smooth. Thus the value of phase change at each pixel should not vary greatly from adjacent pixels. Any discontinuities on the surface such as scratches or marks will cause a sharp irregularity in the intensity measurements which will affect the speckle pattern. Blazer, the signal processing program used for this work, adopts a pixel examination technique to compare each pixel with adjacent pixels for sharp changes in phase. The algorithm only uses pixels with sufficiently smooth continuity for the measurement [27].

2.3.3.4 Coherence Length

Environmental disturbances, speckle size and surface discontinuities are indeed important factors to consider for high quality ESPI measurements; and several effective techniques have been developed to control these potential sources of noise. By far however, the most important factor to consider is the coherence of the illuminations source. The coherence of the illumination source governs the ability of the light to interfere and provide a detectable signal. For that reason, ESPI equipment typically uses high quality, high coherence lasers. However, such lasers are generally bulky, delicate and not suitable for compact portable equipment. A promising alternative to such laser sources are miniature laser diodes. Their small size and moderate cost has made them widely used in many everyday products such as optical drives, computer mice, photocopiers, optical scanners, just to name a few. Their use in interferometry however, has been severely limited due to their low coherence. The coherence of a laser diode is governed by its spectral output. A laser diode has a spectral output shown in Figure 2.17; where several closely separated wavelengths are emitted simultaneously [30]. The separation of the emitted wavelengths, $\Delta\lambda$, is governed by the physical construction of the laser. The central wavelength is governed by the temperature and current of operation. As the temperature or current varies the central lasing wavelength hops from one wavelength to the next [31].

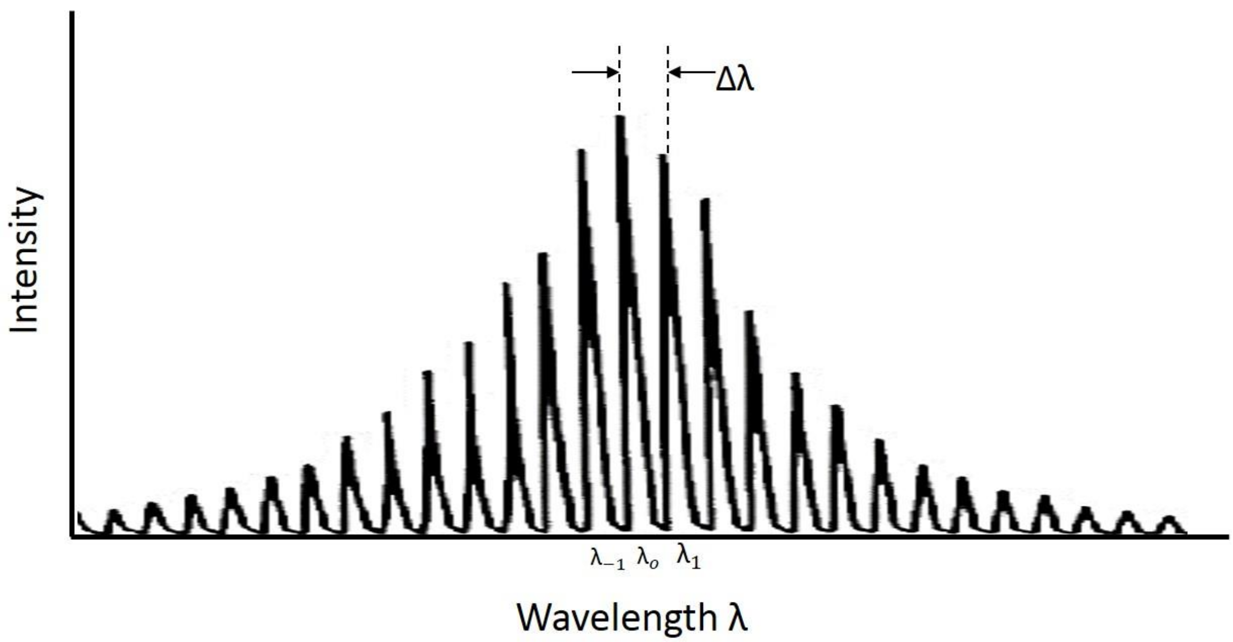

Figure 2.17 - Spectral output of a laser diode, adapted from [30]

When dealing with light measurement in the spatial domain, such as interferometry, it is convenient to measure coherence in units of length. This metric is called coherence length and is defined as the length of the laser beam which exhibits coherent properties. These properties allow the laser beam to create visible interference [32].

Figure 2.18 shows the propagation of a light beam from a laser diode. The emitted waves start out in phase and as they propagate through space they become increasingly out of phase with one another. As they continue to propagate they come back into phase. An interference signal can only occur in the area of the beam that is in phase i.e. a coherent area of the beam.

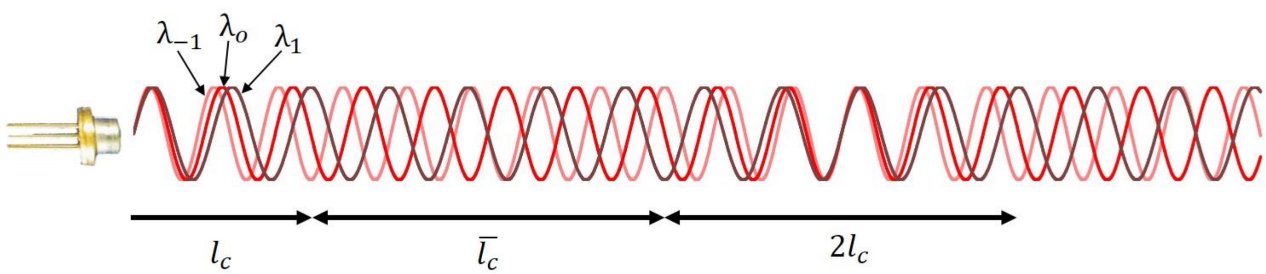

Figure 2.18 – Wave-fronts emitted by a laser diode

The degree the waves can be out of phase and still provide sufficient visibility for interferometric measurement is a function of the interferometer. Hence, coherence length, l_c, depends on the spectral output of the laser and the coherence sensitivity of the interferometer, g. Mathematically the coherence length of a laser can be represented by:

$$l_c = \frac{2g\lambda_o^2}{N\Delta\lambda} \tag{19}$$

where N is the number of wavelengths outputted by the laser. Naturally, the larger the number of outputted wavelengths the shorter the coherence length. The coherence sensitivity, g, is typically 1/2; when the peak of the shortest wavelength coincides with the trough of the longest wavelength and vise versa. At this area of the beam the destructive interference of the shortest wavelength coincides with the constructive interference of the longest wavelength resulting in no change of intensity [33]. As seen in Figure 2.18 coherence length is periodic along the length of the beam. The incoherent area of the laser beam, $\overline{l_c}$, is found between two coherent areas and is a function of the coherence sensitivity, g:

$$\overline{l_c} = \frac{l_c}{g} = \frac{2\lambda_o^2}{N\Delta\lambda} \tag{20}$$

For a typical interferometer of $g = 1/2$, the incoherent area, $\overline{l_c}$, is twice the coherence length, $2l_c$. Typically laser diodes have a coherence length of 2mm. Which means that the optical geometry of an interferometer using a laser diode ought to be within 2mm. Practically this is a challenging thing to do.

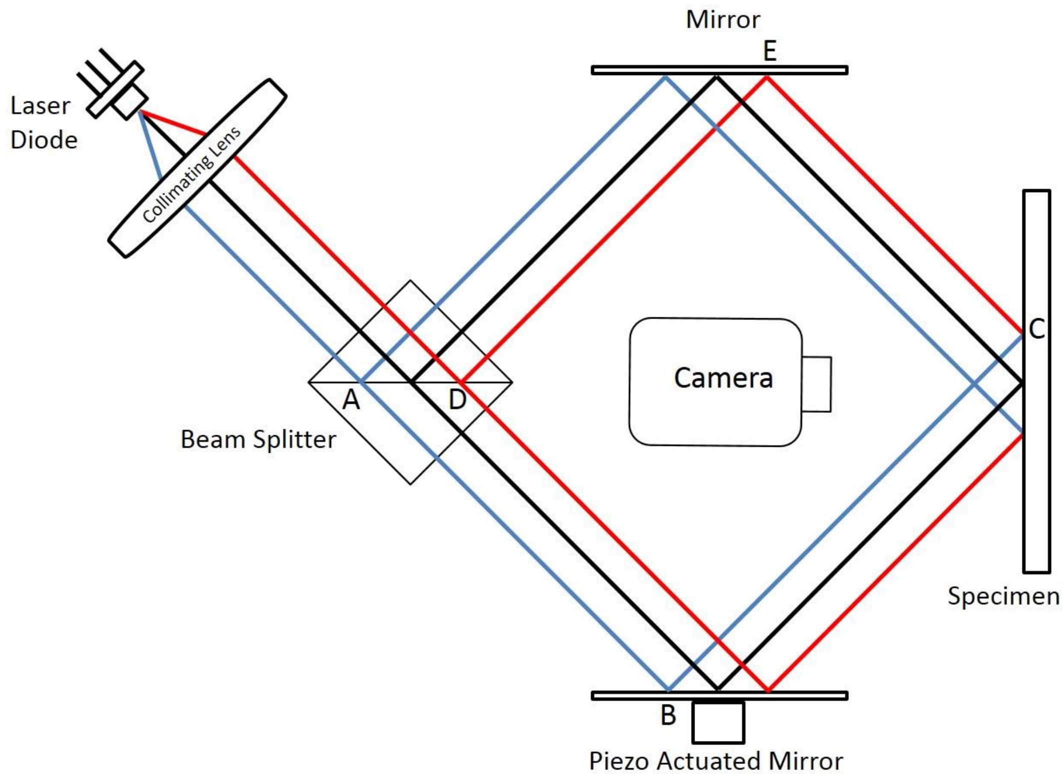

Figure 2.19 - ESPI arrangement using a laser diode

Figure 2.19 shows an ESPI arrangement using a laser diode as the illumination source. Due to the nature of the beam splitter the rays away from the central ray, shown in blue and red, converge on the surface of the specimen outside of their coherence length, where:

$$(\overline{\mathrm{AB}} + \overline{\mathrm{BC}}) - (\overline{\mathrm{DE}} + \overline{\mathrm{EC}}) > l_c \tag{21}$$

It is the aim of this thesis to develop a practical device capable of using compact laser diodes to provide high quality interferometric measurements.

2.4 Conclusion

Combining the displacement sensitivity of ESPI and computational power of FEA has proved an effective way of measuring residual stress [16], [17]. However, the precision of these measurements is limited due to the single sensitivity axis typical ESPI systems have [27], [28], [29]. Furthermore, ESPI systems rely on highly coherent sources of illumination to provide reliable measurements. Such laser sources are bulky and sensitive to environmental conditions. These dependencies limit ESPI measurements to a laboratory setting. Laser diodes are miniature laser sources that offer a potential alternative for compact ESPI equipment. However, their low coherence length severely limits their application for interferometry. To alleviate this problem an alternative optical arrangement is proposed that uses a diffraction grating instead of a traditional beam splitter. The diffraction grating allows for the interference to occur within the short coherence length of the laser diode providing measurements of extremely high quality. Additionally, this optical arrangement provides complete in-plane sensitivity.

Chapter 3: ESPI Using a Diffraction Grating

Matias R. Viotti and Armando Albertazzi from the Metrology and Automation Laboratory at the Universidade Federal de Santa Catarina have been successful at constructing a portable ESPI instrument for residual stress measurements using a laser diode [14]. Due the achromatic character of the diffraction grating configuration they used, the visibility of their measurements is independent of the laser diode wavelength, λ. However, it is dependent on its coherence length, l_c, and as such the visibility is noisier than typical table top ESPI instruments. To improve their measurement quality the laser diode is stabilized by tuning its current [15]. However, even at optimal current operation a laser diode's coherence length is still in the 2-4mm range which requires a very precise and impractical constructional tolerance.

As discussed in Section 2.3.2.4 the quality of the displacement measurement depends on the ability of the interferometer to align the beam paths such that they interfere in the coherent rage of the illumination source. If a laser diode is to be used the path length difference, δ, of the interfering beams has to be within the coherence length of the laser diode, typically 2-4 mm. This work proposes the use of a diffractive grating along with geometrical tuning technique to align the beam paths such that they interfere within their coherence length and provide high quality displacement measurements without the stringent requirement for precise constructional tolerances.

3.1 Diffraction Grating Fundamentals

A diffraction grating is an optical element with very finely spaced grooves as shown in Figure 3.1a. A monochromatic light ray passing through a diffraction grating splits into three rays as shown in Figure 3.1b.

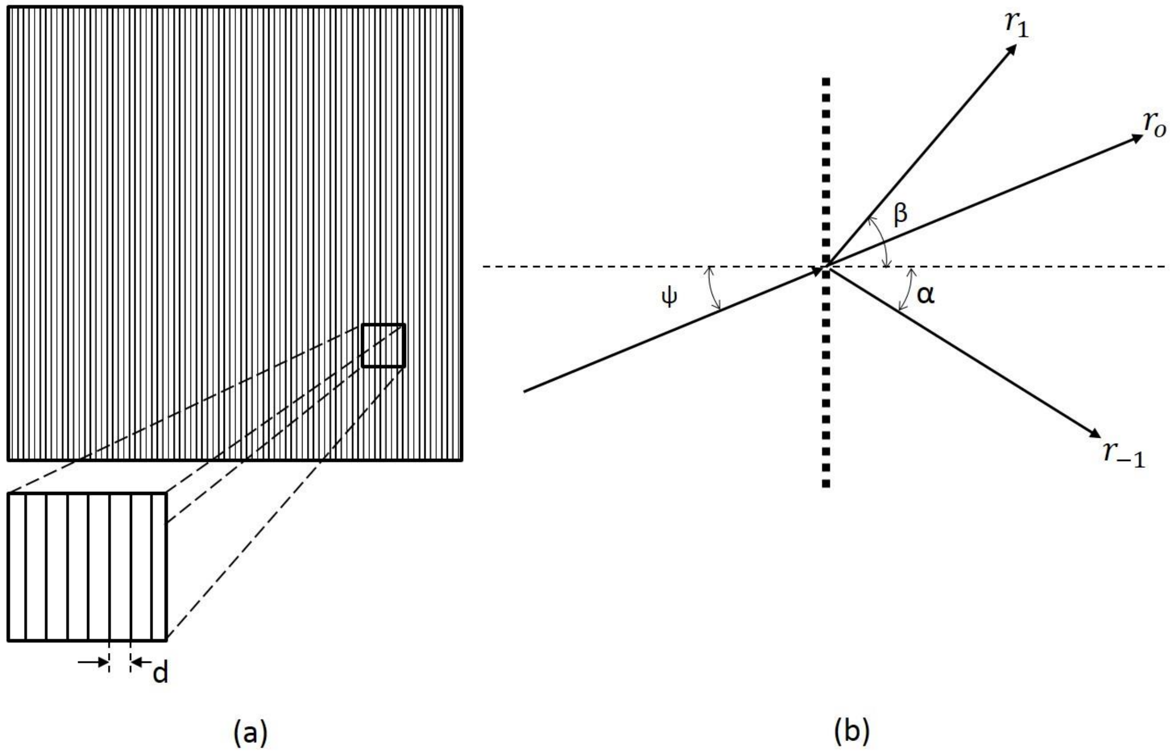

Figure 3.1 - a) Diffraction Grating front-view b) Plan-view of ray transmission

The transmitted angles, α and β, depend on the groove spacing, d, the wavelength of the ray, λ, and the angle of incidence, ψ. Mathematically this is given by Bragg's equation:

$$\sin\beta = \frac{\lambda}{d} - \sin\psi \tag{22}$$

$$\sin\alpha = \frac{\lambda}{d} + \sin\psi \tag{23}$$

When the ray is perpendicular to the diffraction grating the incident angle, ψ is very small and Bragg's equation can be simplified to:

$$\sin\psi \approx 0$$

$$\sin\alpha = \sin\beta = \sin\theta = \frac{\lambda}{d} \tag{24}$$

Where θ is the diffraction angle and angle of illumination as introduced in section 2.2.4 [34].

3.2 System Set-up

Using the rules of diffraction, an ESPI interferometer, as shown in Figure 3.2, is set up.

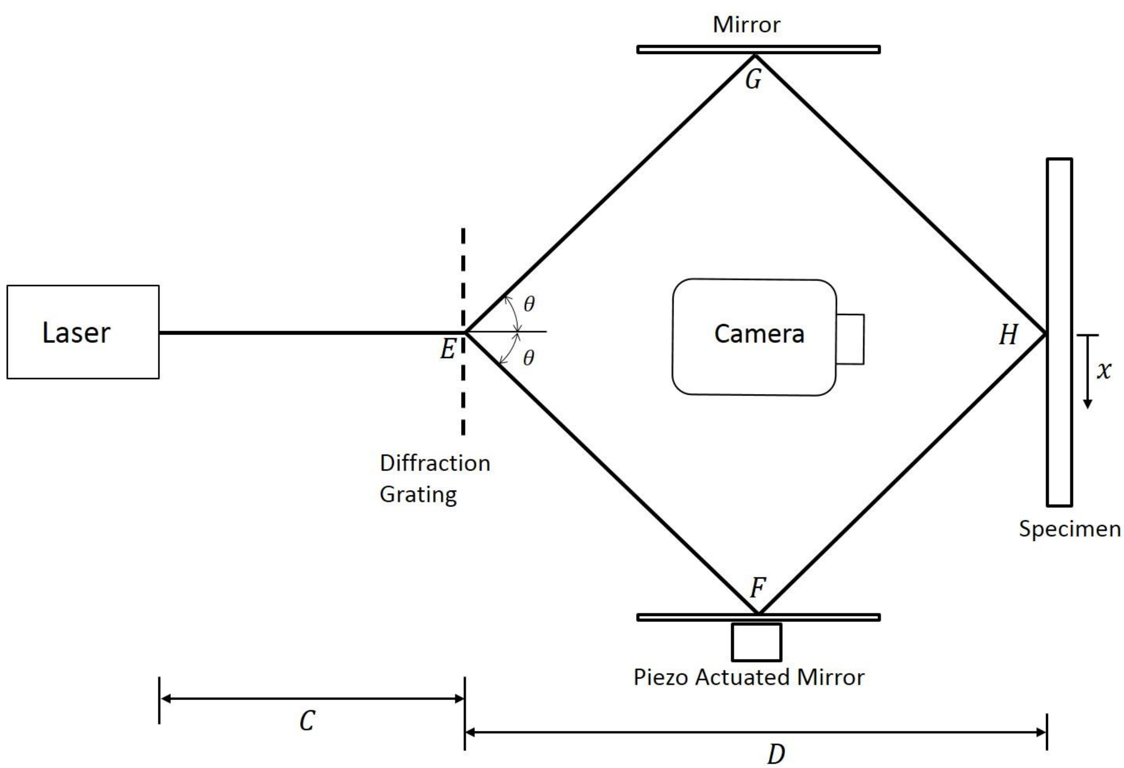

Figure 3.2 - Initial diffraction grating interferometer arrangement

Measurements using this configuration were taken and Figure 3.3 shows the resulting distribution of Visibility.

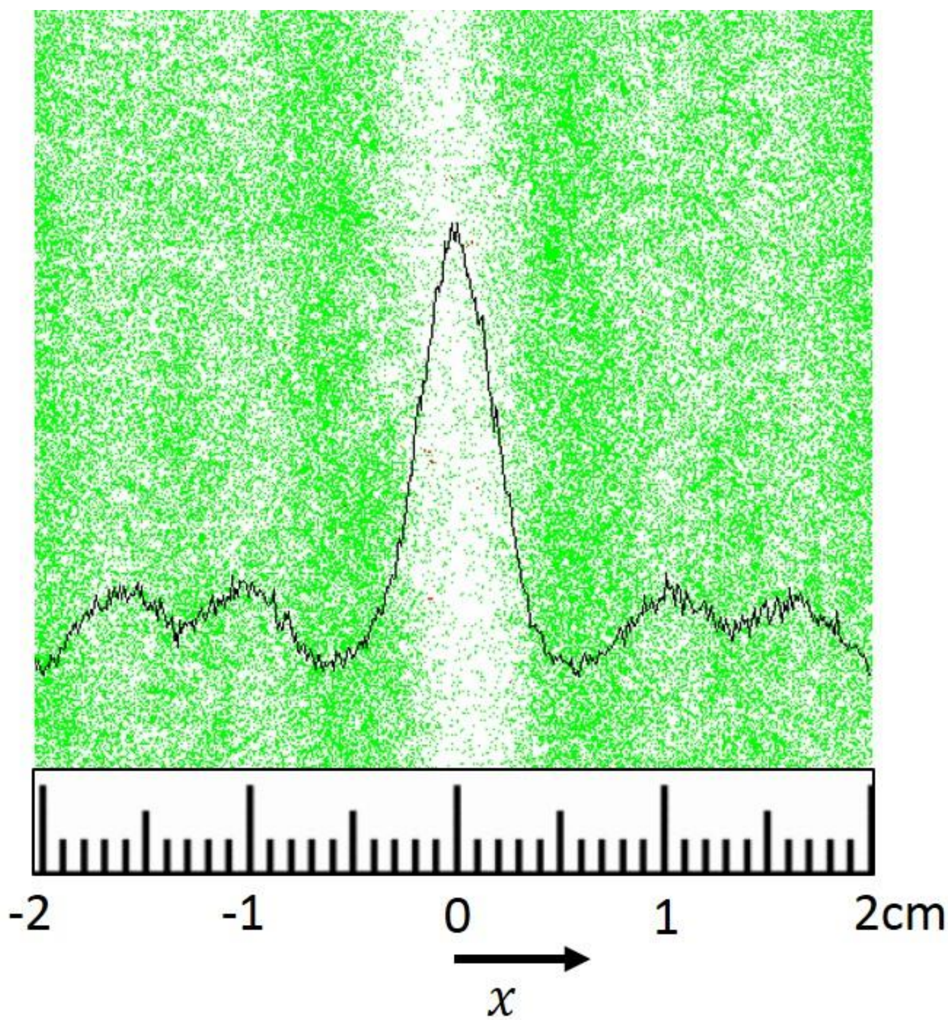

Figure 3.3 - Measurement distribution of visibility

As discussed in section 2.3.2 white pixels indicate good measurement visibility whereas green pixels bad visibility. Since visibility is directly related to the path length difference between the interfering rays it is deduced that the rays interfere at varying distances across the width of the image and at equal distances along its height. These bands of good and bad visibility are named "coherence bands" as the rays interfere within their coherent zone where white pixels are observed and non-coherent zone where green pixels are observed.

3.3 Coherence Bands

Upon further investigation of the optical geometry of the diffraction grating interferometer it is observed that the diverging illumination angle of the laser diode causes the path length difference to increase across the width of the image.

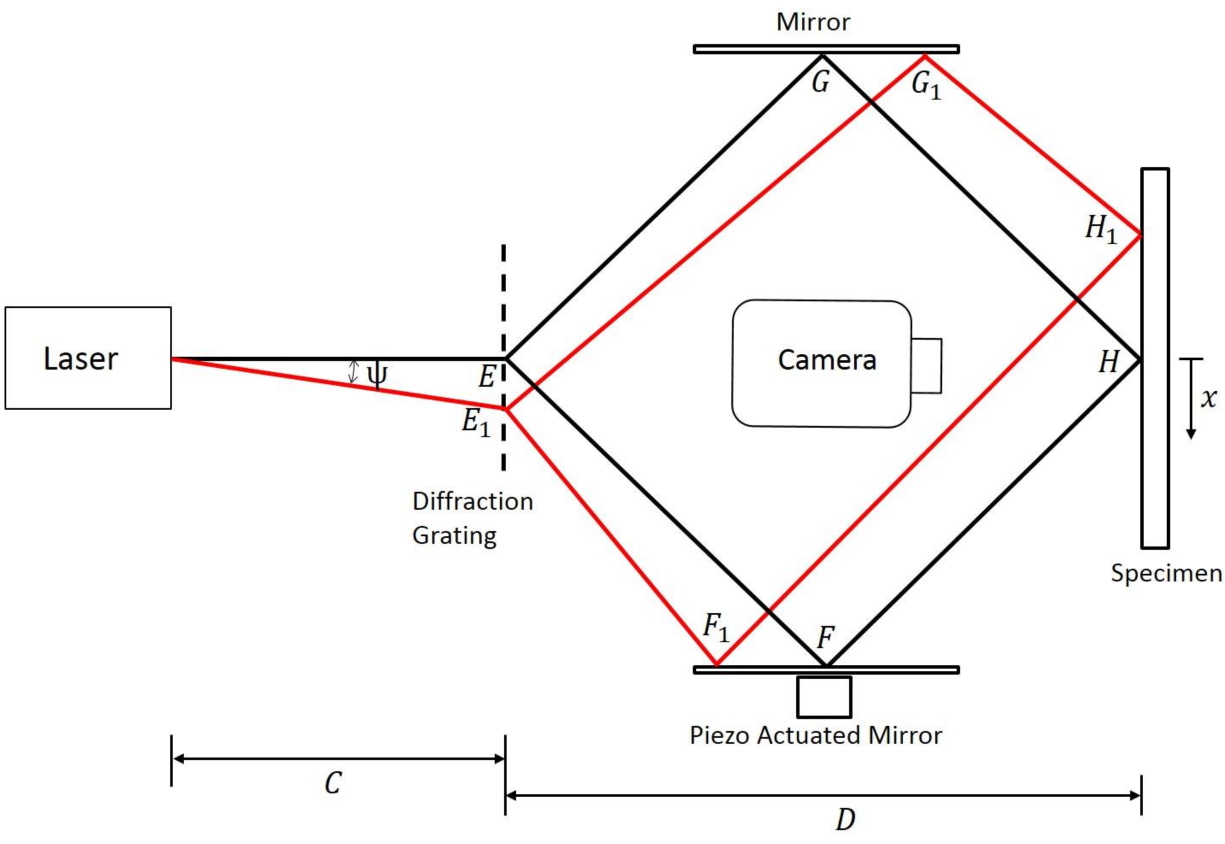

Figure 3.4 - Ray paths across width of image

Figure 3.4 shows this effect. The interferometer is adjusted such that the central path lengths are equal, $\overline{EF} + \overline{FH} = \overline{EG} + \overline{GH}$. A diverging ray is incident on the diffraction grating at angle, ψ, and its diffracted rays do not maintain equal path lengths, $\overline{E_1F_1} + \overline{F_1H_1} \neq \overline{E_1G_1} + \overline{G_1H_1}$. The center of the coherence band is where the rays interfere within their coherent zone. The path length difference between the interfering waves increases along the width, x, of the image. The relationship between the path length difference, δ, along the horizontal width of the image, x, is given by:

$$\delta = \frac{2\sin\theta}{1 + \frac{C}{D} cos^3\theta}\, x \tag{25}$$

where θ is the diffraction angle and angle of illumination as introduced in section 2.2.4. C and D are the distances of the optical arrangement, as shown in Figure 3.4.

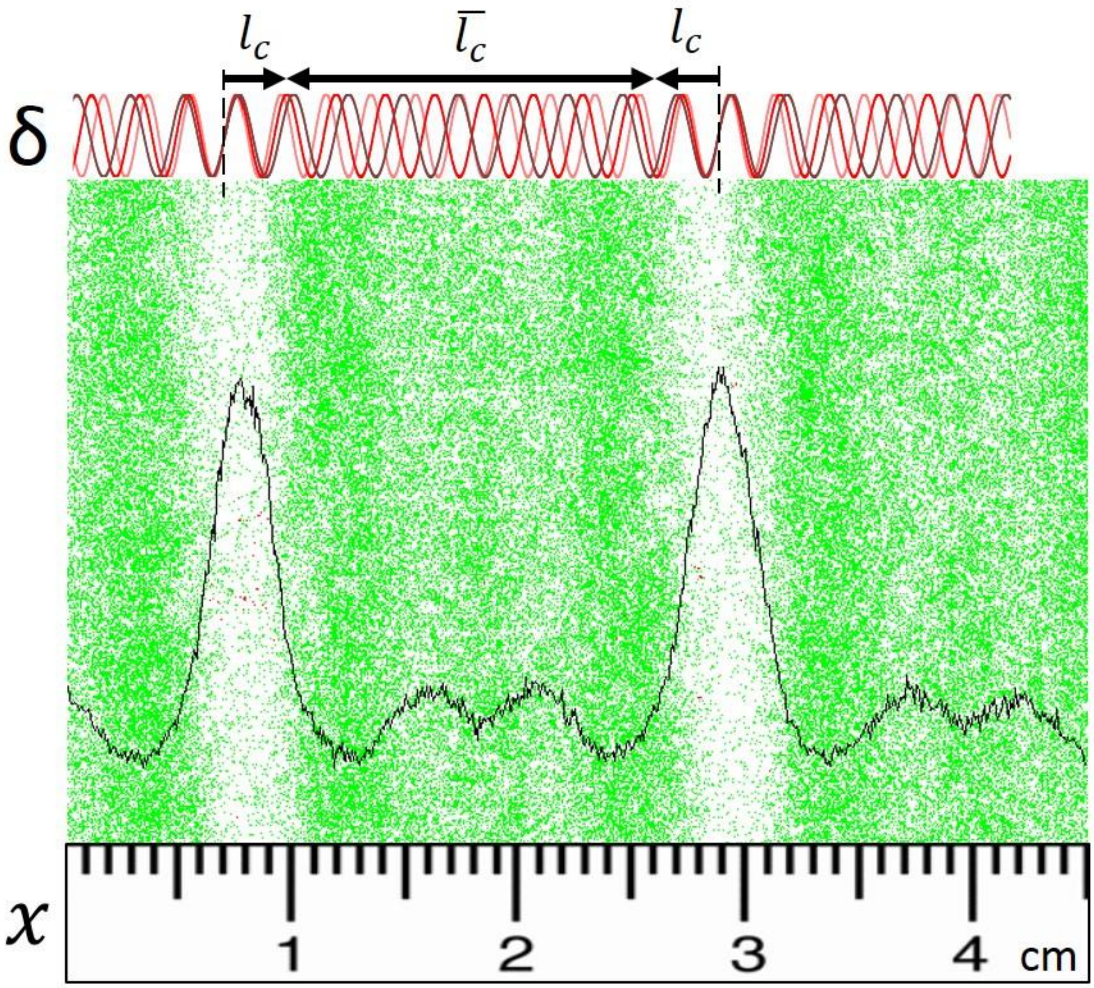

Figure 3.5 - Periodic coherence bands formed across width of image

As explained in Section 2.3.2.4 the coherence along the length of a laser beam is periodic. Due to this characteristic as the path length difference, δ, increases the rays begin interfering within a higher order coherence zone and a second coherence band is produced. Figure 3.5 shows the relationship between the coherence bands and the corresponding path length difference. It is observed that half a coherence band, l_c, is one eighth of the non-coherence band, $\overline{l_c}$. Using equation (20) the coherence sensitivity, g, of the interferometer is shown to be one eighth.

$$g = \frac{l_c}{\overline{l_c}} = \frac{1}{8}$$

Using this relationship the center to center distance between two coherence bands, X_c, is computed to be $10l_c$.

$$X_c = 2l_c + \overline{l_c} = 10l_c$$

Figure 3.5 was taken with the following parameters:

Laser Diode: Mitsubishi ML520G54	Optical Geometry	Distance Between Coherence Bands
λ = 638 nm	D = 305 mm	X_c = 21 mm
	C = 507 mm	
	θ = 40°	

Table 3.1 - Diffraction grating interferometer measurement parameters

Substituting X_c and these parameters into equation (25)

$$10l_c = \frac{2\sin 40°}{1 + \frac{507}{305}cos^3 40°}\,21$$

$$10l_c = 15.45\ mm$$

$$l_c = 1.55mm$$

the coherence length of the laser diode is calculated to be 1.55mm.

Since coherence length is independent of the geometrical arrangement of the interferometer varying the optical geometry, C/D, should not change the computed coherence length. An experiment was conducted where the optical geometry, C/D, was varied and the resulting distance between the coherence bands, X_c, measured. Using equation (26) the coherence length was computed for each arrangement. Graph 3.1 shows that the computed coherence length of 1.55 mm (averaged) is independent of the geometrical arrangement, C/D, of the interferometer.

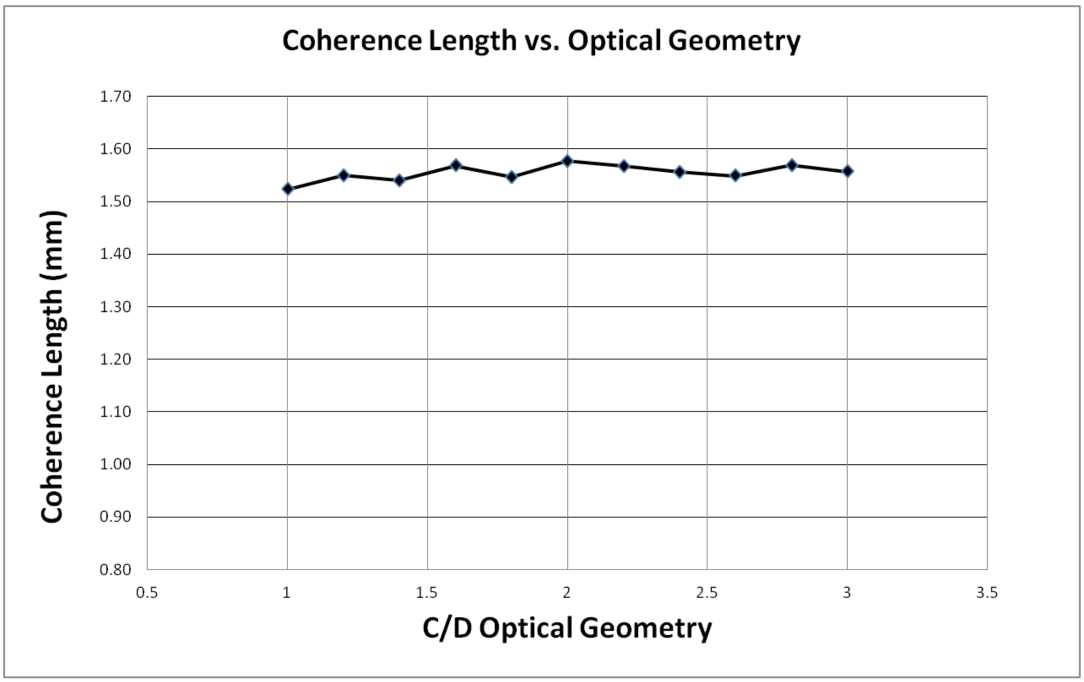

Graph 3.1 - Coherence length measurements at varying geometrical parameters

A Michelson interferometer was used to further validate the coherence length of the laser diode. Figure 3.6 shows the Michelson Interferometer arrangement. The mirror in one arm of the interferometer was moved in a series of 0.1mm steps over a 15mm range. At each step the average visibility, V, was computed.

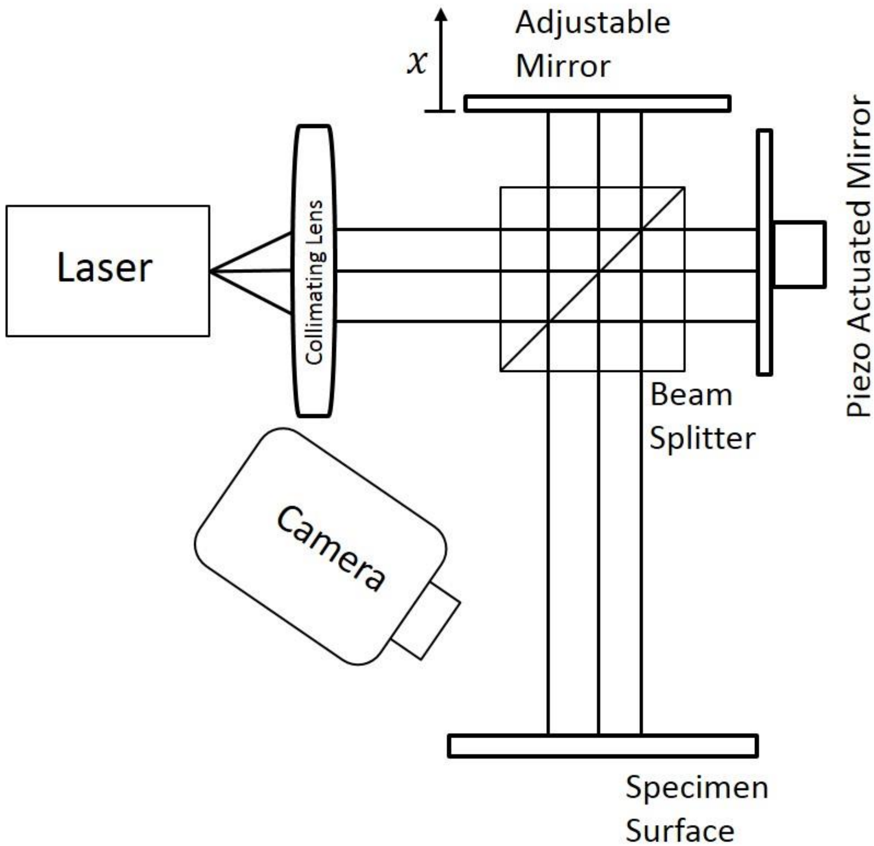

Figure 3.6 - Michelson interferometer arrangement

Graph 3.2 shows the variation of visibility with mirror distance. The coherence length is the full width half maximum at each peak which corresponds to roughly 1.5mm. This validates the coherence length measurements in Graph 3.1 and equation (26).

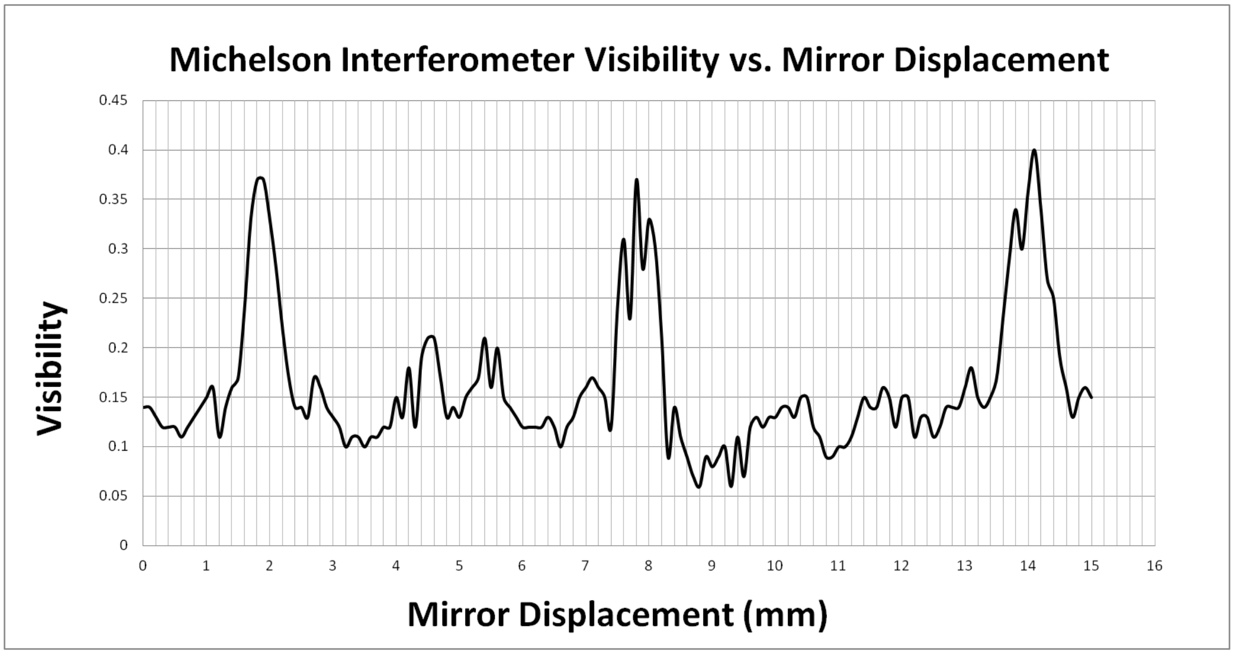

Graph 3.2 - Michelson interferometer visibility at varying mirror displacement

3.4 System Tuning

Although useful in characterizing the coherence length of a laser, coherence bands are undesirable for displacement measurements. Ideally, the full width of the image will have high visibility. To achieve this the laser must be set to operate within its ideal conditions and the optical path difference must be adjusted to so that all rays interfere within their coherent zones.

3.4.1 Laser Diode Stabilization

All lasers are composed of three fundamental components:

1. A gain medium – a material which emits photos when excited by an energy source
2. A pump source – an energy source used to stimulate the gain medium
3. Optical cavity – a filter which amplifies the photon emission and allows only certain wavelengths through.

The laser’s spectrum of operation is determined by the gain medium and the optical cavity. The gain medium emits photons over a narrow but continuous spectrum of wavelengths as seen in Figure 3.7a. The cavity filters the majority of the spectrum to a few allowed wavelengths as seen in Figure 3.7b. The resulting output is a central wavelength with a several equally spaced wavelengths of lower intensity as seen in Figure 3.7c.

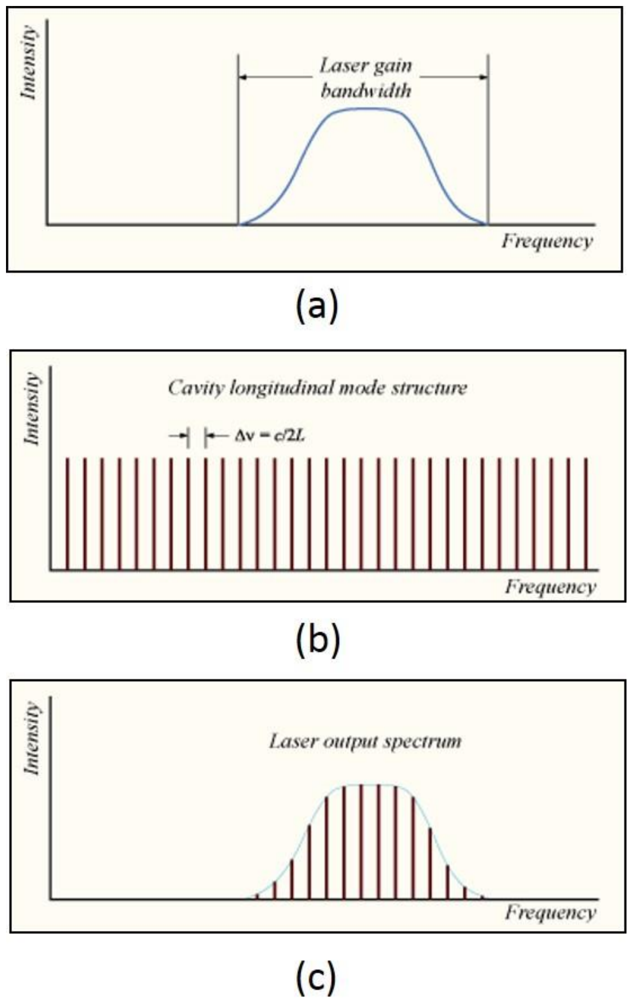

Figure 3.7 - a) Gain medium spectrum profile b) Optical cavity allowed frequencies c) Resulting laser diode emission, adapted form [31].

As the temperature or current drifts the gain profile shifts along the allowed wavelengths governing the dominant central wavelength outputted. If the current or temperature drifts such that the gain profile is in between two central wavelengths the laser source is in a state of "mode hopping" and the coherence length is significantly reduced [31]. Therefore it is important to adjust the laser diode such that it is in the optimal operating conditions and is at its greatest possible coherence length.

3.4.2 Geometrical Tuning

Even with optimal temperature and current tuning laser diodes have a coherence length of about 2-4 mm. To make effective use of a laser diode the tolerance of the interferometer arms need to be within the coherence length. An effective way of maintaining equal lengths for a diffraction grating interferometer is by collimating the laser beam. Figure 3.8 shows the arrangement of a diffraction grating interferometer with a collimated beam.

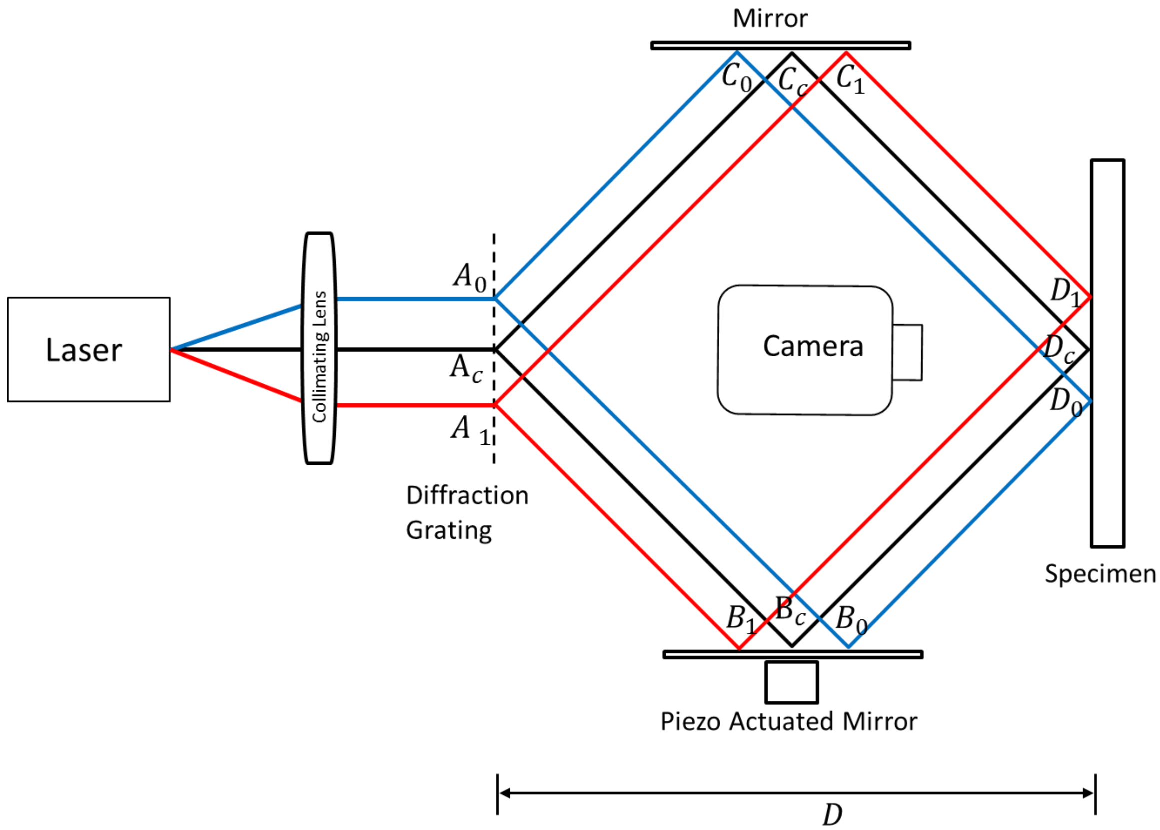

Figure 3.8 - Collimated diffraction grating interferometer

All path lengths along the width of the image are now equal in magnitude and can be adjusted to be within the coherence length. Mathematically:

$$
\begin{aligned}
\textit{central path length difference} &= \overline{(A_cB_c} + \overline{B_cD_c)} - \overline{(A_cC_c} + \overline{C_cD_c)} \\
\textit{path length difference for ray } 1 &= \overline{(A_1B_1} + \overline{B_1D_1)} - \overline{(A_1C_1} + \overline{C_1D_1)} \\
\textit{path length difference for ray } 0 &= \overline{(A_0B_0} + \overline{B_0D_0)} - \overline{(A_0C_0} + \overline{C_0D_0)} \\
&\geq l_c
\end{aligned}
$$

In practice, it is difficult to align the mirrors perfectly and even small deviation can misalign the ray paths. A practical and effective way of adjusting for small ray path misalignments is by angling the diffraction grating as seen in Figure 3.9. The angle of the diffraction grating, γ, causes ray paths to lengthen or shorten appropriately to correct for any mirror misalignment.

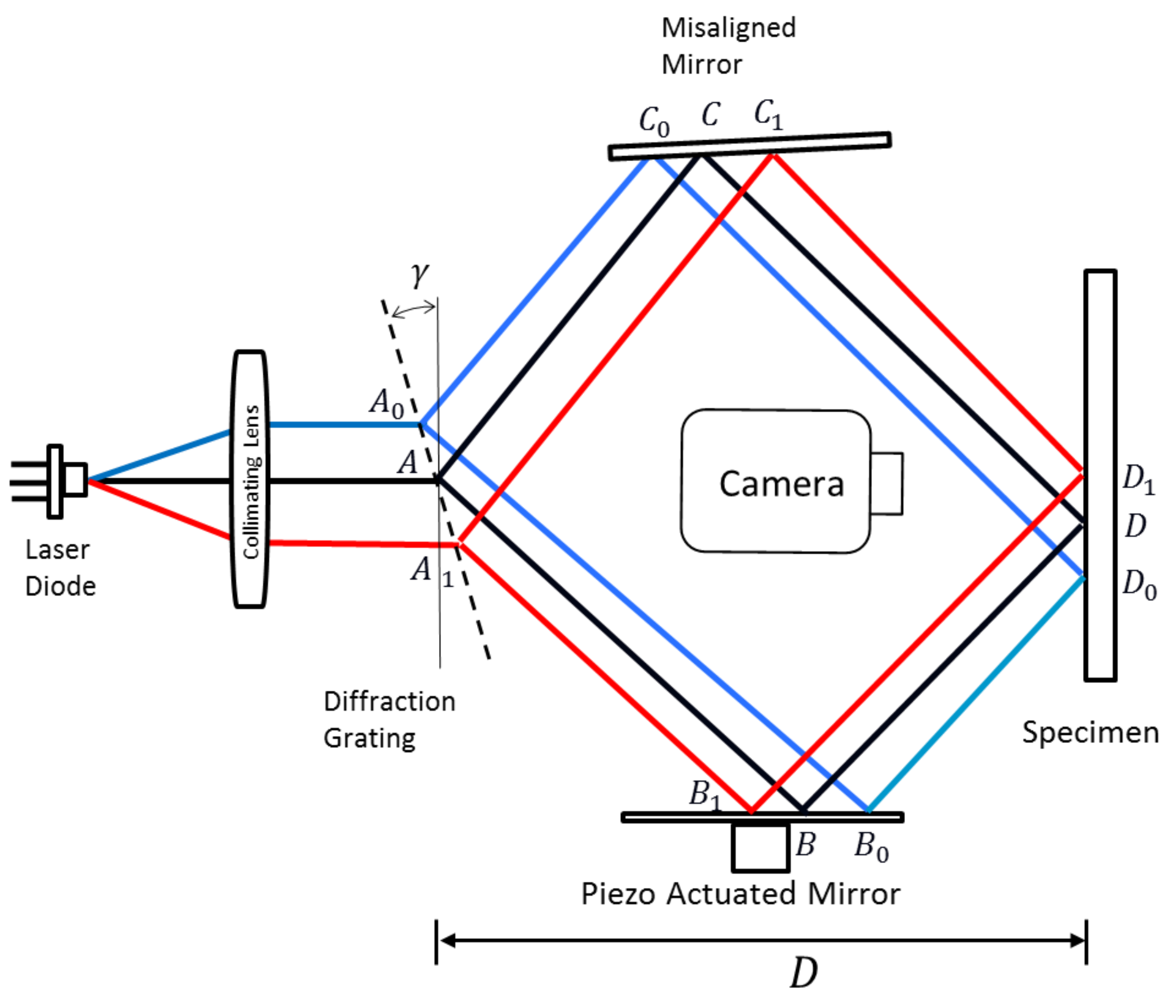

Figure 3.9 - Diffraction grating interferometer with angle adjustment

The relationship between the path length difference and the angle of the diffraction grating can be given by:

$$\delta = \frac{2\,\mathrm{D}\sin\theta\,(1 - \cos\theta)}{cos^3\theta}\sin\gamma \qquad (26)$$

where γ is the angle of the diffraction grating.

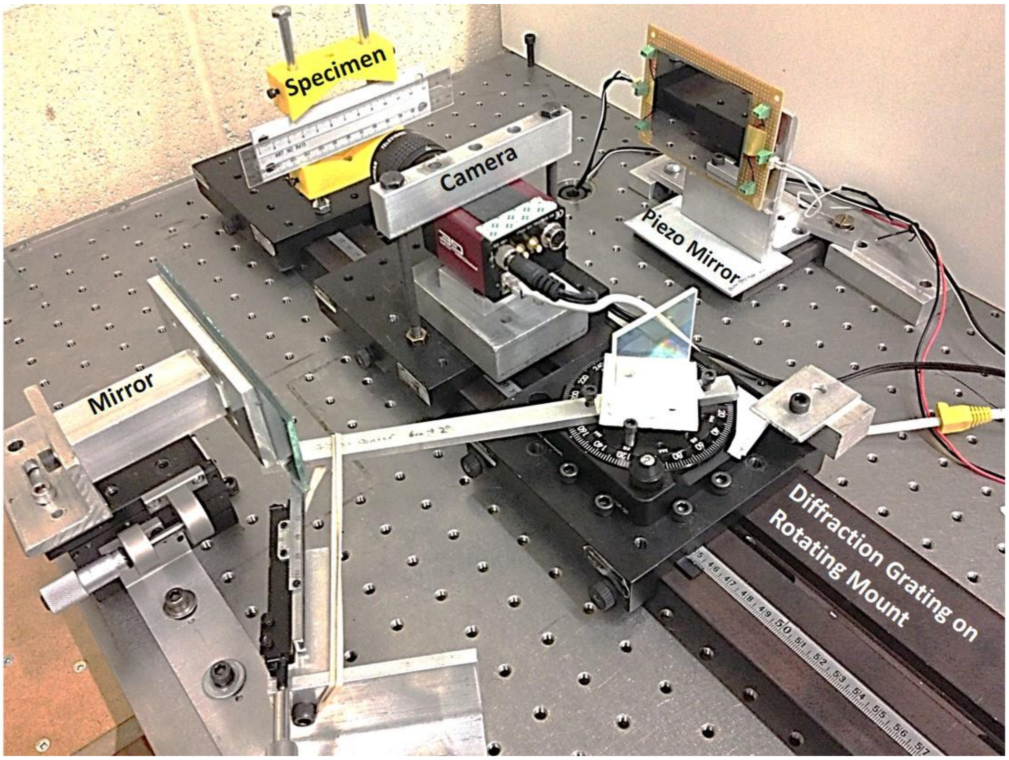

Figure 3.10 – Grading rotation experimental set-up

Using the experimental set-up in Figure 3.10 an experiment was conducted were the diffraction grating was rotated in 0.06° increments over 1.8° range and the average visibility was computed at each increment. Graph 3.3 shows the resulting change in average visibility with diffraction grating angle, γ.

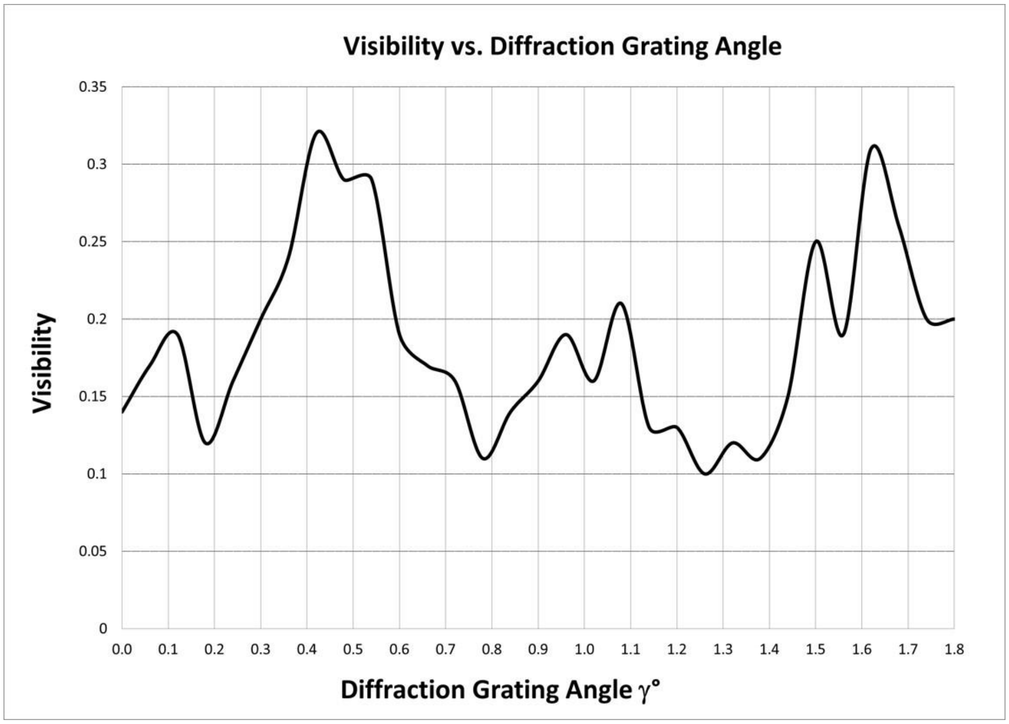

Graph 3.3 - Measurement visibility at varying diffraction angles

Graph 3.3 was generated using the following parameters:

Laser Diode: Mitsubishi ML520G54	Optical Geometry
λ = 638 nm	D = 279
l_c= 1.55mm	θ = 50°

Table 3.2 – Measurement parameters of grating rotation experiment

The full width half maximum of the peaks ranges over 0.25°. Substituting into equation (27) this results in a path length difference, δ, of 1.9mm, which is comparable to the 1.5mm coherence length of the laser diode. Figure 3.11 shows the resulting high visibility image possible with a geometrically tuned interferometer.

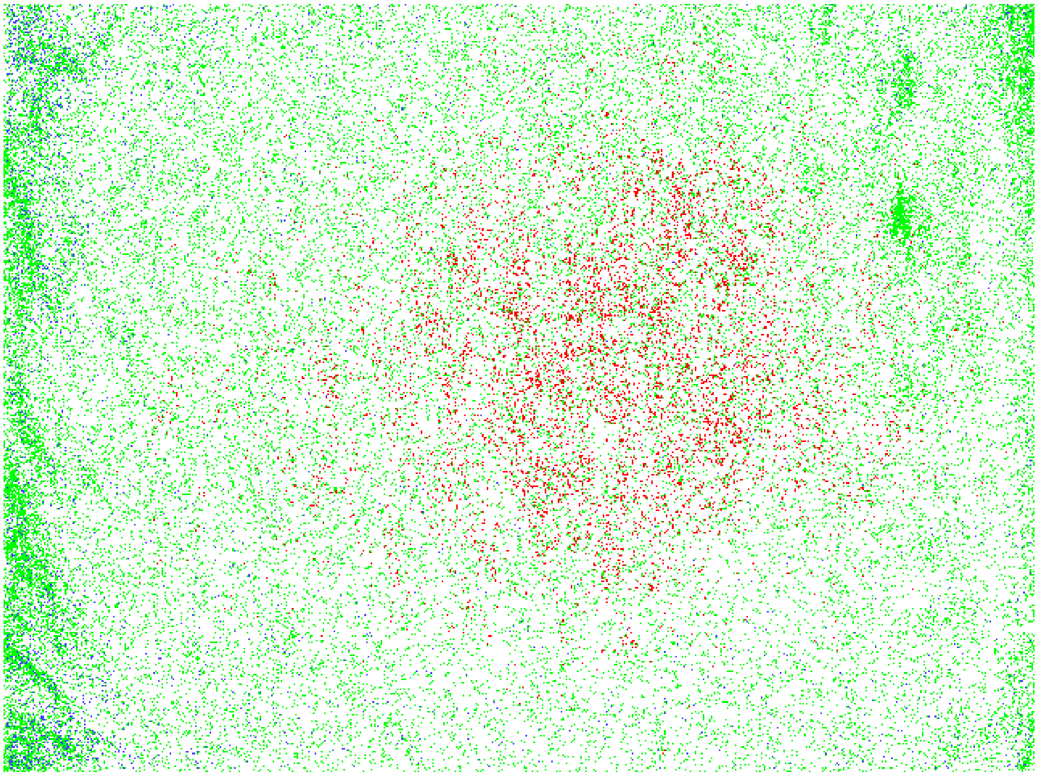

Figure 3.11 - Geometrically tuned interferometer providing visibility of 0.3 across full with of image. Red pixels are due to overexposure.

3.5 Conclusion

All interferometers are affected by the coherence length of the illumination source. The coherence length governs the ability of the interferometer to produce a detectable signal. To achieve reliable measurements, images with high visibility need to be acquired. The short coherence length of laser diodes makes them particularly challenging for interferometry, as the alignment of the optical path lengths needs to be maintained to within 2-4mm. An interferometer using a diffraction grating provides a practical means of maintaining the optical path lengths of the interferometer equal. Care must be taken to appropriately collimate the illumination beam such that the equal path length is maintained across the full width of the image. By slightly angling the diffraction grating small optical misalignments can be corrected. By controlling the optical geometry of the interferometer full control of the image visibility is achieved. For residual stress measurements the interferometer is tuned to achieve the highest possible visibility. This control of visibility has proven useful in characterizing the coherence length of laser diodes. Due to the simplicity and robustness of the optical components and their arrangement a diffraction grating interferometers lends itself to being integrated into a portable device.

Chapter 4: Compact ESPI Device for Residual Stress Measurements

Current ESPI systems for residual stress measurement are bulky and require tightly controlled laboratory conditions to provide reliable measurements. Such systems are impractical for measuring residual stress on large or immovable structures in the field. Unaccounted stresses in such structures can have catastrophic effects and periodic monitoring of their internal loads is vital. Therefore a practical ESPI system capable of measuring residual stress in the field is required. Such a system needs to be:

1. Compact and portable such that it can be conveniently transported to site and mounted at desired location within the structure of interest.
2. Robust and rugged so that it can withstand environmental fluctuations and mount to a variety of structures.
3. Capable of providing highly reliable residual stress measurements without a directional bias as described in Section 2.3.

Such a device was designed and constructed, implementing the benefits of compact laser diodes and the novel geometrical arrangement and system tuning described in Chapter 3. This chapter outlines the various modules which comprise the device.

4.1 Optical Arrangement

As described in Section 3.4.1.1, controlling the optical geometry is the most important factor to consider in achieving high visibility measurements using a laser diode. Therefore the beam path of the portable interferometer was designed first and the rest of the components were fit to accommodate it. The final beam geometry can be seen in Figure 4.1.

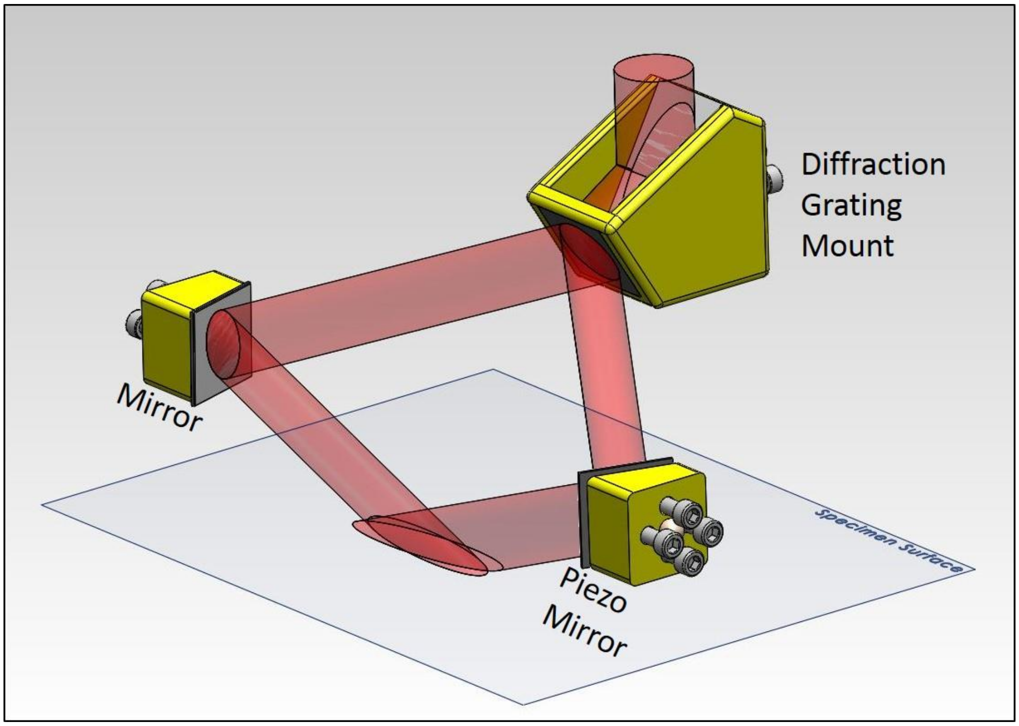

Figure 4.1 - Beam geometry illuminating the specimen surface along axis 1

The beam travels vertically downward and into the Diffraction Grating Mount which redirects and splits the beam appropriately. Each of the two split beams is directed onto the surface of the specimen using two mirrors, one of which is piezo actuated. This three-dimensional beam path was chosen because:

1. The split beams have equal path lengths.
2. It provides short beam paths which can more easily be controlled to interfere in their coherent zone.

3. The optical components do not interfere with the viewing field of the camera.
4. The optical geometry can be orthogonally duplicated to achieve a second axis of sensitivity as can be seen in Figure 4.2.

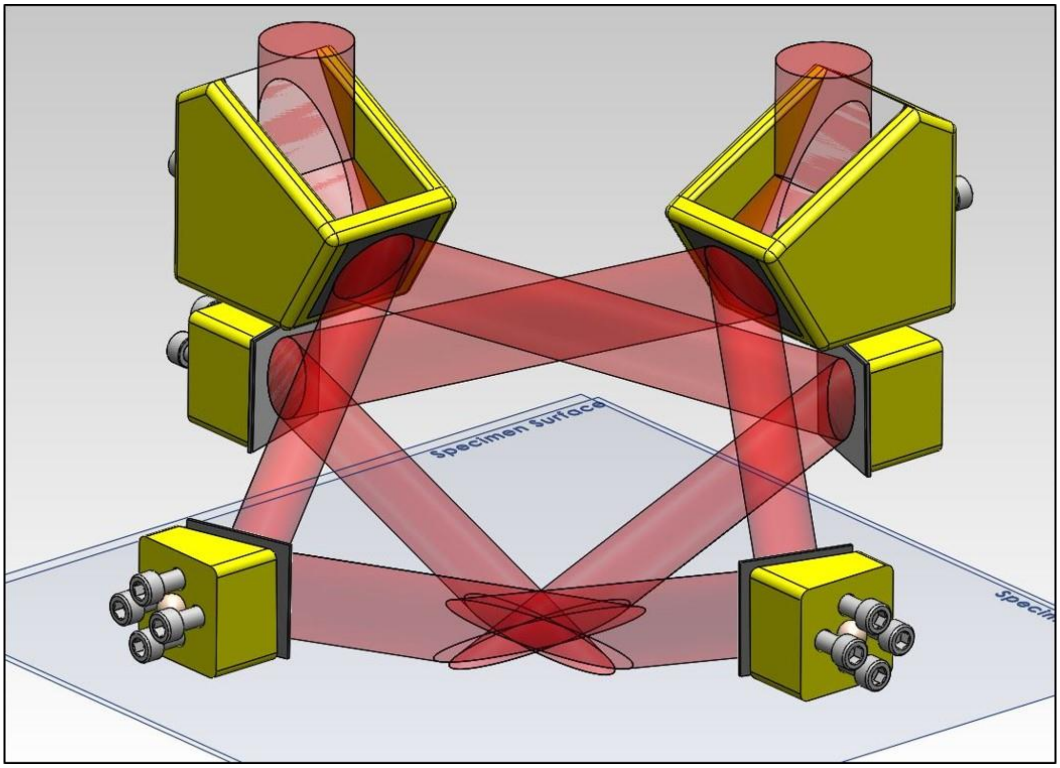

Figure 4.2 - Orthogonal beam geometry illuminating along axis 2

Figure 4.3 shows the integration of the optical geometry into the portable interferometer. The optical components are mounted onto the legs of the interferometer where they are environmentally shielded with panes of glass. The angle of each optical component can be adjusted with a four screw fixture. A camera is mounted pointing downwards to view the interference pattern on the surface of the specimen.

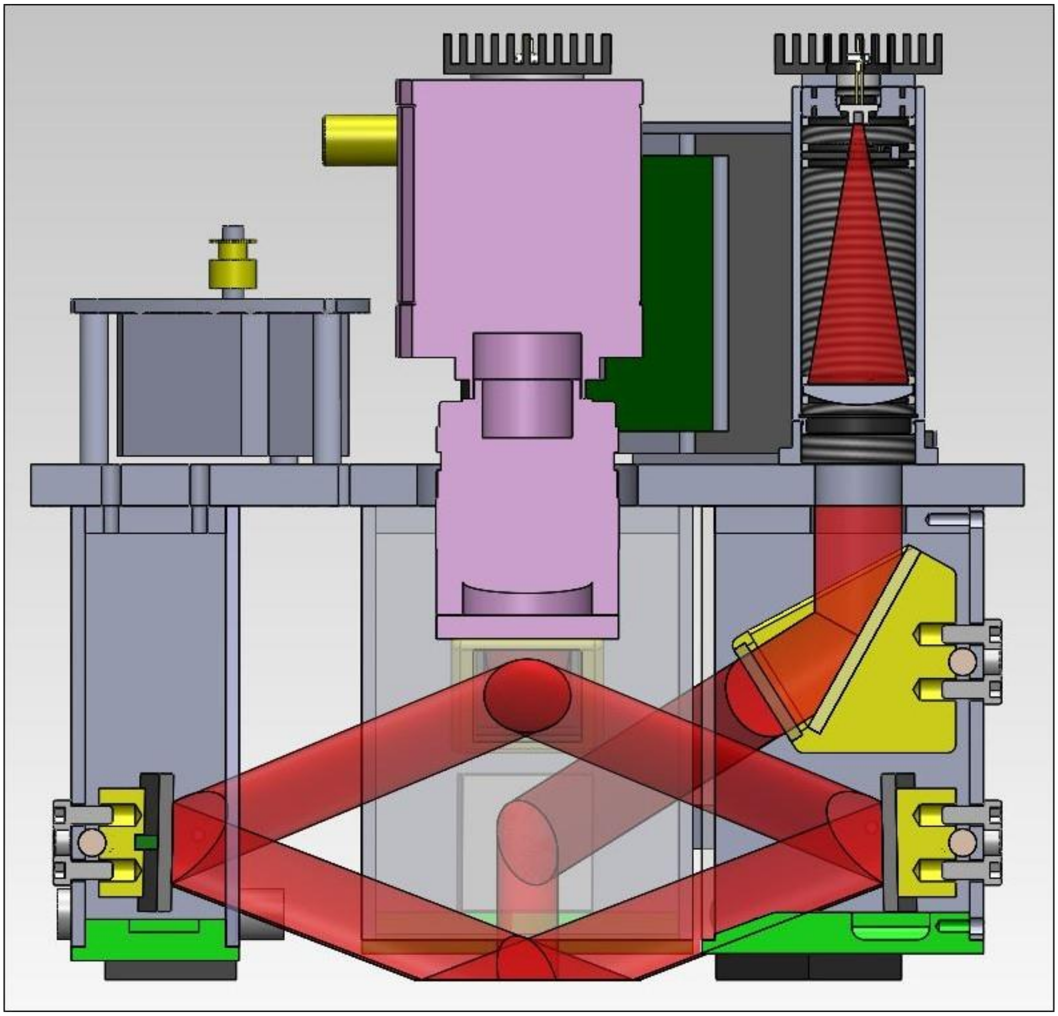

Figure 4.3 - Cross section of portable ESPI device

The arrangement of this interferometer is unique in that it gives complete in-plane displacement sensitivity. As described in Section 2.3.2 typical speckle pattern interferometers rely on the faint effects of poisson's ratio to detect displacements orthogonal to the axis of measurement. With a dual axis system residual stress displacements are measured directly, providing more accurate results [28] [35].

4.1.1 Laser Assembly

The laser diode used for the portable interferometer is a Hitachi HL654MG, with a wavelength of 660 nm and output power of 130 mW. At optimal temperature and current conditions the coherence length of this laser diode was measured to be 2.0 mm. Figure 4.4 shows the laser assembly.

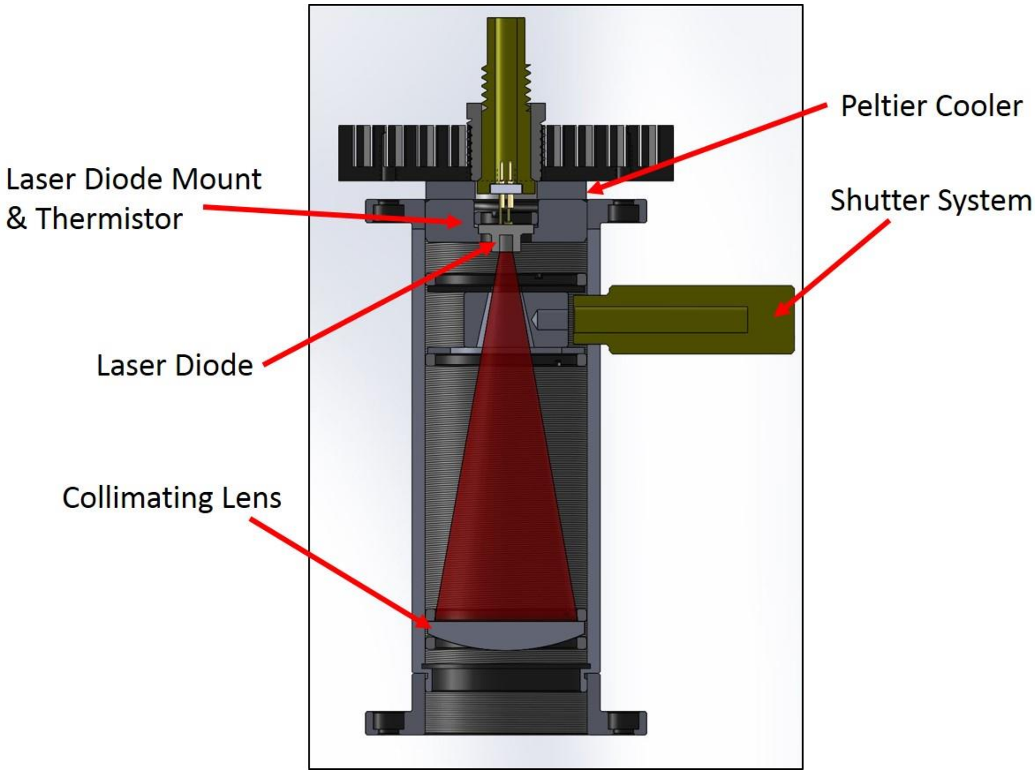

Figure 4.4 - Cross section of laser assembly

A Wavelength Electronics© LDTC0520 controller is used to control the current and temperature of the laser diode. The controller relies on a thermistor sensor and thermoelectric cooler to maintain the temperature of the diode at an optimal condition. A collimating lens is used to control the shape of the beam and a shutter system is used to synchronize each axis of measurement.

4.1.2 Camera Assembly

The camera used is a Prosilica EC750 with a 752 x 480 pixel resolution and pixel area, p, of 6.0μm x 6.0μm. A 25mm Cosmicar lens is used to image the specimen surface. The lens F-number is adjusted to 11 so as to view only one speckle per pixel. The lens is mounted 78mm from the surface providing a magnification, M = 0.25. Using equation (8) each pixel corresponds to a 24μm x 24μm area on the surface of the specimen.

4.2 Drilling Mechanism

A custom drilling mechanism was built to achieve cuts at incremental depths. The drilling mechanism electrically senses the surface of the specimen and is capable of advancing with a precision of 0.05mm increments. An Astro NSK E250 medical drill running at 22,000 rpm with a 3/32" (2.35 mm) flat end milling bit is used to make the incremental cuts.

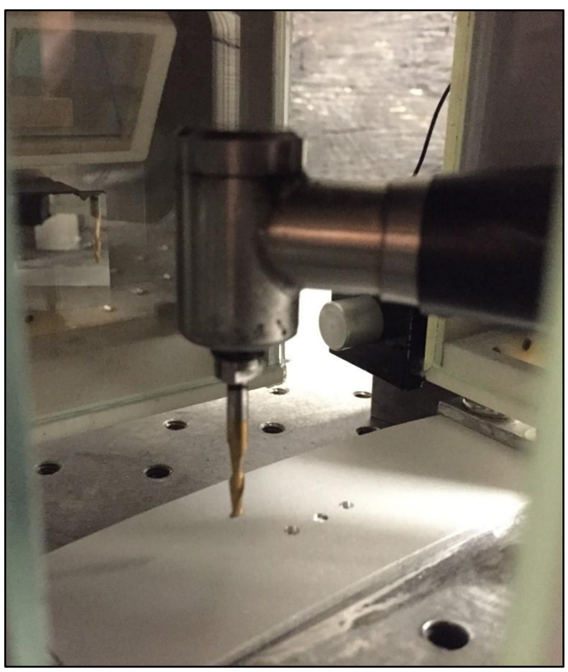

Figure 4.5 - Close up of mill head with 3/32" milling cutter and several holes of varying depths

The drilling mechanism also moves the drill left and right out of the camera view and illumination beam.

4.3 Chassis and Magnetic Feet

A 3/8" thick circular chassis, diameter = 10", aligns and holds all of the components in place. The rigidity of the chassis minimizes any relative movements which may disturb the sensitive ESPI displacement measurements. Three magnetic feet rigidly connect the device to the specimen surface.

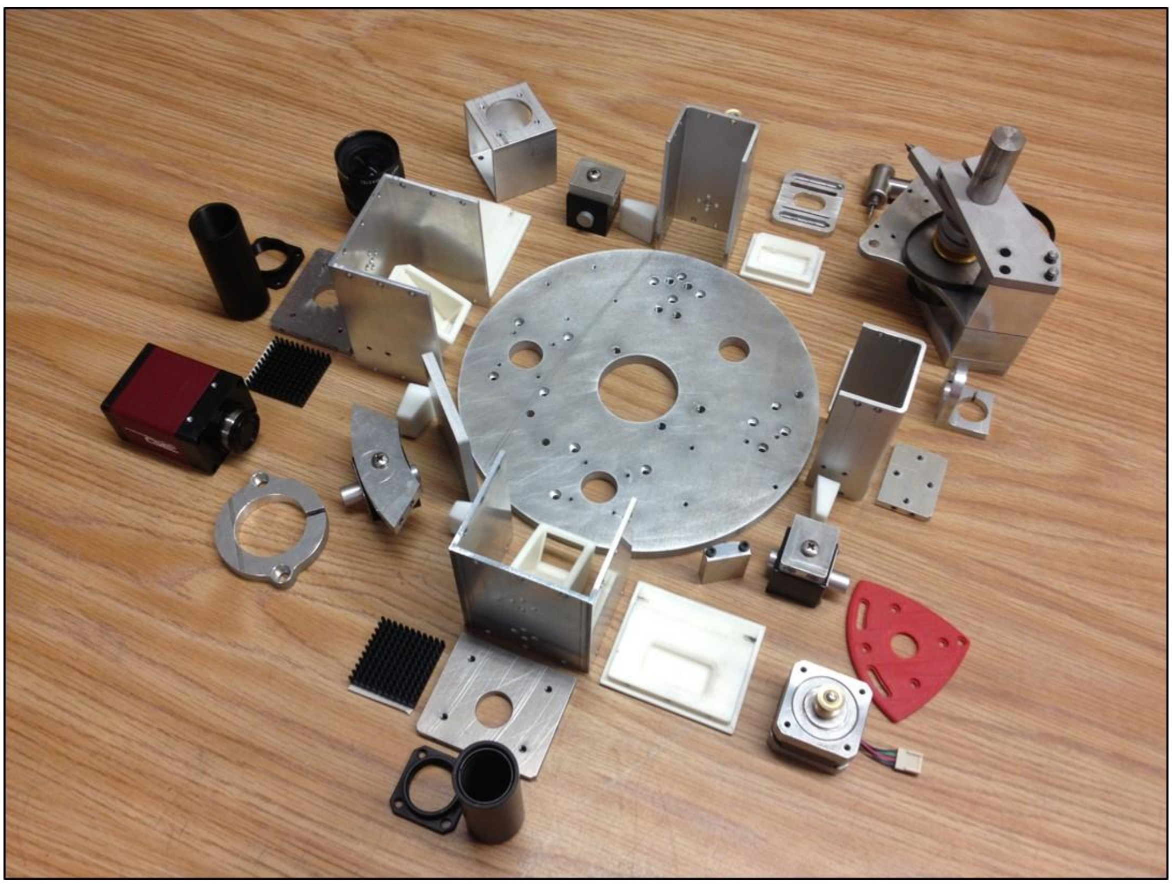

Figure 4.6 - Circular chassis disassembled from all components

4.4 Control Box and Cabling

A control box was built to distribute power and trigger the various components of the instrument. A custom 25 pin cable connects the control box to the instrument and a USB cable connects the computer to the control box.

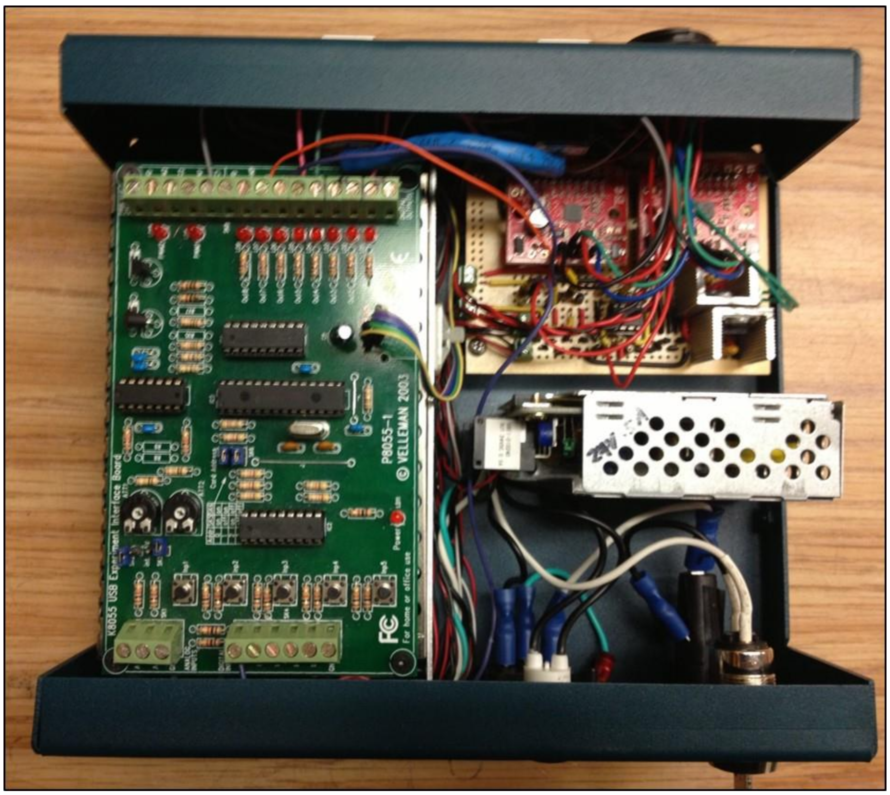

Figure 4.7 - Plan view of control box

4.5 Software and Integration

A custom software called Blazer was developed to drive the portable interferometer and compute the residual stress measurements. The software synchronizes the hole drilling actuation with the ESPI sequencing described in Section 2.2.5. The software also unwraps the fringe patterns and computes the residual stress components as described in Section 2.1.

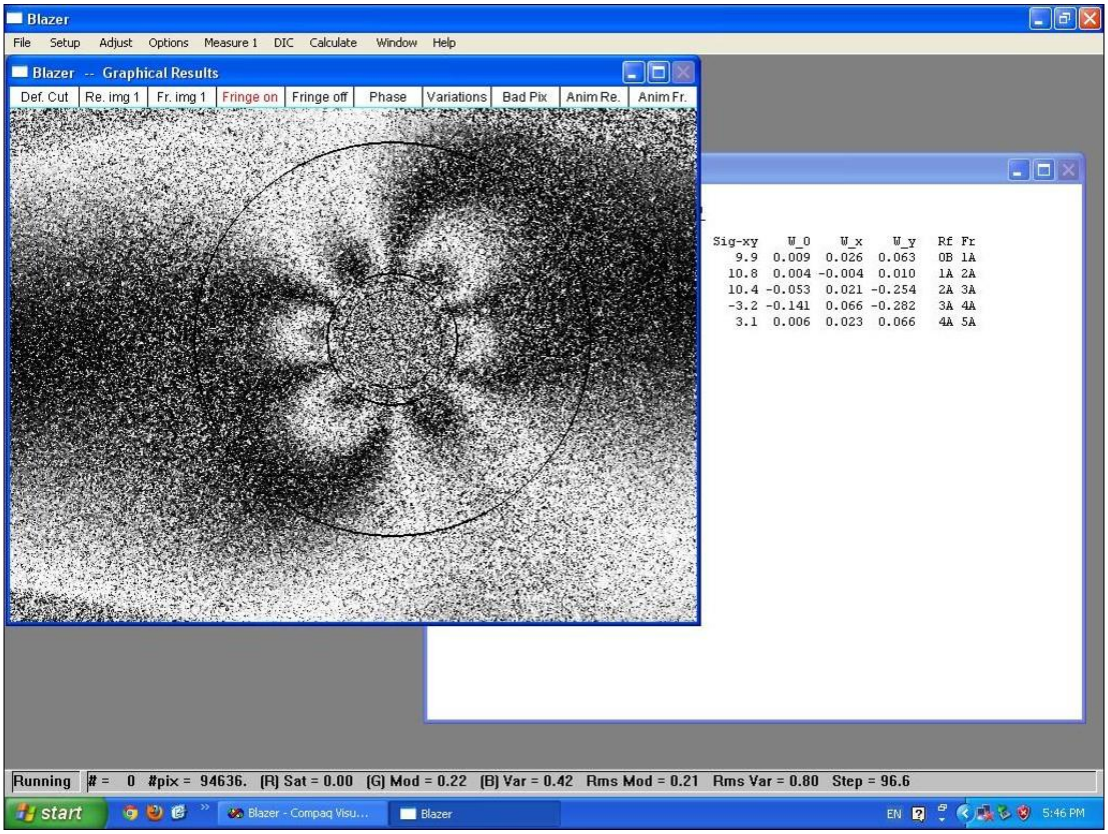

Figure 4.8 - Blazer displaying a raw fringe pattern

The software computes the residual stress components using measurements from Axis 1, Axis 2 and the combination of both Axes.

4.6 Compact ESPI Device with Dual-Axis Sensitivity

This chapter describes the various modules and systems which compose the portable interferometer. Figure 4.8 (a), (b), (c) and (d) show the integration of these modules.

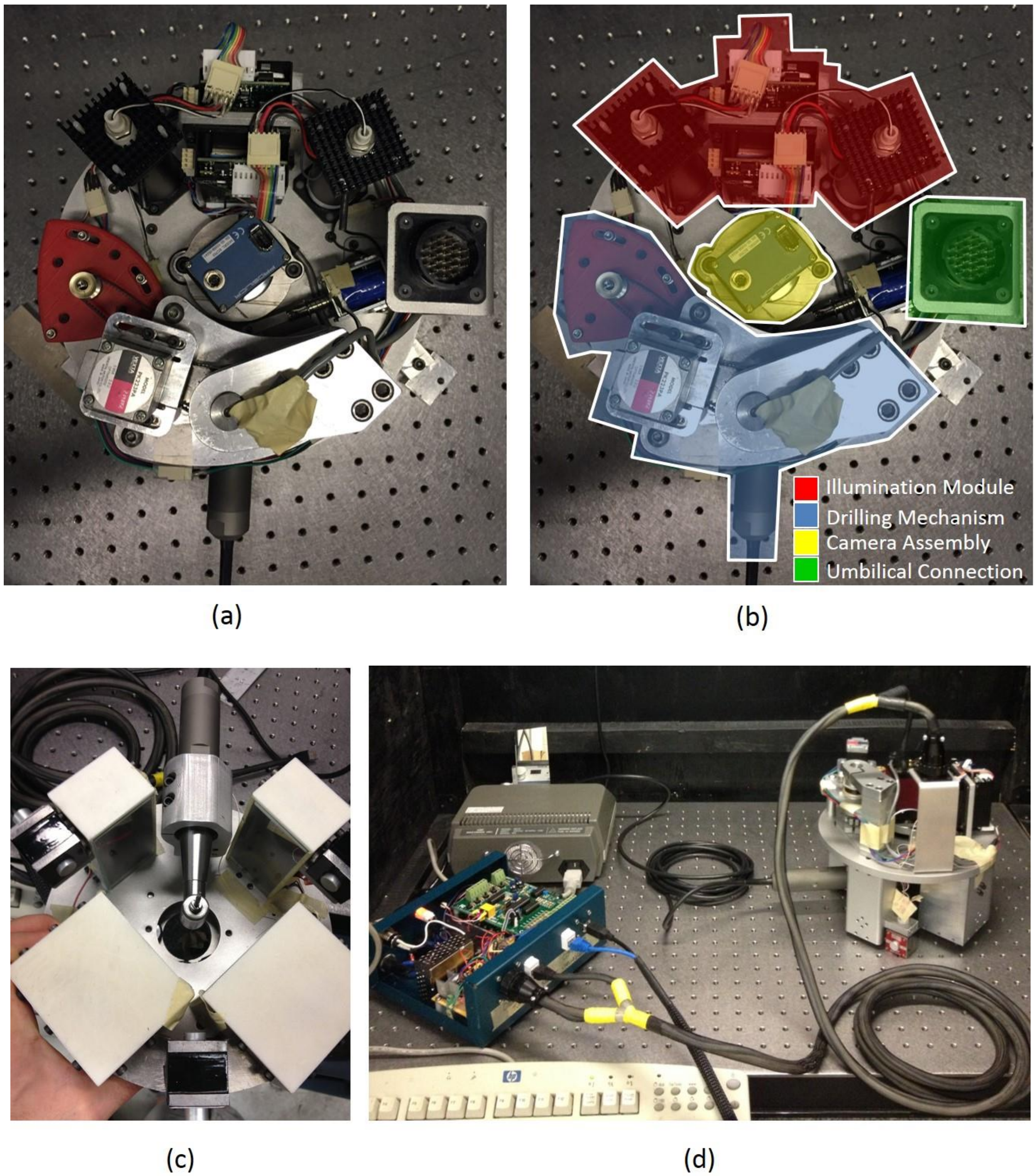

Figure 4.9 - a) Top view of the Compact ESPI Device b) Top view of the Compact ESPI Device with highlighted modules c) Underside of device d) Final assembly of device connected to control box and drill driver

The novelty of this compact and portable device is the practical implementation of laser diodes to provide residual stress measurements of high quality and reliability. This is achieved by tuning the optical system as described in Section 3.4. A further novelty of this device is the dual axis displacement sensitivity. Previous studies have shown the benefits of dual axis interferometry for residual stress measurement [27] [28]. This work incorporates these benefits into a portable package. In the field the orientation of the principal stresses within a structure are rarely known, especially when unaccounted internal loads exist. Therefore aligning a measurement instrument with a single axis of sensitivity to detect the highest stresses in a structure is difficult and often results in loss of precision and accuracy [12], [29]. It is shown that a system with dual axis measurement sensitivity does not require prior knowledge of the stress distribution in a structure to provide measurements of high accuracy and precision.

Chapter 5: Measurement Capabilities

The objective of this experimentation is to determine the measurement accuracy and precision of the compact ESPI device. Measurements were conducted on a calibrated bend specimen and the results compared to the theoretical values. Ideally, a calibrated specimen with residual plane stress in two orthogonal directions, as shown in Figure 2.12, would be used to highlight the capabilities of dual axis measurements. Practically, creating such a specimen for hole-drilling is challenging, therefore a bend specimen with plane stress in one direction is measured at varying orientations of the instrument.

Experimentation consisted of Experiment 1 where the orientation of measurement relative to the principal stress direction was varied to investigate the effect on accuracy and Experiment 2 where a series of measurements under the same conditions were made to identify the precision of the instrument.

5.1 Bend Specimen

All formed metal contains residual stress. As explained in Section 1.1.1, this is due to the manufacturing processes involves in forming the metal. The distribution of these residual stresses is irregular across the surface and depth of the material. For a specimen sample to be useful it needs to be relieved of these stresses and a calibrated residual stress applied to it.

Practical challenges occur in creating a specimen of pure plane stress where calibrated residual stresses are to be applied in two orthogonal directions while maintaining structural rigidity so that a hole can be drilled without causing rigid body movements. Therefore a bend specimen with a calibrated stress in one direction is used and the direction of measurement is changed to simulate stress in multiple directions.

The preparation of the bend specimen begins by cutting appropriately sized blanks out of a 6061 aluminum plate. The blanks are stress relieved by skimming the surface layers that contain the compressive residual stresses explained in Section 1.1. The specimens are clamped in a bending jig that elastically stresses them and rigidly constrains them for hole drilling.

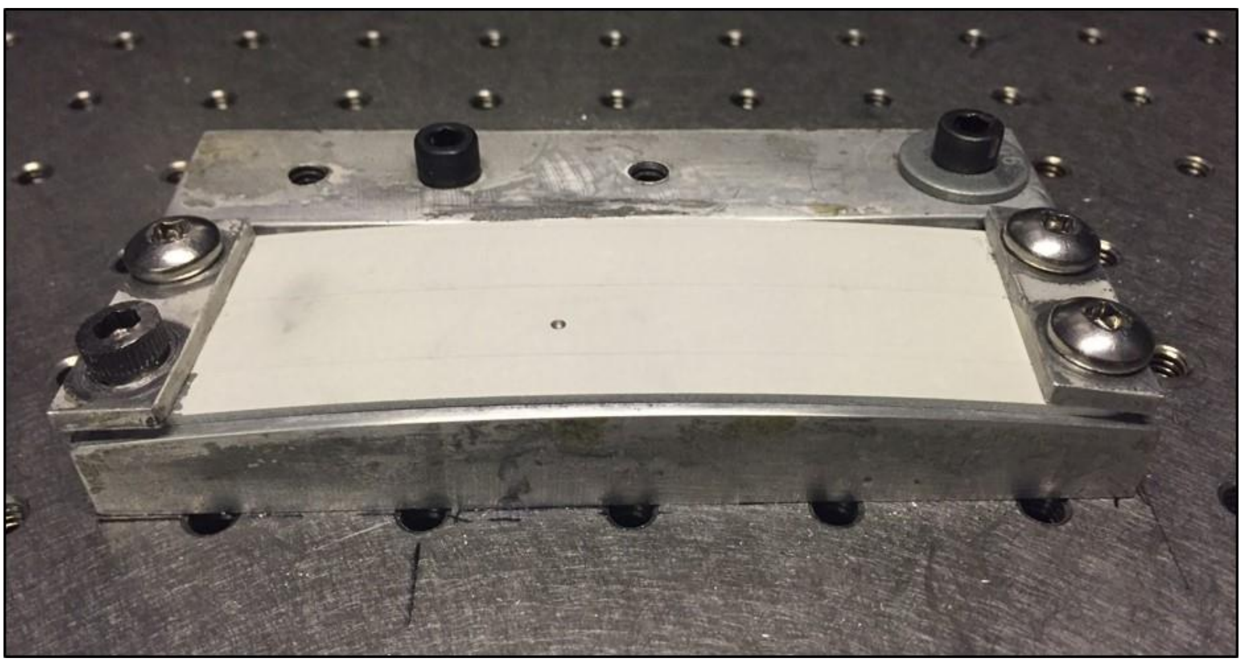

Figure 5.1 - Bending jig with a loaded specimen

Figure 5.2 illustrates the bend geometry of the specimen and the direction of the maximum principal stress. Given the bend radius, R, the thickness of the specimen, t, and the depth of cut, z, the stress along the maximum principal direction (X axis) can be computed [36]:

$$\sigma_x = \frac{E\,(t - z)}{2R} \tag{27}$$

For aluminum 6061, the elastic modulus, E, is 7.1 GPa [37].

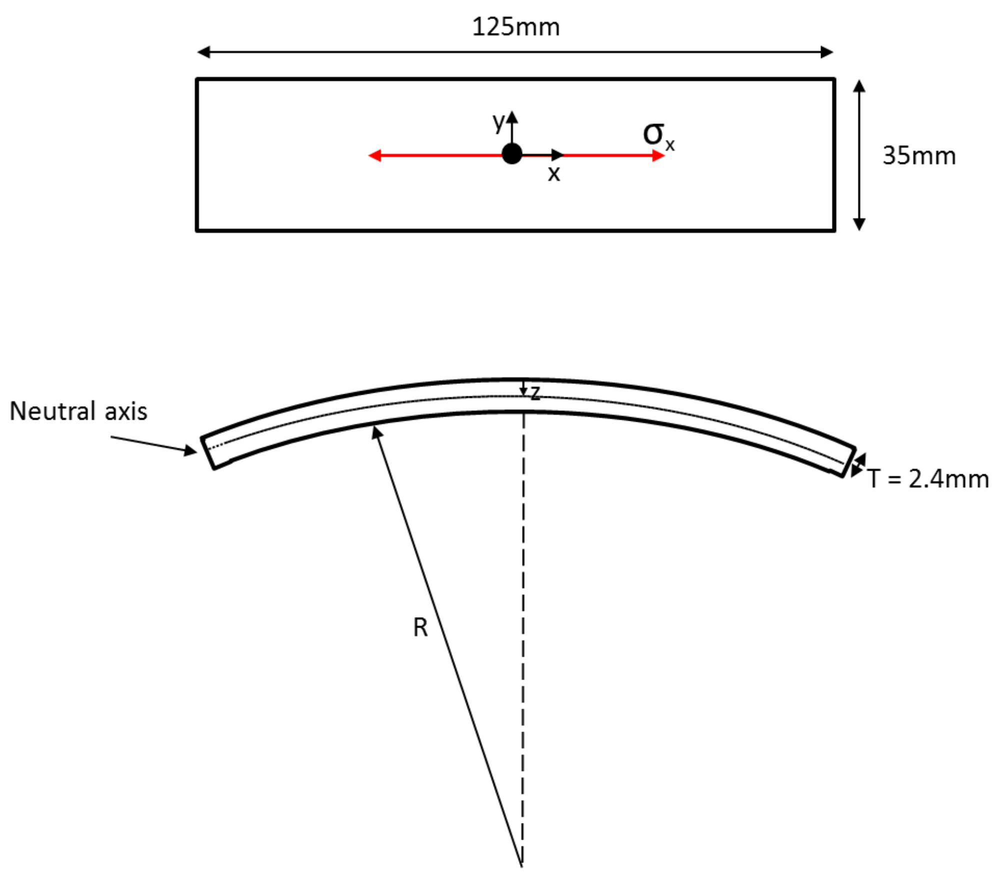

Figure 5.2 - Bend specimen geometry

5.2 Measurement Accuracy

Experiment 1 was conducted to determine the accuracy of each axis at varying measurement orientations relative to the maximum principal stress direction. Figure 5.3a-c shows the measurement orientations of each test. All three tests were conducted on the same 2.4mm thick specimen using a Ø1/16" milling bit. Two hole measurements were made at each orientation and the results averaged.

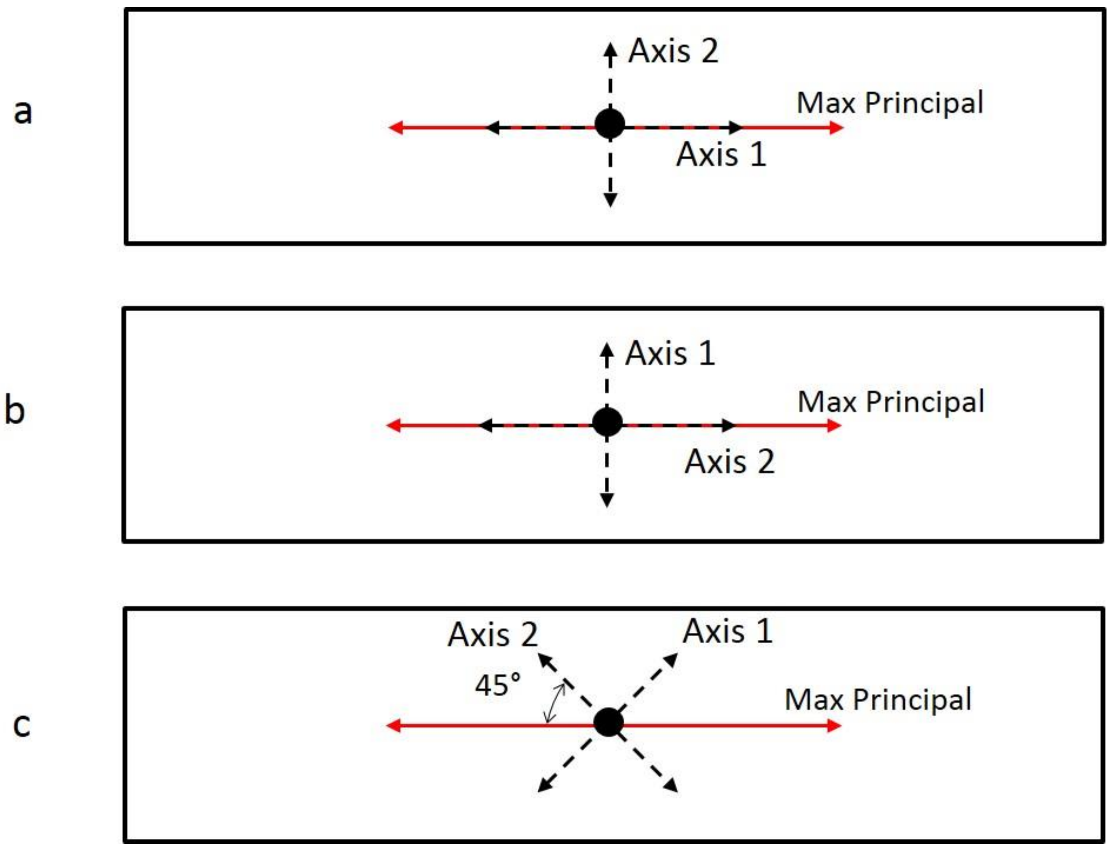

Figure 5.3 – Orientation of measurement for preliminary experimentation

a) Orientation 1 - Axis 1 along principal direction

b) Orientation 2 - Axis 2 along principal direction

c) Orientation 3 - Axis 1 and 2 at 45° to principal direction

5.2.1 Axis 1 Aligned with Maximum Principal Stress

At Orientation 1 shown in Figure 5.3a Axis 1 was aligned along the maximum principal stress and Axis 2 perpendicular to it. Graph 5.1 compares the measured stress profile from Axis 1, Axis 2 and the dual axis computation. All measurements follow the expected linearly decreasing trend computed using equation 27.

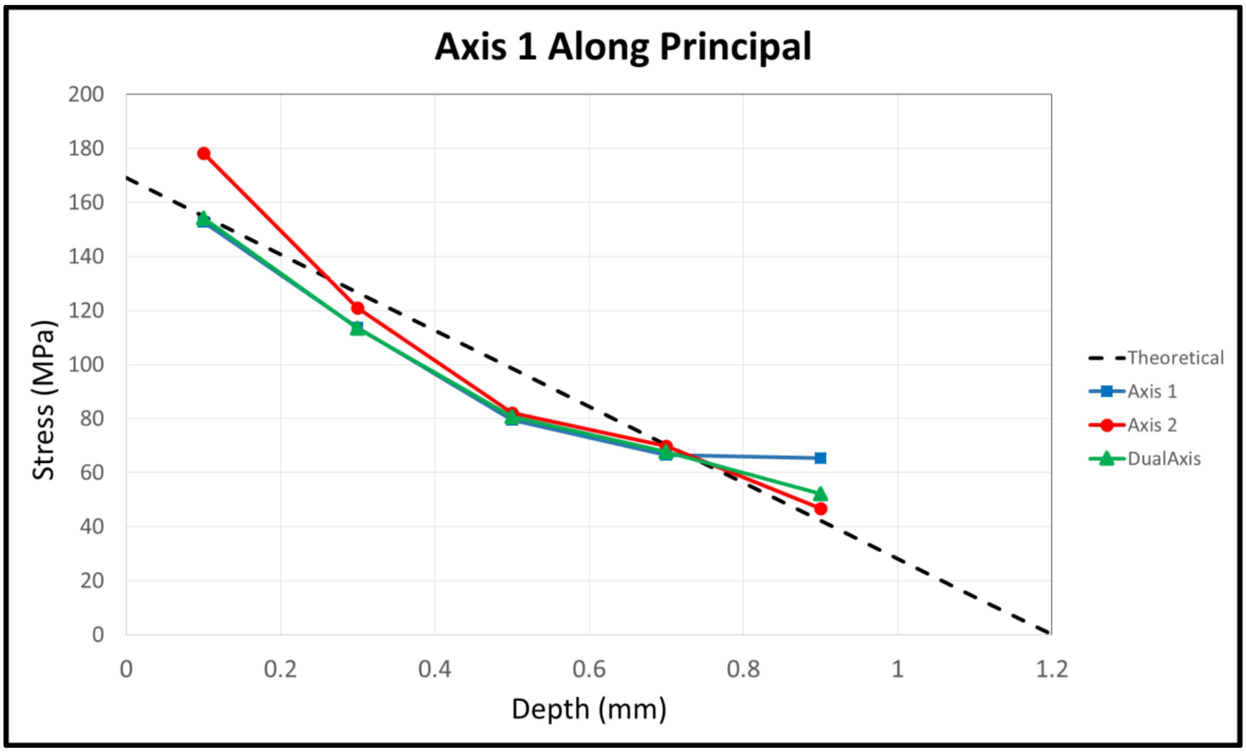

Graph 5.1 - Measured stress profiles at Orientation 1

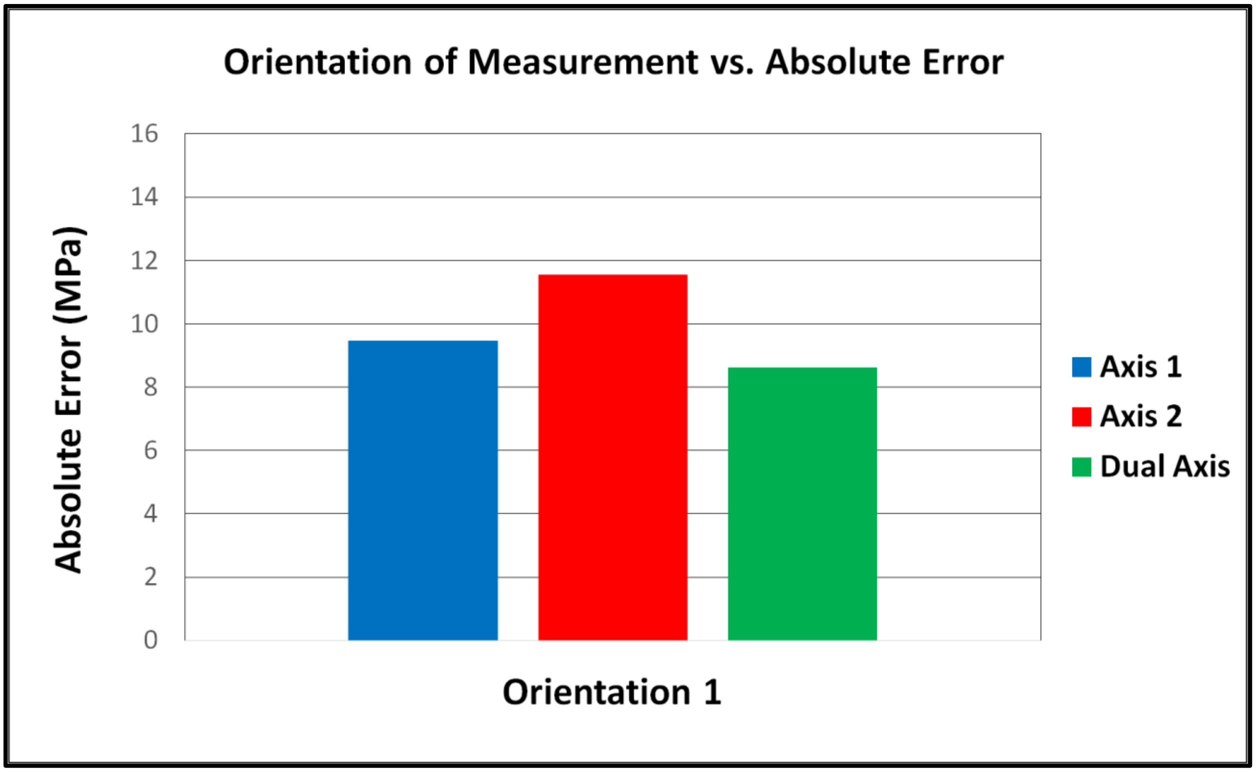

Graph 5.2 - Absolute error of each axis at Orientation 1

At Orientation 1 the measurements from Axis 1 are more accurate than the measurements from Axis 2. This occurs because, Axis 1 measures the displacement caused by the maximum principal stress directly whereas Axis 2 relies on the small contributions from Poisson's Ratio, as explained in Section 2.3.1. The accuracy of the dual axis computation closely matched that of Axis 1 because the least square computation favors the large displacement values measured with Axis 1. The accuracy of the dual axis computation will always be comparable to the more accurate axis.

5.2.2 Axis 2 Aligned with Maximum Principal Stress

A second test was conducted where Axis 2 was aligned with the maximum principal stress and Axis 1 perpendicular to it, as shown in Orientation 2 of Figure 5.3b. Graph 5.3 shows the resulting stress measurements from each axis. As in the previous arrangement all measurements followed the expected linearly decreasing trend.

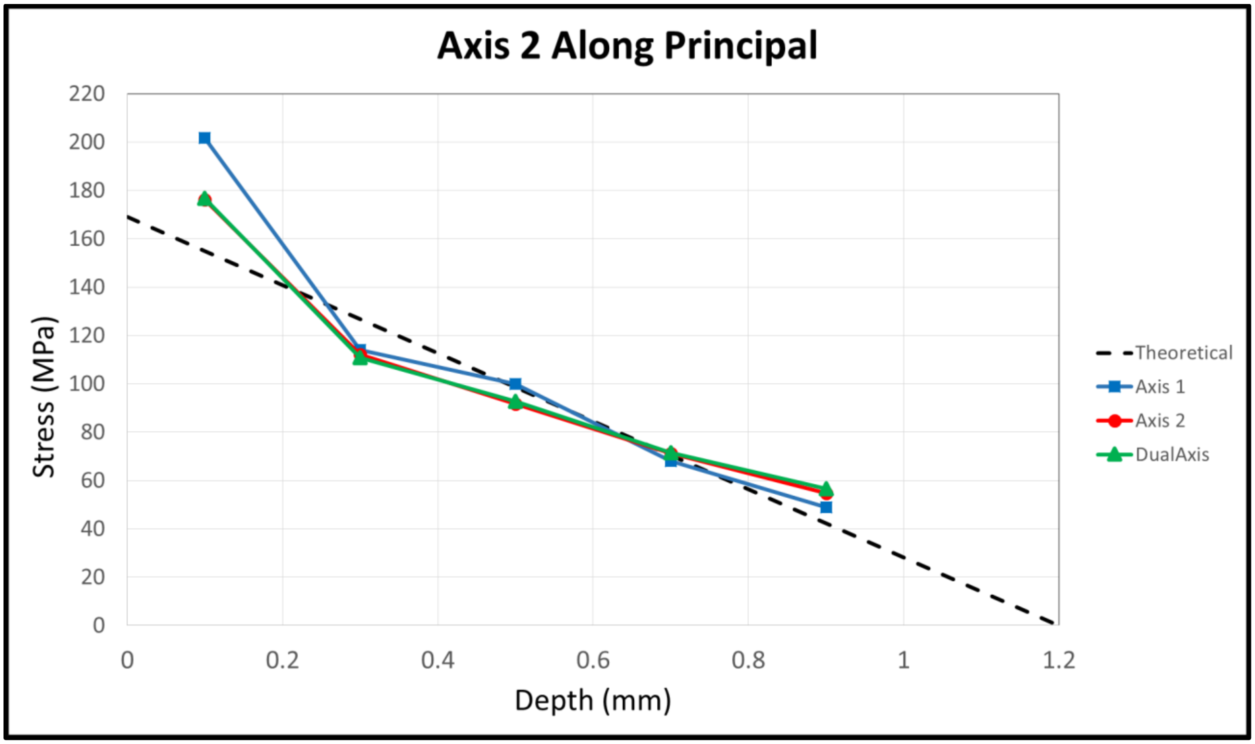

Graph 5.3 - Measurements stress profile at Orientation 2

Graph 5.4 compares the absolute errors of each axis at Orientation 1 and 2. In each case, the measurement in the on-axis direction is more accurate than in the off-axis direction. In addition, the dual axis measurement is always better than the off-axis measurement, and often better than the on-axis measurement.

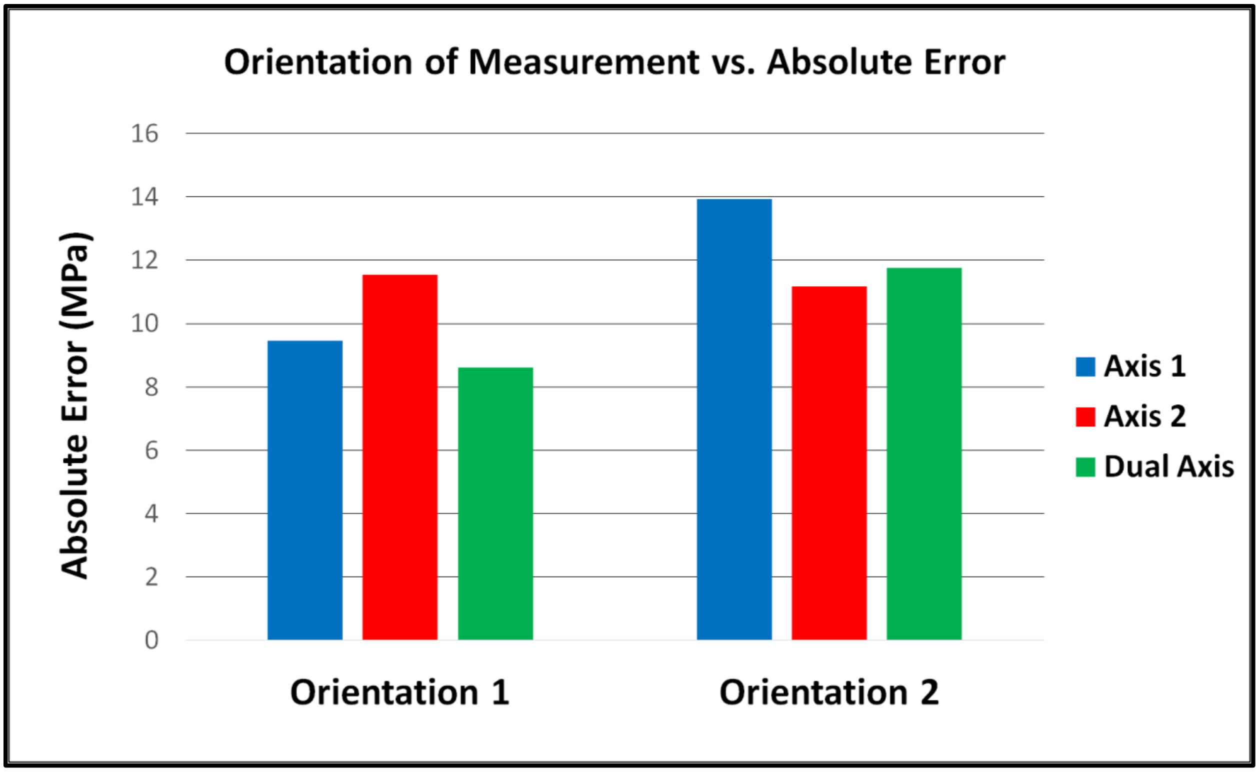

Graph 5.4 - Absolute error of each axis at Orientation 1 and 2

The results from the first and second tests show that the measurement orientation governs the overall accuracy. Furthermore, the accuracy of the dual axis computation always follows the most accurate measurement axis. Imagine a dual axis interferometer whose axes of measurement are aligned with the principal stresses. Each axis of measurement will yield accurate results for the stress it is aligned with, but moderate results for the stress it is perpendicular to. The dual axis computation will leverage the accurate results from each measurement axis to provide an accurate result for both principal stresses.

In the field, the orientation of the principal stresses within a structure are rarely ever known, especially when unaccounted internal loads are present. Therefore, relying on a specific alignment of the interferometer to achieve accurate results is impractical. In practice the axes of measurement will be orientated at some angle to the principal stresses. In the worst case this angle will be 45°, where both axes are equally misaligned with the principal stresses,.

5.2.3 Axis 1 and 2 Aligned at 45° to Principal Stress

To simulate an in-field measurement, a third test was conducted where Axes 1 and 2 where aligned at 45° to the maximum principal stress, as shown in Orientation 3 of Figure 5.3c. At this orientation both axes have equal measurement sensitivity. Graph 5.5 shows the resulting stress measurements from each axis. As in the previous arrangements all measurements followed the expected linearly decreasing trend.

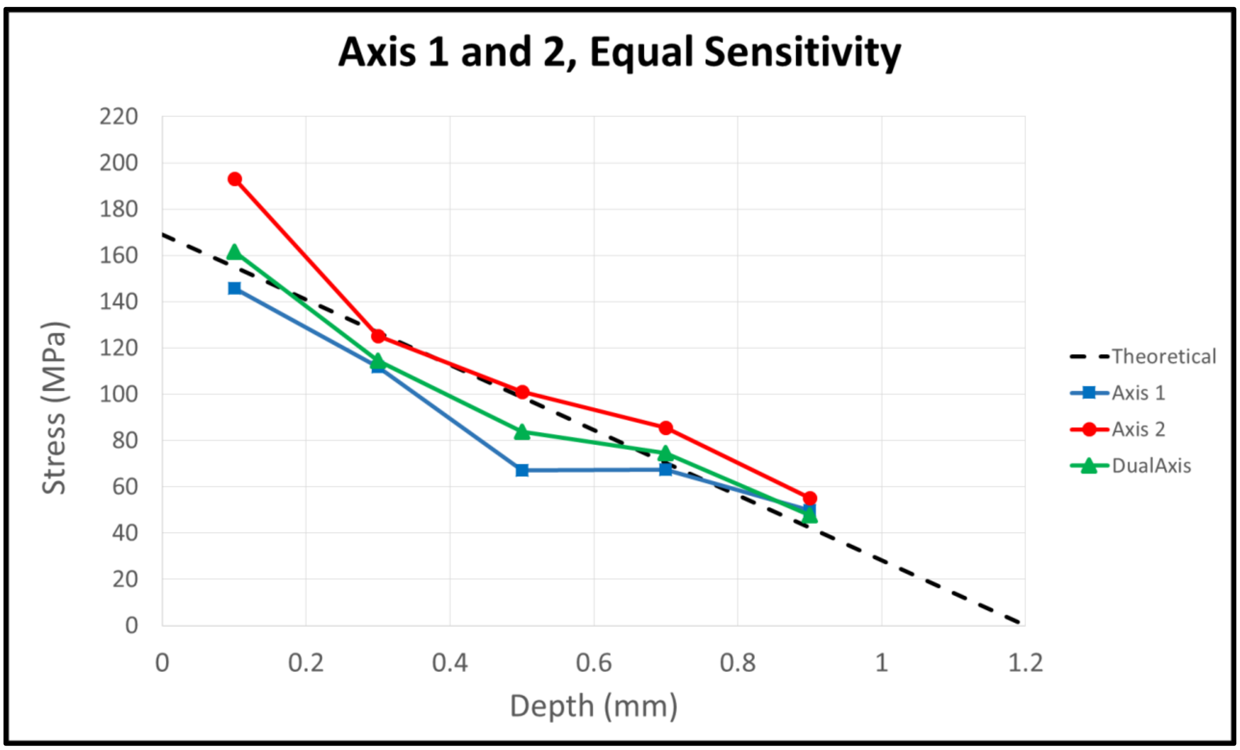

Graph 5.5 – Measurement stress profiles at Orientation 3

Graph 5.6 compares the absolute errors of each axis at Orientation 1, 2 and 3. It is evident that at Orientation 3 both Axis 1 and 2 have approximately equal accuracy. The accuracy of the dual axis computation is significantly better than both Axis 1 and 2. This result is misleading as the overall accuracy of the dual axis computation relies on the sensitivity of each axis. Since both axes have the same sensitivity to the maximum principal stress the dual axis accuracy should be similar to each of the two axes. Upon further investigation it is noticed that stress profile measured with Axis 1 is slightly below the theoretical profile whereas the stress profile measured with Axis 2 is slightly above it. The dual axis computation causes these two errors to cancel out resulting in an unusually accurate result.

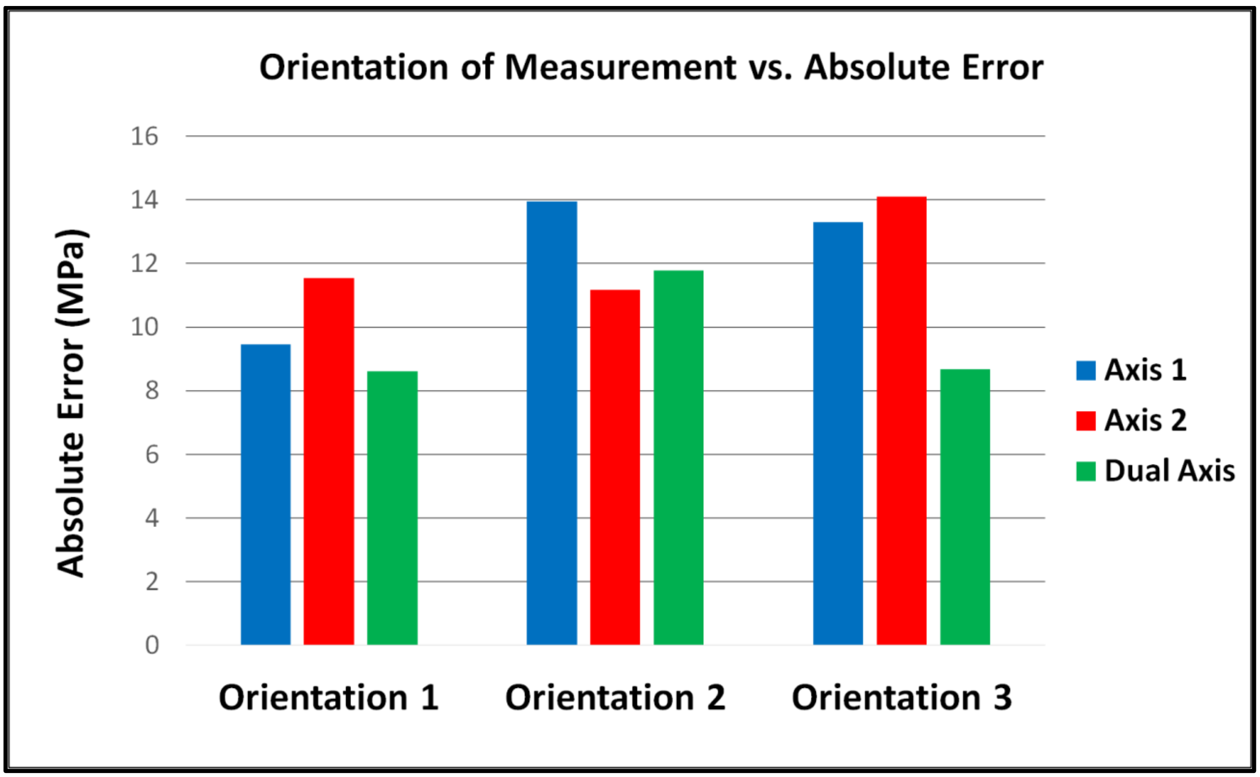

Graph 5.6 - Absolute error of each axis at Orientation 1, 2 and 3

When both measurement axes have equal sensitivity to a given stress state the dual axis computation does not have any means of improving the accuracy of the measurement. However, as explained in Section 2.3.2 the increased size of the data has been shown to improve the precision of the measurement [28].

5.3 Measurement Precision

Experiment 2 was conducted to determine the overall precision of the compact ESPI device. The measurement axes were oriented at 45° to the maximum principal stress as outlined in Orientation 3 of Figure 5.3c. A set of seven holes was made with a Ø 3/32” milling bit in a 2.4mm thick specimen. The standard deviation of the seven hole set was then evaluated.

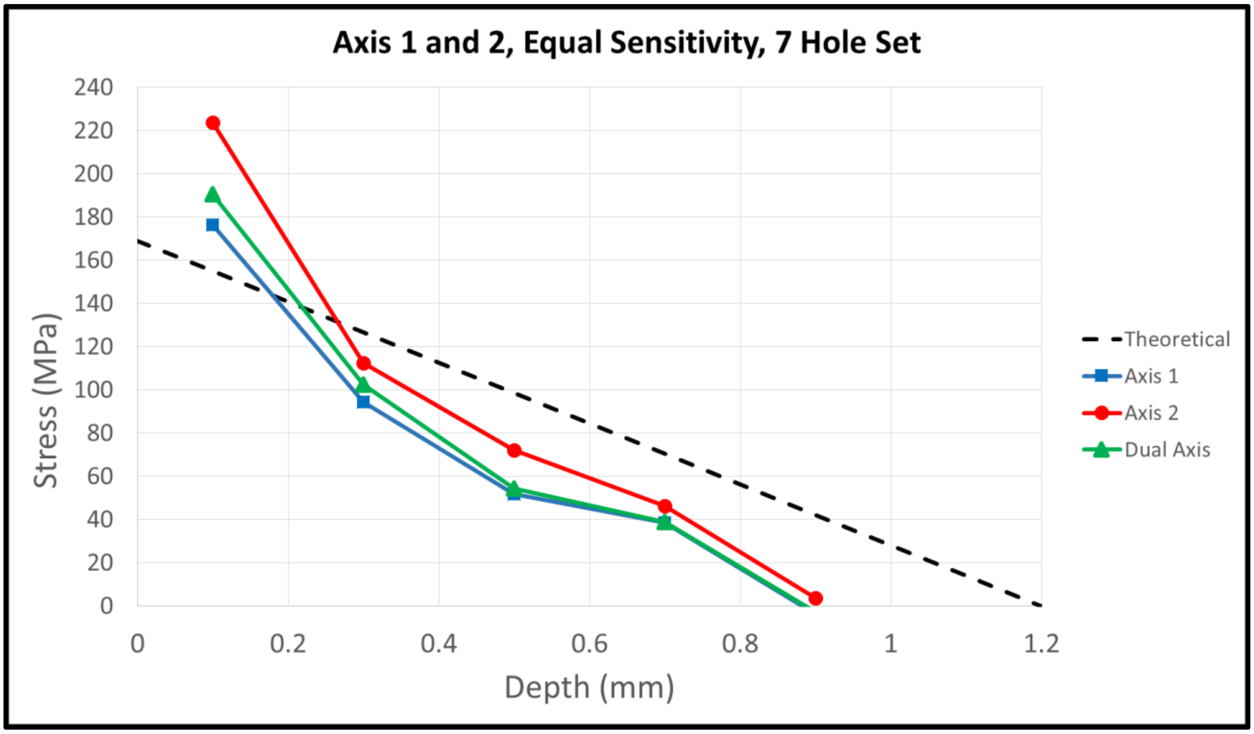

Graph 5.7 – Averaged measurement stress profiles, 7 hole set at 45° to principal

Graph 5.7 shows the averaged stress profile from each axis. As in the previous experiment all measurements followed the expected linearly decreasing trend.

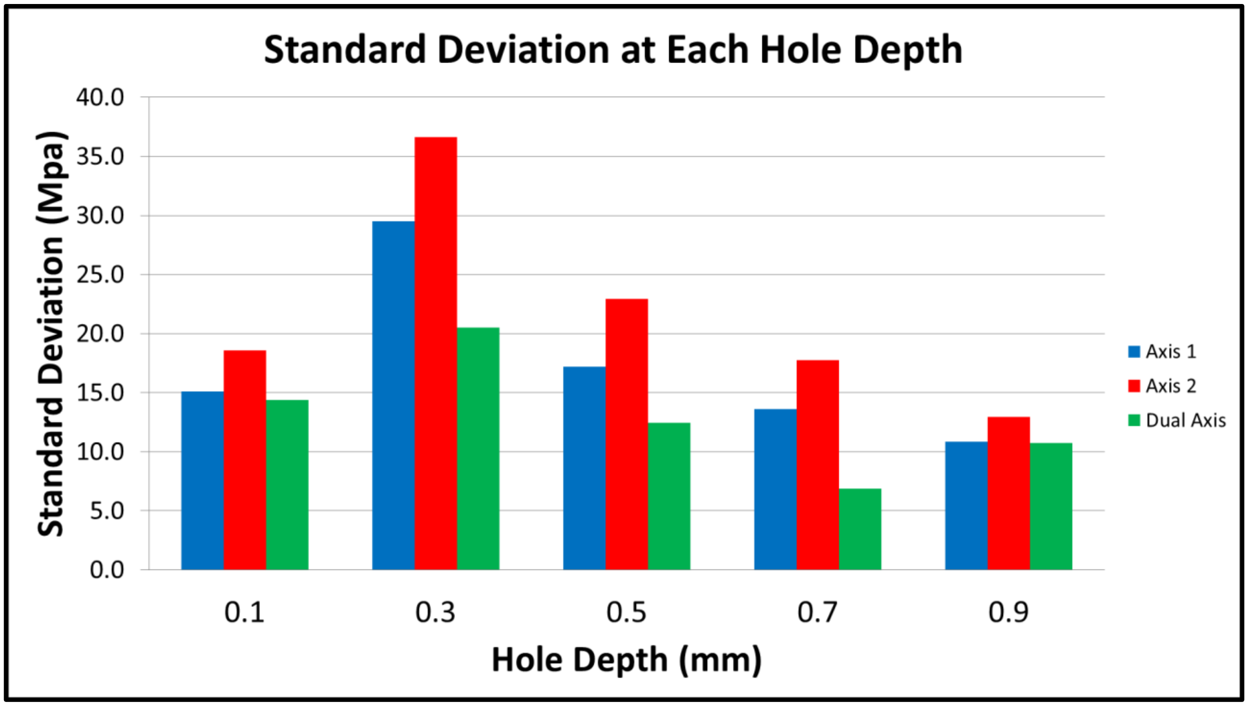

Graph 5.8 – Standard deviation at each hole depth, seven hole set at Orientation 3

Graph 5.8 compares the standard deviation at each hole depth. The deviations are evenly distributed with the exception of hole depth 0.3mm. The variability between measurements is governed by the quality of the image as described in Section 2.3.3. Upon further investigation it was discovered that hole depth 0.3mm for the third hole had a noisy measurement resulting in an outlying stress evaluation. Table 5.1 compares the quality evaluation map of hole depth 0.3mm from hole 1 and hole 3 respectively. The green, blue and red pixels have low measurement quality and are therefore excluded from the residual stress computation. Only the white pixels are used. It is evident that hole 3 has a significantly noisier measurement resulting in an erroneous stress computation.

	Hole 1	Hole 3
Depth 0.3mm	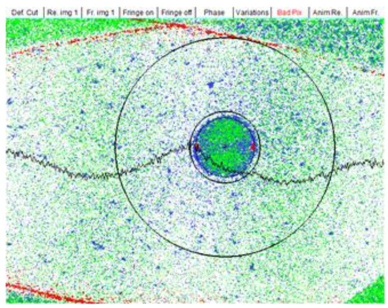	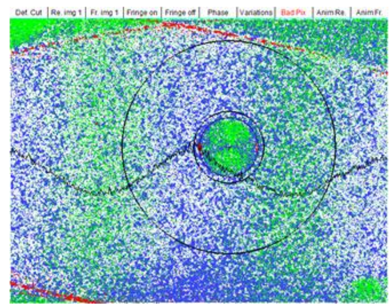

Table 5.1 - Measurement quality comparison

Graph 5.9 shows the resulting standard deviation if the outlying measurement from hole 3 is excluded.

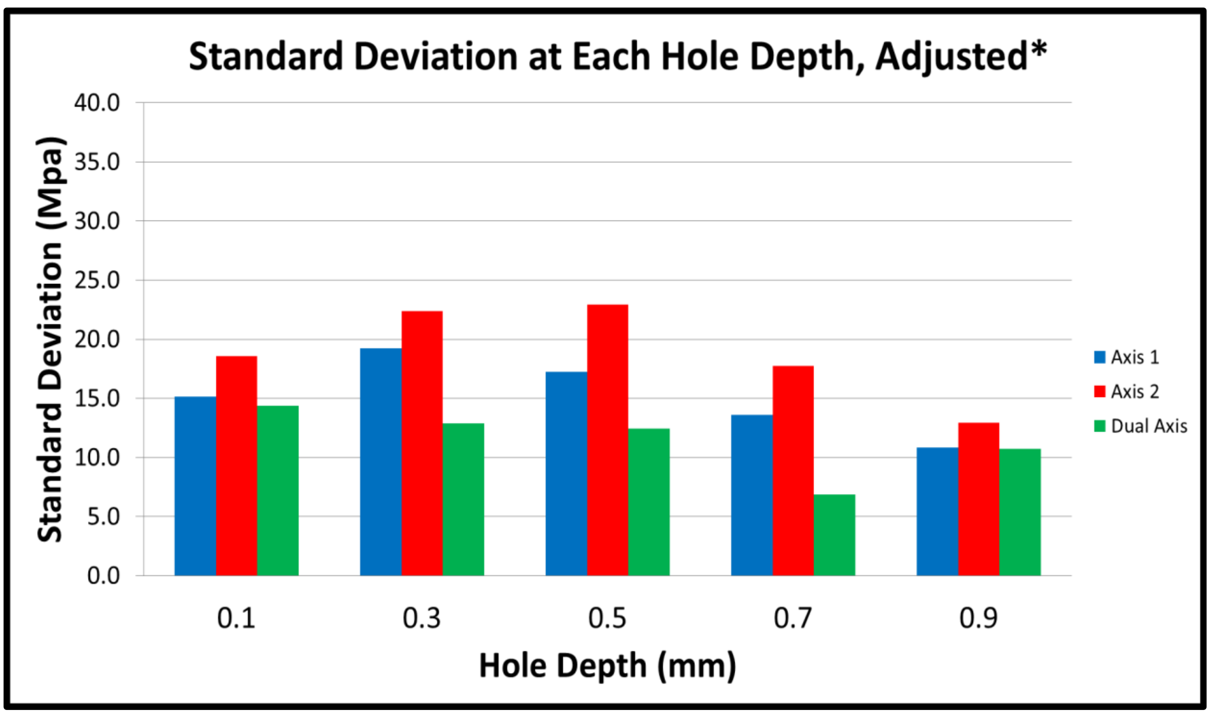

Graph 5.9 – Adjusted standard deviation, excluding outlying measurement from hole 3, depth 0.3mm

Graph 5.10 compares the overall standard deviation of each axis. Axis 1 has better overall precision than Axis 2. This is because for this measurement set the signal from Axis 2 experienced higher pixel saturation than Axis 1. The precision of dual axis interferometry is better than both individual axes. This is because the dual axis measurement uses twice the amount of data, as described in Section 2.3.2. If data are noisy in one of the measurement axis they are ameliorated by the measurement from the other axis.

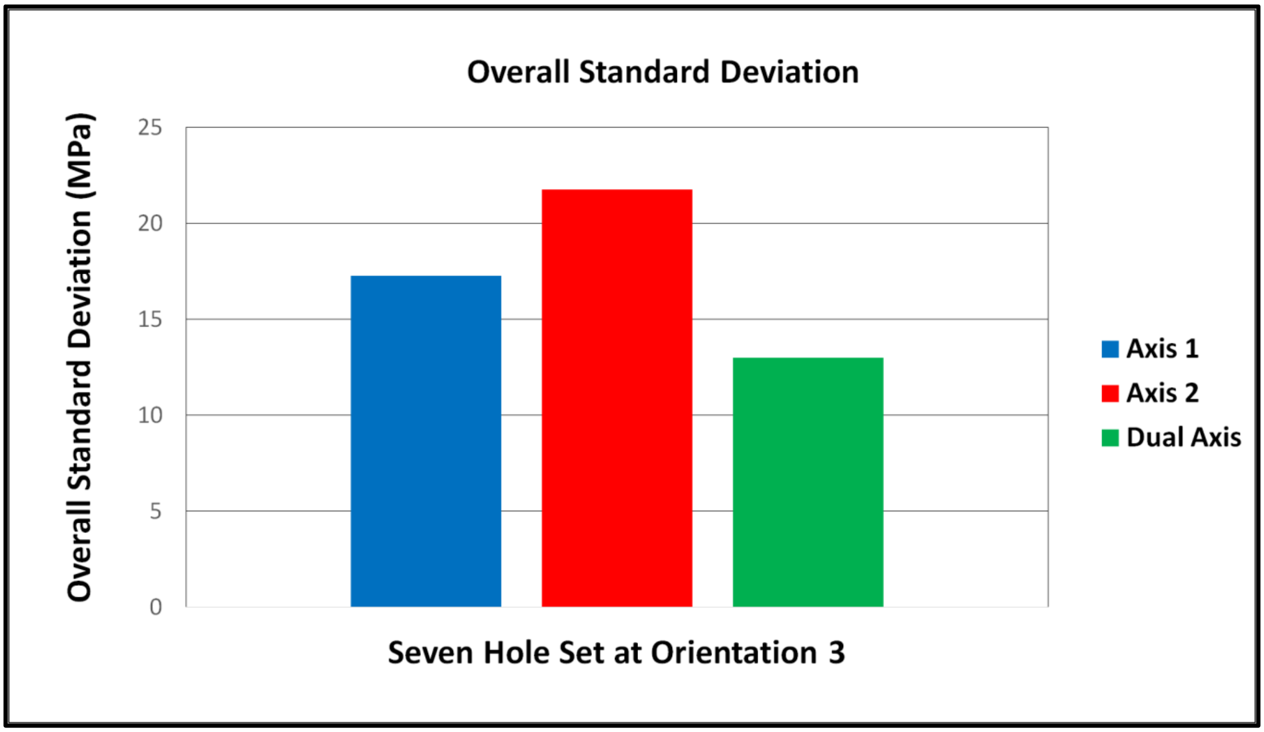

Graph 5.10 - Overall Standard Deviation of Each Axis

5.4 Sources of Error

The sources of error can be categorized into two types, global and axis specific. Global errors affect both measurement axes, whereas axis specific errors affect each axis individually. The aim of this thesis has been primarily to reduce the effects of axis specific sources of error.

5.4.1 Global Sources of Error

5.4.1.1 Elastic Modulus

The absolute error calculated in this analysis compares the measured stress to the theoretical stress computed using equation 27. Practically, the actual stress deviates from the theoretical stress due to the beam bending assumptions the equation from which it is derived. This deviation from the actual stress of the bend specimen is primarily due to the user specified elastic modulus. Realistically, the exact elastic modulus of the specimens is unknown and difficult to determine with precision. The rough value of the elastic modulus used affects both the theoretical bend stress, computed using equation 27, and the residual stress measurement, computed using equation 5. The effect of this error is evident in the stress profile difference between the preliminary and secondary experimentation. The 2.4mm specimen used for the preliminary experiment was cut from a different plate than the 2.4mm specimen used for the secondary experiment. As a result, the elastic modulus of the first specimen matched the 7.1GPa used in the computation whereas the second specimen did not, resulting in higher absolute errors.

5.4.1.2 Depth of Cut

The depth of cut governs the amount of residual stress relieved and the amount of displacement experienced on the surface. A hole that is too deep yields higher stresses than theoretically expected and vice versa.

5.4.1.3 Camera Adjustment

The camera adjustment is vital in detecting a clean signal from the measurement surface. Pixels that are too dark or too bright cannot be used in the measurement. Therefore, the shutter speed and f-number must be adjusted to provide well balanced image contrast. Since the two illumination sources were viewed with the same camera, Axis 2 resulted in several oversaturated pixels. This is why Axis 2 had lower overall precision.

5.4.1.4 Coefficients

The surface displacements detectable by ESPI become steadily smaller with each hole depth. The coefficients described in equation 1 in Section 2.1.1 account for this effect. However, since these coefficients are interpolated over a range of specimen thicknesses and hole geometries their accuracy is compromised and as a result the measured residual stresses are affected.

5.4.2 Axis Specific Sources of Error

5.4.2.1 Measurement Orientation

The orientation of the measurement axis is a significant source of error. As outlined in Section 5.2 the closer an axis is to the principal stress direction the more accurate the measurement is. This directional bias of single axis ESPI measurements is a major motivation for this work.

5.4.2.2 Coherence Length

As described in Section 2.3.3 the coherence length of the illumination source governs the quality of the signal and hence the accuracy of the measurement. The coherence length of the laser diodes use in the compact ESPI device is 1.5mm. As described in Section 4.1, the optical arrangement was geometrically tuned such that the rays of light interfere within the 1.5mm coherence length. The major source of coherence length deviations is caused by temperature fluctuations. As described in Section 3.4.1.1, temperature fluctuation in the laser can cause it to operate in a state called 'mode hopping’ which significantly reduce the coherence length. A thermoelectric cooler is used to control the temperature of the laser, however, at extended periods of operation the temperature of the laser was observed to increase and the quality of the measurements deteriorate. The laser then had to be turned off and allowed to cool to normal operating temperatures. These fluctuations in laser temperature where a major source of noise for each of the measurement axes.

5.5 Conclusion

This chapter highlights the accuracy and precision capabilities of the compact ESPI device. The Experiment 1 shows how accuracy depends on the orientation of measurement and principal stress direction. The overall absolute error of the device when measuring along the principal stress direction is 10MPa, and 14MPa when measuring perpendicular to it. The dual axis computation always follows the more accurate axes. Therefore, when measuring a biaxial stress state the dual axes computation yields more accurate results than either of the individual measurement axes. This characteristic of the dual axis computation allows for accurate measurements to be taken without prior knowledge of the principal stress direction. Experiment 2 shows how the dual axes computation improves the precision of the measurement. The standard deviation of each axes individually is 20 MPa and 13 MPa for the dual axes computation. The dual axes computation doubles the amount of data at each location on the displacement map thereby improving the statistical averaging of the least square computation.

Two types of error where observed during experimentation, global and axis specific. Global sources of error play an important role but are generally outside the control of the compact ESPI device. This work focuses on improving the axis specific sources of error by removing the inherent directional bias of single axis measurements and geometrically tuning the illumination source.

Chapter 6: Conclusion

The purpose of this work is to develop a compact and robust ESPI instrument capable of providing high quality and isotropic residual stress measurements. The motivation for such a device is to measure the residual stress state of large or immovable structures in the field. The major limiting factor for compact interferometry is the requirement of a highly coherent illumination source. Furthermore, the accuracy of ESPI measurements depends on the orientation of the device relative the maximum principal stress direction. In the field the principal stress direction is often unknown therefore aligning an instrument with it is impractical. **This work addresses these issues by developing a compact, geometrically tuned, dual axis ESPI device capable of providing complete in-plane residual stress sensitivity with accuracy ranging 9-12MPa and precision of 13MPa.**

6.1 Contribution

This work presents three major contributions to the field of residual stress measurements using hole drilling and ESPI:

1. The coherence length of the ESPI illumination source governs the ability of the interferometer to produce a detectable signal as represented in a unit-less ratio called visibility. This work introduces a novel diffraction grating arrangement that can be tuned geometrically to provide extremely high visibility measurements using low coherence laser diodes. Section 3.4.2 showed that a visibility of 0.3, comparable to the visibility of highly coherent illumination sources, can be achieved with a laser diode of 1.5mm coherence length. Furthermore, by establishing a relationship between the geometry of the interferometer and the visibility of the measurement a practical means

of measuring the coherence length of the illumination source was developed. This technique can be used to characterize the illumination sources of future systems.

2. Single axis residual stress measurements rely on the small effect of Poisson's ratio to calculate the stress 90° to the axis of measurement. Consequently, the measurement accuracy depends on the orientation of measurement relative to the maximum principal stress in the structure. In the field it is impractical to require the measurement device to align with the maximum principal stress it is attempting to detect. This work addresses this problem by combining two orthogonal axes of measurement. This arrangement guarantees an alignment with the maximum principal stress within 45°, yielding a dual axis accuracy of 9-12MPa respectively. Furthermore, a second axis of measurement doubles the quantity of data in the displacement map, improving the reliability of the least squares computation and the overall precision of the measurement. Each of the measurement axes of the dual axis ESPI device has a precision of 20MPa individually and a combined computational precision of 13MPa.

3. The ESPI device constructed for this research integrates the compactness and adjustability of diffraction grating interferometry with the improved sensitivity and precision of a dual axis arrangement. This integration of ESPI and hole drilling modules into a compact stand-alone unit is a significant milestone for in-field residual stress measurements.

6.2 Remaining Challenges

There are three main issues which affected the present results:

1. Deviations between the user specified depth of cut and actual depth of cut have a direct bearing on measurement accuracy. The drilling mechanism was analyzed to have a deviation of 0.05mm across a 1.00mm depth cut. The current overhanging arrangement of the drilling mechanism allows for some deflection. A means of stiffening the system would have to be devised. Additionally, an improved stepping algorithm for the driving stepper motor could improve the hole drilling precision

2. If the ambient temperature is over 25°C the thermoelectric cooler has difficulty cooling the laser diode after about an hour of operation. The increased temperature of the laser diode results in a mode-hopping state of the laser. To resolve this issue a larger heat sink, capable of dissipating more heat at a faster rate, will need to be installed.

3. Two illumination sources were viewed with the same camera adjustment. This made it difficult to view both illumination sources with optimal brightness and contrast. This issue can be addressed by programming independent exposure times for each measurement axes in the data acquisition software.

6.3 Future Work and Recommendations

Once the remaining challenges have been addressed, the next step of this research is to begin taking measurements in the field. A practical application for this device is with a large >0.50m diameter pipe. The internal pressure of the pipe will create axial and hoop stresses that can be measured and compared to the theoretically expected results. Any discrepancy between the theoretical and expected results could mean residual stress in the pipeline. This in-field experimentation will highlight additional issues and avenues to be explored.

A further improvement to the device would be to replace one of the illumination sources with a green or blue laser and to instrument the device with a color camera. The dual axis measurement could then be taken simultaneously by illuminating the surface with both lasers and separating the signal using the color camera.

Bibliography

[1] G. S. Schajer, *Practical Residual Stress Measurement Methods*, 1st ed. Chichester, UK: John Wiley & Sons Ltd., 2013.

[2] P. J. Withers, "Residual Stress and its Role in Failure," *Reports on Progress in Physics*, vol. 70, no. 12. pp. 2211–2264, 2007.

[3] M. B. Prime, "Residual Stresses Measured in Quenched HSLA-100 Steel Plate," in *Experimental Mechanics*, 2005, vol. 52, no. 1, pp. 1–7.

[4] J. B. Cohen, "Residual Stresses in Materials," *American Scientist*, vol. 79, no. 2. pp. 142–153, 2014.

[5] "Cardinal Glass Industries," 2013. [Online]. Available: http://www.cardinalst.com/products/solartemp/. [Accessed: 13-Oct-2014].

[6] J. Mathar, "Determination of Initial Stresses by Measuring the Deformations Around Drilled Holes," *ASTM*. 1934.

[7] G. S. Schajer, "Hole-Drilling Residual Stress Measurements at 75: Origins, Advances, Opportunities," *Experimental Mechanics*, vol. 50, no. 2. pp. 245–253, 2009.

[8] N. J. Rendler and I. Vigness, "Hole-drilling Strain-gage Method of Measuring Residual Stresses," *Experimental Mechanics*, vol. 6, no. 12. pp. 577–586, 1966.

[9] "E837 - 13 Standard Test Method for Determining Residual Stresses by the Hole-Drilling Strain-Gage Method," *ASTM*. West Conshohocken, USA, pp. 1–16, 2014.

[10] P. Jacquot, "Speckle Interferometry: A Review of the Principal Methods in Use for Experimental Mechanics Applications," *Strain*, vol. 44, no. 1. pp. 57–69, 2008.

[11] J. F. Vandenrijt and M. Georges, "Electronic Speckle Pattern Interferometry and Digital Holographic Interferometry With Microbolometer Arrays At 10.6 μm," *Applied Optics*, vol. 49, no. 27. pp. 5067–75, 2010.

[12] "Measurement of Residual Stresses by the Hole-Drilling Strain Gage Method. Tech Note TN-503," *Vishay Precision Group*. pp. 19–33, 2010.

[13] M. R. Viotti and A. G. Albertazzi, "Compact Sensor Combining Digital Speckle Pattern Interferometry and The Hole-Drilling Technique to Measure Nonuniform Residual Stress Fields," *Optical Engineering*, vol. 52, no. 10. pp. 1–8, 2013.

[14] M. R. Viotti and A. G. Albertazzi, "Industrial Inspections by Speckle Interferometry: General Requirements and a Case Study," in *SPIE*, 2009, vol. 7389, pp. 1–15.

[15] M. R. Viotti and A. G. Albertazzi, “Image Quality Improvement of an Achromatic DSPI Interferometer,” in *SPIE*, 2012, vol. 8493, pp. 1–8.

[16] E. Ponslet and M. Steinzig, “Residual Stress Measurements Using The Hole Drilling Method and Laser Speckle Interferometry Part I,” *Experimental Techniques*, vol. 27, no. 3. pp. 43–46, 2003.

[17] E. Ponslet and M. Steinzig, “Residual Stress Measurements Using The Hole Drilling Method and Laser Speckle Interferometry Part II: Analysis Technique,” *Experimental Techniques*, vol. 27, no. 4. pp. 17–21, 2003.

[18] G. S. Schajer, “Full-field Calculation of Hole Drilling Residual Stresses from Electronic Speckle Pattern Interferometry Data,” *Experimental Mechanics*, vol. 45, no. 6. pp. 526–532, 2005.

[19] G. S. Schajer, B. Winiarski, and P. J. Withers, “Hole-Drilling Residual Stress Measurement with Artifact Correction Using Full-Field DIC,” *Experimental Mechanics*, vol. 53, no. 2. pp. 255–265, 2012.

[20] S. Wolfgang and L. Yang, *Digital Shearography: Theory and Application of Digital Speckle Pattern Shearing Interferometry*. Society of Photo Optical, 2003.

[21] G. Cloud, “Optical Methods in Experimental Mechanics Part 4: Some Basic Methods of Interferometry,” *Experimental Techniques*, vol. 26, no. 6. pp. 21–24, 2002.

[22] G. Cloud, “Optical Methods in Experimental Mechanics Part 2 : Interference of Light Waves,” *Experimental Techniques*, vol. 26, no. 4. pp. 13–15, 2002.

[23] B. E. Saleh and M. C. Teich, *Fundamentals of Photonics*, 2nd ed. New Jersey, USA: John Wiley & Sons Ltd., 2007.

[24] G. Cloud, “Optical Methods in Experimental Mechanics Part 24: Demonstration of Laser Speckle Phenomena,” *Experimental Techniques*, vol. 30, no. 6. pp. 27–30, 2006.

[25] G. Cloud, “Optical Methods in Experimental Mechanics Part 26 : Subjective Speckle,” *Experimental Techniques*, vol. 31, no. 2. pp. 17–19, 2007.

[26] G. Cloud, “Optical Methods in Experimental Mechanics Part 27: Speckle Size Estimates,” *Experimental Techniques*, vol. 31, no. 3. pp. 19–22, 2007.

[27] Y. An, “Residual Stress Measurements Using Cross-Slitting and ESPI,” *University of British Columbia*. MASc Thesis, Vancouver, p. 73, 2008.

[28] G. S. Schajer, “Dual-Axis Hole-Drilling ESPI Residual Stress Measurements,” *Journal of Engineering Materials and Technology*, vol. 132, no. 1. pp. 633–642, 2009.

[29] M. Steinzig and T. Takahashi, “Residual Stress Measurements Using The Hole Drilling Method and Laser Speckle Interferometry Part IV: Measurement Accuracy,” *Experimental Techniques*, vol. 27, no. 4. pp. 59–63, 2003.

[30] M. Pospiech and S. Liu, “Laser Diodes: An Introduction,” *University of Hannover*, 2004. [Online]. Available: http://www.matthiaspospiech.de/files/studium/praktikum/diodelasers.pdf. [Accessed: 01-Sep-2013].

[31] T. A. Heumier and J. L. Carlsten, “Mode Hopping in Semiconductor Lasers, Application Note 8,” *ILX Lightwave*, 2003. [Online]. Available: http://assets.newport.com/webDocuments-EN/images/AN08_Mode_Hopping_Laser_Diode_IX.PDF. [Accessed: 01-Sep-2013].

[32] Attwood, “Spatial and Temporal Coherence: Coherent Undulator,” *University of Berkeley, California*, 2007. [Online]. Available: https://www.youtube.com/watch?v=YTkNSa-Ay5g. [Accessed: 01-Sep-2013].

[33] S. Ezekiel, “Optics: Two-beam Interference,” *MIT Open Courseware*, 2012. [Online]. Available: https://www.youtube.com/watch?v=zD6tTb74KdU. [Accessed: 01-Sep-2013].

[34] “Visible Transmission Grating,” *Thor Labs*, 2014. [Online]. Available: https://www.thorlabs.com/newgrouppage9.cfm?objectgroup_id=1123. [Accessed: 01-May-2013].

[35] J. Zhang and T. C. Chong, “Fiber Electronic Speckle Pattern Interferometry and Its Applications in Residual Stress Measurements,” *Applied Optics*, vol. 37, no. 28. pp. 6707 – 6715, 1998.

[36] J. Gere, *Mechanics of Materials*, 6th ed. Toronto, ON: Thomson Cananda Limited, 2006.

[37] ASTM, “Standard Specification for Aluminum and Aluminum-Alloy Sheet and Plate,” *B209-14, American Society for Testing and Materials*. West Conshohocken, PA, pp. 1–29, 2007.